ULTRA-MASSIVE MIMO COMMUNICATIONS IN THE MILLIMETER WAVE AND TERAHERTZ BANDS FOR TERRESTRIAL AND SPACE WIRELESS SYSTEMS

A Dissertation
Presented to
The Academic Faculty

By

Shuai Nie

In Partial Fulfillment
of the Requirements for the Degree
Doctor of Philosophy in the
School of Electrical and Computer Engineering
College of Engineering

Georgia Institute of Technology

May 2021

ULTRA-MASSIVE MIMO COMMUNICATIONS IN THE MILLIMETER WAVE AND TERAHERTZ BANDS FOR TERRESTRIAL AND SPACE WIRELESS SYSTEMS

Thesis committee:

Dr. Ian F. Akyildiz, Advisor
School of Electrical and Computer Engineering
Georgia Institute of Technology (formerly)

Dr. Gordon Stüber
School of Electrical and Computer Engineering
Georgia Institute of Technology

Dr. Raghupathy Sivakumar, Chair
School of Electrical and Computer Engineering
Georgia Institute of Technology

Dr. Chuanyi Ji
School of Electrical and Computer Engineering
Georgia Institute of Technology

Dr. Manos M. Tentzeris
School of Electrical and Computer Engineering
Georgia Institute of Technology

Dr. Ashutosh Dhekne
School of Computer Science
Georgia Institute of Technology

Date approved: April 20, 2021

ACKNOWLEDGMENTS

First and foremost, I would like to express my heartiest gratitude to my advisor, Prof. Ian F. Akyildiz, for his continuous support, guidance, and encouragement to me during my Ph.D. journey. I have been blessed to have the opportunity to research under his supervision and learn under his mentorship. He has led me to numerous amazing research opportunities and allowed me to explore new directions of my research interests. I am also grateful to him for his enthusiasm and passion, which not only motivated me to advance towards the completion of this dissertation, but inspired me to embrace the unknowns in my future career. I am also sincerely thankful for the precious life lessons shared by Prof. Akyildiz that will perpetually influence and guide me throughout my career and life.

I would also like to express my deep appreciation to my committee members, Prof. Raghupathy Sivakumar, Prof. Gordon Stüber, Prof. Manos Tentzeris, Prof. Chuanyi Ji, and Prof. Ashutosh Dhekne, who provided me valuable and constructive suggestions on my work. Their invaluable feedback have helped me better shape this work towards the completion of my doctoral research.

My sincere thanks go to members of the Broadband Wireless Networking (BWN) Lab who helped and encouraged me over the past years. I remember all the laughters and wonderful trips we shared together. I am also thankful for my friends in and out of Georgia Tech, for their constant support and patience to me, especially during the final year in this journey. Thank you for being in my life.

Finally, to my parents and family, thank you for your endless love. I could never be able to become who I am without your understanding, support, and encouragement. This dissertation is dedicated to you.

TABLE OF CONTENTS

LIST OF TABLES

LIST OF FIGURES

SUMMARY

Wireless communication systems have experienced substantial progress over the past few years. In parallel to the massive growth in the total number of wirelessly connected devices, there has been an increasing demand for higher speed wireless communication. Following this trend, wireless multi-hundred gigabit-per-second (Gbps) and terabit-per-second (Tbps) links are expected to become a reality in the next several years. In this context, millimeter wave (mmWave, 30–300 GHz) and terahertz (THz)-band (300 GHz–10 THz) communications are envisioned as key wireless technologies in the fifth generation (5G) and beyond eras. The very large available bandwidth at mmWave (with up to 10 GHz of consecutive bandwidth) and THz-band (with several hundreds of GHz) frequencies will alleviate the spectrum scarcity problem and capacity limitations in current wireless networks. Nevertheless, a major challenge at these frequencies is the limited communication distance, which results from the very high channel path loss and the limited transmission power of mmWave and THz transceivers.

The objective of this thesis is to address the important problem inherent in these frequency bands for their applications in both terrestrial and space wireless systems. First, for the terrestrial wireless system, especially in the indoor communication scenario, a theoretical design of the *Intelligent Communication Environments* based on the ultra-massive multiple-input multiple-output (UM MIMO) platform is proposed. The aims of this design are to increase the communication distance and extend coverage for users not directly visible to access points at mmWave and THz-band frequencies. The UM MIMO system, which is enabled by a type of two-dimensional artificial material of metasurfaces in mmWave or plasmonic antenna arrays at THz band, allows precise control and engineering of electromagnetic waves with sub-wavelength resolution. Second, with the utilization of large antenna arrays as reconfigurable reflectarrays in the Intelligent Communication Environments, in order to provide received signal strength improvement at end users, beamform-

ing solutions for metasurface-based reflectarray are proposed. Dynamic radiation pattern design based on phase-gradient metasurfaces is presented. A further extension on polarization diversity is analyzed with a dual-polarization channel enabled by metasurfaces' polarization-tuning functionality. Third, an extended Kalman filtering approach is proposed and analyzed for the dominant path tracking at THz band, which provides an effective path-tracking solution in a non-stationary channel in a typical indoor office environment. Fourth, for future inter-satellite communications, the channel peculiarities in both the Earth's upper atmosphere and deep space on inter-satellite links (ISLs) operated in the mmWave and THz bands are characterized. In particular, effects of the charged particles on channel impairments and their impact on beam angle misalignment are analyzed. Last but not the least, owing to the benefit of the abundant spectrum resources at mmWave and THz bands, a multi-band communication for small satellites to meet the throughput requirements for inter-satellite data-intensive applications is proposed. This architecture can significantly leverage the capabilities of current small satellite networks, and will pave the way for the development of future satellite networks in the 6G and beyond era.

CHAPTER 1
INTRODUCTION

During the past decade, there has been a drastic increase in wireless data traffic along with an ever-growing demand for a faster and more reliable wireless network. The development and deployment of the fifth-generation (5G) wireless communication systems have demonstrated a significant improvement on the maximum achievable throughput of 8.5 gigabits-per-second (Gbps) in a lab environment over the predecessor of the fourth-generation networks. In addition to a remarkable improvement over maximum throughput, the system latency in the 5G is expected to fall below ten milliseconds. Accompanying the system performance upgrades is a surge in wireless connectivity market, where the number of wireless devices, across verticals spanning from consumer electronics to healthcare, has reached 14 billion in 2020[1].

In parallel to the massive growth in the total number of wirelessly connected devices, there has been an increasing demand for more innovative wireless communication techniques to achieve higher speeds. Following this trend, wireless multi-hundred Gbps and Terabit-per-second (Tbps) links are expected to become a reality within the next five years. Therefore, it is necessary to call upon a set of transformative solutions that have sufficient room to both accommodate the growing number of devices and support network requirements with respective to throughput, latency, coverage, and reliability.

As the research focus has been gradually steered towards the development of the sixth-generation (6G) wireless communication networks, several emerging enabling technologies have been discussed, and the terahertz (TH) band communication serves in a frontline [1]. Spanning in the frequency range of 300 GHz to 10 THz, this spectrum offers abundant frequency resource feasible for wireless communications. Joining forces with the currently

[1] https://www.statista.com/statistics/245501/multiple-mobile-device-ownership-worldwide/

millimeter (mm)-wave (30–300 GHz) for the 5G networks, this previously underexplored spectrum is envisioned as a key enabling solution in the 6G and beyond era. The very large available bandwidth will alleviate the spectrum scarcity problem and capacity limitations in current wireless networks. If properly utilized, such massive spectral resources can lead to drastic improvements in terms of both individual and multi-user throughput.

Nevertheless, a major challenge at mmWave and THz-band frequencies is the limited communication distance, which results from the very high path loss and the limited transmission power of mmWave and THz transceivers. To overcome this problem, high-gain directional antenna systems are needed. Besides, antenna arrays are utilized to implement massive multiple-input-multiple-output (MIMO) and ultra-massive MIMO communication systems. Such multiple-antenna solutions have been proven to achieve substantial beamforming gain to compensate for the high path loss at these frequency bands [2].

Recently, the Federal Communications Commission (FCC) has released the frequency bands above 95 GHz till 3 THz for research purposes[2]. While a handful of cellular operators have adopted low millimeter wave frequencies for their 5G services with the intention of achieving a maximum data rate of 100 Gbps, the test results thus far leave much to be improved, showing a peak data rate of around 8.5 Gbps in a lab environment[3]. This gap between the targeted and practically achievable data rates is influenced by multiple factors, including a high complexity in realistic communication channels, imperfections in circuitry design, and interference from other systems operating in adjacent frequency bands, among others. Nevertheless, even though the THz band has been applied in imaging and object detection, as well as for THz radiation spectroscopy in astronomical research, their use cases in wireless communications are still under preliminary studies. Lying between the mmWave spectrum and infrared light spectrum, such THz band has been previously deemed as a "no-man's land". However, owing to their abundant spectrum resources and

[2]https://docs.fcc.gov/public/attachments/DOC-356588A1.pdf

[3]https://news.samsung.com/us/samsung-5g-mmwave-speeds-8-5gbps-multiple-devices-demonstrates-full-potential/

great potentials for providing ultra-high-throughput connectivity, major progress in the domains of transceiver and antenna design has seen THz links as a promising option for realizing indoor communications networks. More recently, there has been significant progress on realizing wireless network on chip (WNoC) using THz bands [3].

1.1 Overview of THz band wireless communications

In this section, a brief overview is dedicated to the background of research on THz band wireless communications, which mainly focuses on recent progress in device design, physical-layer solutions, and use cases of the this spectrum.

1.1.1 Devices in the THz band

The need for higher output power, lower phase noise, and better receiving sensitivity in THz band transceivers has driven advances in device development. Currently, three main directions are deployed in THz band signal generation, which are *photonics-based*, *electronic-based*, and *emerging material-based* approaches, respectively.

In the photonics-based approach, many III-V semiconductors, including gallium arsenide (GaAs) and indium phosphide (InP), which provide high electron mobility, are excellent candidates especially for high frequency (i.e., above 100 GHz) applications. Such photonics-based techniques generate time-domain pulses with lengths of femto-seconds (10^{-15} s) and experimental results have demonstrated 50 Gbps data links in an indoor scenario at 300 GHz using the uni-traveling-carrier photodiode (UTC-PD) technique [4]. The UTC-PDs and modified UTC-PD structures, as an effective photomixing solution which allows wider spectrum-tuning and simpler construction compared to laser pulse generators, have pushed the output signal range from 300 GHz to 2.5 THz, with output powers of 10 μW at 300 GHz and 1 μW at 1 THz [5]. Additionally, a design based on slot-antenna-integrated UTC-PDs has shown superior performance in resultant signal strengths at 350–850 GHz and 900 GHz–1.6 THz, compared to that of the bowtie-antenna integrated

UTC-PD [6]. Similar photonics-based THz signal generation at above $1\ \mathrm{THz}$ can be realized using quantum cascade lasers (QCLs) and other solid state lasers [7]. However, the operations of such devices are limited at room temperatures, requiring liquid helium cooling, which affects their deployment in local area networks with space restrictions. Furthermore, photoconductive antennas (PCAs) have been utilized widely for both pulse and continuous-wave signal generation at THz band [8], demonstrating a wide spectrum (up to $4.5\ \mathrm{THz}$) with a remarkable dynamic range of up to $100\ \mathrm{dB}$ [9].

In parallel to the photonics-based approach for THz band device design which down-converts the optical frequencies, the electronic-based THz band signal generation relies on frequency up-conversion using multipliers [10], including frequency doublers and triplers, as well as backward wave oscillators [11]. A recent experiment has demonstrated an all-electronics-based wireless link at $240\ \mathrm{GHz}$ with a throughput of $50\ \mathrm{Gbps}$ and a maximum 29% error vector magnitude using QPSK modulation [12]. The backward wave oscillator, which is a compact design to generate THz band signals based on the mechanism of energy transfer from an electron beam to an electromagnetic wave through a vacuum tube, has been used to generate signals at $300\ \mathrm{GHz}$ with an output power of $1\ \mathrm{W}$ in plasma diagnostics [11].

Among the two commonly used approaches, the photonics-based design benefits from a relatively simpler transceiver architecture based on the photomixing technique, while the electronics-based solution relies on cascaded frequency up-conversion of RF signals, which sets stringent requirements on linear-range operation and potentially limits the terahertz bandwidth. On the other hand, the electronics-based approach is less sensitive to environmental conditions, such as temperature, humidity, among others, which makes it more favorable for outdoor operations, whereas the link reliability from its photonics-based counterpart is affected by scattered particles in the channel, making the THz band link less robust.

Besides these classical approaches for THz band device development, new materials,

including graphene, carbon nanotubes, graphene nanoribbons, and metamaterials, are gaining more attention due to their extremely high electron mobility in the order of $8,000$–$10,000\ \mathrm{cm}^2/(\mathrm{V}\cdot\mathrm{s})$ at room temperature, as compared to $1,400\ \mathrm{cm}^2/(\mathrm{V}\cdot\mathrm{s})$ of silicon, and $8,500\ \mathrm{cm}^2/(\mathrm{V}\cdot\mathrm{s})$ of GaAs, which means that the link throughput can be potentially up to ten times higher than that currently achievable with most semiconductors [13]. The graphene-based devices, offering outstanding mechanical, electrical, and optical properties, have been utilized in the development of power detectors at $600\ \mathrm{GHz}$ [14], as well as plasmonic antenna arrays and transceivers [15, 16]. Graphene-based devices have the potential to break new ground in reaching the desired level of performance at much higher frequencies above $1\ \mathrm{THz}$.

1.1.2 Physical layer modeling at the THz band

The realization of wireless communications at THz frequencies requires the development of accurate channel models to capture the impact of both channel peculiarities including the high atmospheric attenuation and molecular absorption rates at various transmission windows, as well as the propagation effects including reflection, scattering, and diffraction, with respect to different materials. Current research has reported several efforts to provide fundamental understanding of such channels. For example, an early work in [17] demonstrates the remarkable capacity the THz band channel can support for short transmission distances. The model provides a detailed analysis on the effect of attenuation caused by the molecular absorption and spreading loss, on which the performance of channel throughput is heavily dependent. Additionally, a stochastic channel model for indoor THz band communications at 300 GHz has been reported in [18] which characterizes both spatial and temporal domain channel information. More recently, based on the aforementioned applicable scenarios in the THz band, a stochastic channel model for kiosk applications has been reported in [19] which ranges from 200–340 GHz. The main takeaway from current models validated using either measurements or the ray-tracing technique is that the direct path

between the transmitter and the receiver and the single-bounce reflected paths dominate the received power, while other channel effects, including diffraction and scattering, attenuate power significantly along propagation.

1.1.3 Ultra-massive multiple-input multiple-output communications

As the aforementioned limitation in transmission distance at THz band, solutions ranging from the physical layer to the medium access layer as well as on a system level have demonstrated a successful case for THz frequency signals to propagate up to 100 m with the presence of obstructions [20]. In particular, the ultra-massive multiple-input multiple-output (UM MIMO) communications, enabled by an array size of 1024 plasmonic nano-antenna elements, can drastically boost the signal strength by steering and focusing the transmitted beams in both space and frequency [21]. Additionally, owing to the benefit of huge available spectrum at the THz band, the UM MIMO communication can also operate in a multi-band scenario, serving multiple users at different frequencies simultaneously.

By properly feeding the antenna array elements, different array modes can be adaptively generated, which range from jointly utilizing all the antennas to create a single razor-sharp beam to communicate with one distant user, to utilizing spatial diversity to communicate with multiple users. In particular, three adaptive modes are envisioned in the UM MIMO system:

- *Ultra-Massive Beamforming:* In this case, all the nano-antennas are fed with the same plasmonic signal, as in standard beamforming. This beamforming design can effectively overcome the very high attenuation at mmWave and THz-band frequencies and, importantly, enhance the communication distance. Moreover, owing to the sub-wavelength resolution, beam fronts can be designed to precisely and selectively target specific users while simultaneously minimizing the signal on non-target users, even in the presence of multi-path propagation, and also exploit the angle diversity.

- *Ultra-Massive Spatial Multiplexing:* By virtually grouping array elements [2], dy-

namically defined sub-arrays can be targeted to communicate with an individual user. This spatial multiplexing scheme uses multiple streams on a single carrier to increase the capacity per user, but is most effective when radio links operate in a high SNR regime and are bandwidth-limited. This mode improves the network throughput by the means of spatial multiplexing, given that the UM MIMO channel matrix is well-conditioned, or equivalently, provides the sufficient diversity and rank. The sub-wavelength integration of the plasmonic antennas provides an unprecedented level of granularity and enables the definition of interleaved arrays for different users.

- *Combination of UM Beamforming and UM Spatial Multiplexing:* The benefits of beamforming and spatial multiplexing can be achieved at the same time by adopting a combination of these two schemes, due to the very large bandwidth specially in the THz band and the very large antenna arrays with thousands of antenna elements. The array elements in one virtual subarray can be grouped for beamforming to increase SNR in power-limited situations. Alternatively, unique data streams can be injected for the different subarrays.

1.1.4 Medium access control in THz band

On top of physical layer channel models, the medium access control (MAC) schemes in THz band communications should adopt certain spatial and spectral features in order to provide solutions in resolving issues such as the deafness problem and LoS blockage [22, 23]. Different from commonly used MAC solutions in RF systems that utilize omnidirectional antennas, such as carrier sense multiple access with collision avoidance (CSMA/CA), the MAC protocols designed for THz band rely on handshakes between transceivers with highly directional beams. These razor-sharp beams can provide higher power radiation gain and prolong the transmission distance, but when misalignment happens, the deafness problem arises. As such, the deafness avoidance approach is required in MAC scheme design. Existing solutions utilized in IEEE 802.15.3c and others employ a beam-training

phase to estimate and steer beams towards destined devices. Recent works also propose methods based on angular division multiplexing [24] and *a priori* aided channel tracking schemes [25]. The results in such proposed solutions suggest that with good beam alignment strategies the channel throughput can be improved significantly.

Moreover, the MAC protocols can also resolve the issue of LoS blockage where the received power of a user device may undergo deep fading due to the device being held in a manner that blocks the LoS path. Studies have shown that such attenuation by the human body can be as high as $20\ \mathrm{dB}$ at $60\ \mathrm{GHz}$ and up [26, 27]. To mitigate the blockage problem, researchers have proposed a multi-hop scheme at the mmWave and THz bands to form alternative routes [28]. A careful link-level scheduling and neighbor discovery process is necessary to achieve high throughput while maintaining low interference.

1.1.5 Use cases of THz band communications

Different from wireless networks at lower frequencies, THz-band wireless communications has several unconventional application scenarios, owing to the distinct electromagnetic and photonics characteristics of this tremendously high frequency (THF) band. In addition to the promised Tbps-level links for cellular systems, THz-band spectrum can also be leveraged for the following scenarios:

- *Local Area Networks:* Several spectrum windows are feasible for short-range links within ten meters, including 625–$725\ \mathrm{GHz}$ and 780–$910\ \mathrm{GHz}$ [4]. The THz band communications are expected to form the THz–optics bridge to enable seamless transition between fiber-optics and THz-band links with zero latency.

- *Personal Area Networks:* THz band communications can provide "fiber-like" data rates without the need of wires, between multiple devices at a distance of a few meters. Such communication scenarios can be found in indoor offices and multimedia kiosks.

- *Data Center Networks:* Conventional data centers manage and maintain connectivity in wired networks using cables, resulting in high costs in terms of both installation and reconfiguration. On the other hand, THz links provide promising prospects for seamless connectivity at ultra-high-speeds in fixed networks and adaptability for hardware reconfiguration.

- *Wireless Network on Chip:* As the trend in transceiver hardware development motivates a higher level of integration and miniaturization as well as weight reduction, the THz band links can serve as a promising candidate to establish wireless connections among different modules within the transceiver chassis, in order to replace the wired connections commonly found in existing transceiver hardware products.

- *Nano-networks:* With its wavelength falling into the nanometer (10^{-9} m) range, the THz band can operate better than any other frequencies in nano-networks. Within this context, a nano-network is a set of interconnected nano-devices or nano-machines for information exchange, storage, and computation.

- *Inter-satellite Communications:* Lying largely outside the Earth's atmosphere, inter-satellite links are not constrained by atmospheric attenuation, which makes the THz band a favorable candidate for such communication links. Compared to existing spectrum resources allocated for inter-satellite links, the THz band has a much wider bandwidth which can accommodate more satellites and achieve higher link performance. Unlike the widely used optical links, the THz band has less stringent requirements on beam alignment, which can help maintain a high level of link stability as satellites drift from their orbits.

1.2 Overview of Intelligent Communication Environments

In current solutions, the primary focus is on the advancement of wireless transceiver hardware and software, as well as network optimization strategies. However, the wireless prop-

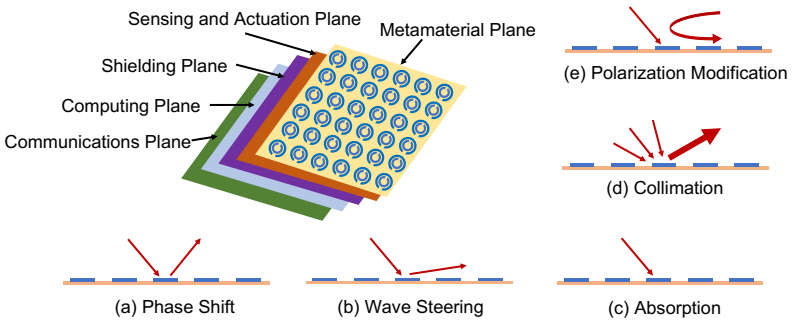

Figure 1.1: A layered metasurface-based reflectarray design for EM waves manipulation [29].

agation medium has been largely neglected. The wireless communication environments, for both indoor and outdoor scenarios, can be actively utilized in order to become controllable for signal propagation. To control signal propagation in environments is essentially to control how electromagnetic (EM) waves interact with scatterers, which include indoor furniture and outdoor buildings as well as other infrastructure. Typically, the controllable behaviors of EM waves include controlled reflection, absorption, wave collimation, signal waveguiding, and polarization tuning, as illustrated in Figure 1.1. The notion of "Intelligent Communication Environments"[4] resides in the control algorithms which are to be exploited to dynamically reconfigure the environments. In the following subsections, we elaborate on these controllable wave behaviors, current research efforts, as well as corresponding open issues.

1.2.1 Basics

The intelligent environments can be seen as a three-dimensional structure with several layers, each with different functionalities. Recent research under the European Commission Research Project "VisorSurf" has demonstrated a structure with five main layers, which are (from top to bottom) the EM behavior layer, the actuation and sensing layer, the shielding layer, the computing layer, and the communication layer, respectively [30]. Specifically, the

[4]Similar names are found in literature, including "reconfigurable intelligent surfaces (RISs)", "intelligent reflecting surfaces (IRSs)", "programmable wireless environments (PWEs)", and so on.

EM behavior layer is composed of metasurfaces, a two-dimensional representation of metamaterials, and has a tunable impedance to control directions of reflection of the EM waves. Some other works use reflectarray antennas as the top surface [31, 32]. The actuation and sensing layer consists of circuits for phase shifting and sensors for impinging signal sensing. Some options for actuation include PIN diodes with controllable biasing voltage as switches in reflectarray antennas, and complementary metal–oxide–semiconductors (CMOS) transistors as well as micro-electro-mechanical system (MEMS) switches for metasurfaces. The shielding layer isolates the upper and lower parts of the layered structure so as to minimize the possible interference. The computing layer serves to control the phase shifts and process sensed impinging waves. To this end, another reported solution makes use of field-programmable gated arrays (FPGAs) to fulfill such functions on metasurfaces [33]. Finally, the communication layer connects all upper layers and serves as the gateway towards the central controller which processes all connection requests, forwards and receives signals, and conducts the aforementioned controlled wave functions.

Compared to existing relays with multiple antennas which are widely deployed in wireless networks, Intelligent Communication Environments offer the following advantages: (i) a higher spatial diversity due to the wide coverage of the intelligent surface with controllable antenna arrays, (ii) a reduced processing time given that the computing and communication layers are directly underneath the surface layer, and (iii) a higher flexibility in network routing when impinging signals come from different directions and the intelligent surfaces are able to collimate waves and reflect them towards desired directions.

1.2.2 Functionalities

Bolstered by the layered structure, intelligent surfaces can enable controlled EM wave operations. At microwave and mmWave frequencies, metasurfaces are considered as a good candidate. In metasurfaces, a meta-atom is the smallest unit, which is a conductor with a size smaller than half the wavelength of the signal. Metasurfaces can thus control the im-

pinging EM waves with a very fine granularity. The meta-atoms are interconnected by a set of miniaturized controllers that connect the switches of the metasurfaces in the computing layer, while a gateway serves as the connectivity unit in the communication layer to provide inter-element and external control. At THz bands, when the metasurfaces do not yield optimal performance, the graphene-based plasmonic antenna arrays serve as a promising alternative.

Compared to metallic antenna arrays, the plasmonic antenna arrays can have much denser element layout and go beyond the conventional $\lambda/2$ sampling of space towards more precise space and frequency beamforming, owing to the physics of plasmonics. In a previous work, it has been demonstrated that graphene can be used to build nano-transceivers and nano-antennas with a maximum dimension of $\lambda/20$ at THz frequencies, thus allowing them to be densely integrated in very small footprints (1024 elements in less than 1 mm^2), as shown in Figure 1.1 [21]. Therefore, by incorporating the graphene-based plasmonic antenna arrays at THz bands and metasurfaces operating at mmWave bands, we can expand the operational spectrum of intelligent environments and utilize them in transmission and reception in a controllable manner.

1.2.3 Layered structure

Based on the operating principles of the aforementioned Intelligent Communication Environments, in this subsection, we anatomize the layered structure and detail each layer's functionality.

Metamaterial plane

The metamaterial plane is also the surface plane, as shown in Figure 1.1. In designs based on reflectarrays, phase shifts are applied to each element to improve useful signals while canceling interference [34, 31]. The metasurface element proposed in [35] with millimeter-scale dimensions is connected to a PIN diode with a bias voltage to control operation

modes, such as altering polarizations.

In general, this layer comprises the supported EM function of the tile as well as its operation principle. In particular, reflectarray employ modifiable phase shifts applied over their surface. In the far field of radiation, reflected rays can be considered co-directional, and their superposition—constructive or destructive—is controlled by the applied phase shifts. Hence, wave scattering or controlled reflecting functions can be attained. Metamaterial tiles, however, operate as surfaces with tunable local impedance [36]. Impinging waves create inductive surface currents over the tile, which can be routed by tuning the local impedance across the tile. Notice that the Huygens Principle dictates that any EM wavefront can be traced back to a current distribution over a surface [37]. As a result, in principle, metamaterials can produce any custom EM function as a response to an impinging wave. Common functions include wave steering, focusing, collimating (i.e., producing a planar wavefront as a response to an impinging wave), polarizing, phase altering, full or partial absorption, frequency selective filtering and even modulation [36, 33].

Sensing and actuation plane

In order to control the EM waves per actual channel conditions, the programmable surfaces are expected to sense the propagation environment and actuate the upper surface plane accordingly. Such layer contains hardware elements that can be controlled to achieve a phase shift or impedance distribution across a tile.

Commonly, the layer comprises arrays of planar antennas–such as copper patches–and multi-state switches between them. Reflectarray tiles usually employ PIN diodes with controllable biasing voltage as switches [35]. Metamaterials have employed a wider range of choices, both in the shape and geometry of the planar antennas and in the nature of switches. CMOS transistors, PIN diodes, MEMS switches, micro-fluidic switches, magnetic and thermal switches are but a few of the considered options in the literature [38]. Notably, some options—such as micro-fluid switches—are state-preserving in the sense

that they require power only to change state but not to maintain it, which is different from biased PIN diodes. Sensing impinging waves are also necessary for exerting efficient control over them. While this information can be provided by external systems [39], with dynamic channels and mobile end-users, tiles capable of incorporating sensing capabilities can be immune from the channel aging problem [40]. The sensing can be direct, employing specialized sensors, or indirect, e.g., via deducing some impinging wave attributes from currents or voltages between tile elements.

Computing plane

The computing functionality serves the processing functionality in the controllable surface system. In the metasurface designs in [33] and [35], FPGA-based controllers are connected to the metasurfaces to implement the computing functions. This layer comprises the computing hardware that controls the actuation and sensing elements. Its minimum computing duties include the mapping of local phase or impedance values to corresponding actuator states. Reflectarray tiles commonly implement this layer using FPGAs and shift registers [35].

Metasurfaces, and specifically, HyperSurfaces, can alternatively employ standard IoT devices for the same purpose. Moreover, they can optionally include computing hardware elements (ASICs) distributed over the tile meta-atoms [41, 42]. This can enable autonomous and cognitive tiles, where meta-atoms detect the presence and state, and correspondingly take local actuation decisions to meet a general functionality objective.

Communication plane

The communication plane passes signals from the processing layer to corresponding metasurface layer and collects signals from the sensing and actuation plane. In complicated programmable surface systems, communication occurs among planes to realize various EM wave control functions. The command signals normally operate at much lower fre-

quencies compared to the ones emitted from programmable surfaces; such signals prove to be more efficient in tuning the bias voltage of the PIN diodes [33].

This layer comprises the communication stack and connects actuation and sensing layer as well as computing layer with external devices such as controllers. In the simplest case, this layer is implemented within the computing hardware, acting as a gateway to the external world using any common protocol such as the Ethernet. HyperSurface tiles with embedded distributed computing elements additionally require inter-tile communication schemes, to handle the information exchange between smart meta-atoms. Both wired and wireless intra-tile communication is possible [41, 42].

1.2.4 Use cases

With the utilization of well-coordinated tiles in the Intelligent Communication Environments, the wireless system can be greatly improved in terms of communication efficacy.

On spectral efficiency enhancement

From the perspective of multiple users and moving users, the Intelligent Communication Environments are envisioned to serve a large number of users with more realistic user patterns, including mobile users and users in a cluster. Additionally, the system should ensure physical layer security against jamming and eavesdropping, an increasingly important problem that remains to be solved.

- *Transmission Distance:* For users in the non-light-of-sight (NLoS) areas relative to the transmitter, the Intelligent Communication Environments system is expected to extend the transmission distance and reach previously uncovered areas through waveguiding or reflection. Simulation results in [39] demonstrate that at 60 GHz the coverage can be extended to an entire NLoS area.

- *Interference Mitigation:* Due to the scenario with multiple users, there is inevitably concern of interference. As in the envisioned scheme, each functional unit, or a set

of such units, is dedicated to an individual user, thus the majority of interference will reside in the wireless section of the end-to-end link.

- *Reliability:* The primary efforts in terms of physical-layer reliability include using highly directional antennas to nullify jamming, forming exclusion areas, assigning secret keys to legitimate users, and so on. From the perspective of fundamental propagation channels with Intelligent Communication Environments, good reliability is achieved when the eavesdroppers do not have the knowledge of the frequencies where packages are transmitted, or the eavesdroppers are in the same frequency channel but with much higher noise which makes the intercepted data impossible to decode. Therefore, the dedicated links in Intelligent Communication Environments are inherently secure.

On physical-layer security improvement

The more frequent data exchange between users and service providers exposes a higher risk of personal and private data leakage. The 6G wireless network should not only inherit existing network secrecy measures, but also provide enhanced physical-layer security associated with new enabling techniques. In current 5G networks, highly directional beams are used for mmWave communications in spatial domain to prevent signals from being intercepted. However, a recent study has shown that such razor-sharp beams are still vulnerable to agile eavesdropping [43]. Other physical-layer encryption algorithms, including source coding approaches such as the low-density parity-check (LDPC) code, are demonstrated with optimal performance under specific conditions [44]. Furthermore, existing solutions in the reconfigurable intelligence surface utilize passive sub-wavelength reflectarrays, which do not have the capability to effectively distinguish target users from malicious attackers. Hence, a solution based on the Intelligent Communication Environments serves the purpose of identifying unintended recipients, creating null areas, and improving link secrecy rate.

Essentially, the envisioned Intelligent Communication Environments have the capability to sense user locations and exchange such information with a system controller to verify the user's authenticity. Only affirmative users shall be served with signal streams from the sender. On the other hand, connection requests from unauthorized users (i.e., eavesdroppers) will be nullified from attempting to access secure information or even trying to establish links with the sender.

In practice, the Intelligent Communication Environments can be configured to tune the phases of multipath components in the channel, such that those arrived at intended users can be coherently combined with boosted received signal strengths, whereas those intercepted by eavesdroppers will be scrambled or even cancelled due to non-coherent combining. Simulation results demonstrate a 6-dB attenuation observed at the received signal strength from the eavesdropper, validating the proposed physical layer security solution [45]. Hence, the good channel secrecy is achieved when such unintended users do not own the knowledge of equalizer to recover the transmitted signals from noise.

1.3 Research Objectives

Before the realization of terabits-per-second-level link in next-generation wireless communication systems, there still exist several open research challenges to be addressed. As discussed, a major challenge at mmWave and THz-band frequencies is posed by the very high propagation loss, which drastically limits the communication distance. Specifically, the free space path loss of a 10-meter link at THz frequencies can easily exceed 100 dB, which makes communication above tens of meters extremely challenging [46]. Random scatterers in the propagation channel also can block the dominant line-of-sight (LoS) path, causing the blockage issue or NLoS problem. On the one hand, the very high path loss arises from the spreading loss, which increases quadratically with the frequency, $\propto f^2$, as defined by the Friis' law. On the other hand, the molecular absorption loss, which accounts for the attenuation resulting from the fact that part of the wave energy is converted

into internal kinetic energy of the molecules in the propagation medium, also contributes to the path loss in the mmWave and THz bands [17]. Caused by oxygen and water vapor at the mmWave and THz frequency bands, respectively, the absorption peaks create spectral windows, which have different bandwidths and drastically change with the variation of the distance. Moreover, despite major developments, the transmission power of THz transceivers is still in the sub-milliwatt range, which further limits the transmission distance.

The objective of the thesis is to address the challenges in *distance limitation* and *NLoS problem* and pave the way for advanced solutions in the physical layer for wireless communication in the THz band, in both terrestrial and space communication systems. In particular, we focus on the following research items.

- *Design of UM MIMO-based Intelligent Communication Environments*

  The objective of this chapter is to theoretically design the UM MIMO platform aimed at increasing the communication distance and spectral efficiency at mmWave and THz-band frequencies. To realize this vision, the UM MIMO system in transmission and reception is designed and modeled. Plasmonic metamaterials and graphene will be utilized to design reconfigurable plasmonic antenna arrays able to support dynamic spatial beamforming and beam-steering. A new channel model accounting for peculiarities in the mmWave and THz wave propagation is developed and evaluated.

- *Beamforming and Beam-Steering Solutions for Intelligent Communication Environments*

  In this chapter, we focus on designing beamforming and beam-steering solutions at the access point (AP), the use equipment (UE), and the reconfigurable reflectarray in the environment, in order to improve the spectral efficiency and solve the NLoS problem. Metasurface-based intelligent communication environments usually employ a large number of antenna elements (e.g., on the order of a few hundreds), each

of which has limited antenna gains. In order to provide received signal strength improvement at end users, it is necessary to perform beamforming at the reconfigurable reflectarrays. Hence, desired beamforming vector design for maximizing beamforming gain is the research objective of this chapter. We further demonstrate that it is feasible to utilize the flexible dual-polarization unique in metasurfaces to achieve polarization diversity.

- *Path Tracking in Terahertz Band Communications*

  In order to utilize the THz band with its full potential, a good understanding of the characteristics becomes the priority for channel modeling and system design on the physical layer. In indoor environments, the most common communication scenario is the local area network, which requires the APs to provide satisfying connections to UEs. However, in mmWave and THz bands, the indoor channel is observed as non-stationary, since both the UE and random objects can be moving. Therefore, the conventional assumption of channel stationarity or quasi-stationarity is no longer valid for THz band communication. Additionally, the channel capacity is influenced by the molecular composition of the propagation medium and propagation distance, so a comprehensive three-dimensional (3D) channel model is required to describe the THz band. Hence, the research objective in this chapter is to perform dominant path tracking using an extended Kalman filtering approach. We demonstrate that the proposed solution can effectively track the line-of-sight (LoS) path in a typical indoor office environment.

- *Channel Modeling and Analysis of Inter-Small-Satellite Links*

  In current satellite communication systems, there is a lack of understanding of the propagation characteristics in the inter-satellite channel, which locates at the Earth's upper atmosphere (i.e., in the exosphere overlapping with the ionosphere) and in the deep space. Therefore, in this chapter, our research objective includes the channel

characterization and link design for both near-Earth and deep-space scenarios with an orbital perturbation model to analyze the spectral efficiency. In particular, we analyze the effect of Earth's upper atmosphere on near-Earth ISLs and solar activities on deep-space ISLs operated in the mmWave and THz bands. We characterize effects of the charged particles in both the ionosphere and in circumstance of solar wind. Furthermore, for deep-space links, we quantify the relationship between the angle of beam misalignment with the ISL's distance from the Sun. In addition, we study the relative motion between a pair of small satellites during formation flying and propose a model for orbital perturbation caused by gravitational force, Earth's oblateness, and solar radiation pressure. Based on characterization of inter-small-satellite channels and recognizing the potentials of polarization and frequency diversity in achieving high throughput, we propose a channel model that exploits these channel peculiarities and diversity schemes. In particular, we analyze the link metric of spectral efficiency under different link conditions, transmit power levels, and polarization configurations for the inter-satellite links.

- *Design of Multi-Frequency CubeSat in Satellite Communication Networks*

  In this chapter, we propose an initial CubeSat (i.e., a type of small satellites) design able to support multi-band wireless communication at microwaves, mmWave, THz band, and optical frequencies. Communication between satellites is needed both to enable the exchange of control and data information between CubeSats as well as to realize a globally connected network with ground infrastructure. Currently, conventional satellite networks as well as recently-deployed CubeSat networks rely on the use of specific frequency sub-bands in the microwave range, governed by the FCC and the International Telecommunications Union (ITU). The use of higher frequency bands has been less explored for active communication due to their much higher path loss and, thus, shorter transmission distance between satellites, which would have required the deployment of denser satellite constellations. However, the much lower

cost and development timeline of CubeSats open the door to considering higher frequency bands for communication, including the mmWave and THz bands. The research objective of this chapter is to devise a multi-band communication solution for CubeSats to meet the throughput requirements for inter-satellite data-intensive applications. This architecture can significantly leverage the capabilities of current CubeSat networks, and will be fundamental for future interplanetary CubeSat networks. We envision that the CubeSat networks will conceive the "*Internet of Space Things* (IoST)", a paradigm-shift architecture to leverage the cyber-physical system with another degree of freedom in the space for global process control and optimization.

1.4 Organization of This Thesis

The rest of the thesis is organized as follows. For the UM MIMO-based Intelligent Communication Environments, in Chapter 2, a propagation channel with controlled multipaths is modeled with performance evaluation on transmission distance maximization. In addition, practical design consideration with configuration overhead is analyzed to facilitate system design. Then, in Chapter 3, beamforming solutions are analyzed based on optimal continuous phase shifts and phase-gradient metasurfaces. Polarization diversity is also achievable on a basis of dual-polarized metasurfaces. Moreover, a tracking solution for the dominant path in the THz band channel is proposed in Chapter 4. For future small-satellite communication network operating at THz band, a channel model for inter-small-satellite communication is analyzed in Chapter 5, with orbital perturbation and environmental effects taken into consideration. Furthermore, a CubeSat design with multi-frequency communication potentials is described with link budget analysis in Chapter 6. Finally, the research contributions and future directions are summarized in Chapter 7.

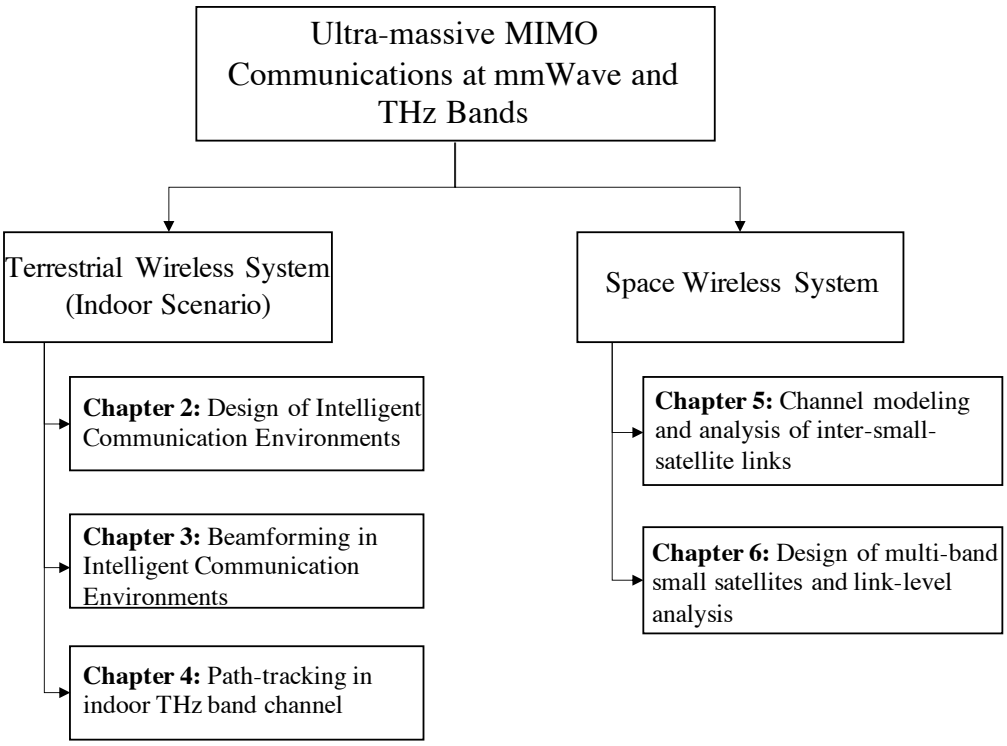

Figure 1.2: Organization of this thesis.

CHAPTER 2

DESIGN OF INTELLIGENT COMMUNICATION ENVIRONMENTS

In this chapter, we present the concept of Intelligent Communication Environments enabled by the ultra-massive multiple-input multiple-output (UM MIMO) communication platform as a solution to effectively increase the communication distance and throughput at mmWave and THz-band frequencies. The design of the Intelligent Communication Environments is motivated by reconfigurability of UM MIMO communication, in terms of both the utilization of advanced materials and the flexibility of its operation modes. Specifically, on one hand, the advanced engineered materials (e.g., metasurfaces), which can have negative refractive indices due to their unconventional chirality, are designed to build plasmonic antenna arrays with special EM functionalities, including non-specular reflection, wave absorption, polarization tuning, wave collimation, among others. These distinctive functionalities pave the way to a controllable propagation channel, where constructive paths can be enhanced while destructive paths can be suppressed. As a result, we show that the transmission range can be extended to more than 100 meters. On the other hand, as operating frequency increases, each antenna element becomes smaller in size, a larger number of elements are thus integrable within the same footprint, while preserving the same level of energy consumption.

2.1 Motivation and Related Work

The UM MIMO platform consists of reconfigurable plasmonic antenna arrays both at the transmitting and receiving nodes, operating as *plasmonic transceive arrays*, and in the transmission environment, in the form of *reconfigurable reflectarrays* and able to operate in different modes, including transmission, reception, reflection, and waveguiding. Plasmonic antennas leverage the physics of Surface Plasmon Polariton (SPP) waves to efficiently ra-

diate at the target resonant frequency while being much smaller than the corresponding wavelength [47]. This particular property allows them to be integrated in very dense arrays, beyond traditional antenna arrays, and enables the precise radiation and propagation control of EM waves with sub-wavelength resolution.

In order to better utilize the abundant spectrum resources in the mmWave and THz bands, it is of significant importance to address some important challenges in the physical layer. One of the major challenges is the limited communication distance because of high path loss inherent to small wavelengths and the limited transmission power of mmWave and THz-band transceivers [20]. To overcome this problem, high-gain directional antenna systems are needed. Besides, reconfigurable antenna arrays can be utilized to implement MIMO and massive MIMO communication systems. When increasing the communication frequency, antennas become smaller and, thus, a higher number of antennas can be integrated within the same footprint. However, simply increasing the number of antennas is not sufficient to overcome the much higher path loss as we move towards the THz band and to meet the demands and expectations of beyond 5G systems.

In previous studies of UM MIMO communication system enabled by plasmonic antenna arrays [2, 48], such antennas [47, 49, 50] leverage the physics of surface plasmon polariton (SPP) waves, i.e., confined EM waves resulting from the global oscillations of electrons at the interface of a conductor material and a dielectric material, to efficiently radiate at the target resonant frequency while being much smaller than the corresponding wavelength. This property allows them to be integrated in very dense arrays, beyond traditional antenna arrays. The ratio between the free-space wavelength λ and the SPP wavelength λ_{SPP} is known as the plasmonic confinement factor, and depends on the plasmonic material properties and the operation frequency. The higher the confinement factor, the smaller the antennas and the higher the density in which they can be integrated. In current literature, some other commonly used materials for constructing controllable wireless communication environments are reflectarrays and metasurfaces. In this section, we first

elaborate on the physical properties of these materials and corresponding functionalities that can be utilized in the controllable surfaces, then we discuss the layered structure that supports these functionalities.

Based on the fundamentals of reflectarrays and metasurfaces, recent research has found great potentials of them in constructing the software-defined metamaterials (SDMs), or programmable metamaterials [51, 30, 29, 52, 20, 39]. Some related works focusing on the system-level architecture and associated functionalities have been reported, where an overview on the state-of-the-art in the general controllable surfaces is shown briefly in Table 2.1.

Table 2.1: Overview on Current Research in Controllable Surfaces.

Name of Surface	Metamaterial Plane	Sensing & Actuation Functionalities	Computing Functionality	Communications Across Layers
VisorSurf HyperSurface [30]	Graphene-based or CMOS switches	Integreted sensors	Massive manycores, infinitesimal computing, and approximate computing algorithms	Network-on-chip and nanonetworking
Digital Coding Metasurfaces [33]	Space-time-coding metasurfaces with elements connected via biasing lines	Actuation realized by a control voltage loaded to PIN diodes	Frequency-dependent phase and amplitude tuning	Wired connection between FPGA and metasurfaces
Smart Reflectarray [34]	Reflectarray antennas	Reflectorarrays are controlled by a bias voltage to tune the varactors	No computing in passive reflectarrays	Controller to passive reflectarrays
Intelligent Reflecting Surface [31]	Reflectarray antennas	Controller-based sensing & reflecting modes	No computing in passive reflectarrays	Controller to passive reflectarrays
Programmable Metasurface [35]	Unit cell with a rectangular-shaped patch and a metal-ground plane	Actuation enabled by a control voltage applied on PIN diodes	FPGA-based control board connected to sub-metasurface	Wired connection through computer, control board, and metasurfaces

2.1.1 Reflectarrays

Reflective array antennas, or reflectarrays, are a popular candidate for controllable surfaces. The essential functionality of a reflectarray is to form a prescribed radiation pattern generated by a group of individual reflector antenna elements. In general, reflectarrays contain a feed antenna and a number of antenna elements which are mounted on top of a substrate surface according to certain patterns or shapes. A reflector can effectively help to improve the front-to-back ratio by not adding the signals from the rear direction to the ones received in front of the reflectarrays.

Reflectarrays can be categorized based on the number of layers, the number of reflecting surfaces, types of polarization, or the extent of dynamic beam reconfigurability. According to the criterion on the extent of reconfigurability of reflectarray beams, two groups of reflectarrays can be classified: fixed-beam reflectarrays which are passive and reconfigurable reflectarrays which are considered active. For the purpose of controllable surface implementation, the reconfigurable reflectarrays are taken into consideration, where controllable mechanisms at the antenna element level is introduced in order to modify the phase shift and to reconfigure beams.

Reflectarrays have been widely utilized in radars, point-to-point links, and satellite communications because of their flexibility and low cost [53]. Based on principles of phased arrays and geometrical optics, electronically tunable reflectarrays can realize dynamically adjustable radiation patterns. Specifically, the phase shift of each element in the reflactarray can be controlled electronically and will jointly form an array pattern to receive or transmit the signal to or from desired directions. Compared to phased arrays that require complicated phase shifter circuits and suffer from high transmission line loss at mmWave frequencies, reflectarrays are simpler in mass production and have higher energy efficiency because there is no need for transmission lines. Since under communication scenarios where receivers are expected to move, antenna arrays should also be flexibly adjustable in order to keep a satisfying SNR at the user end.

In environments with scattered multipaths at mmWave bands, reflectarrays can be deployed to serve single and multiple transmitter and receiver pairs to communicate simultaneously and to extend the transmission range. For example, in an indoor environment where the direct path from a transmitter to a receiver is blocked, a reflectarray close to the access point can be used as a reflector to bounce off the signal towards the UE. The reflectarray can dynamically tune the phase of the elements that can sense the transmitted signal to direct the reflected rays towards the users, without any complicated signal processing techniques at the UE side. Additionally, since multiple reflectarray elements will form sharp beams targeting specific users, the interference among users can be suppressed. Reflectarrays can be installed close to access points, or around turning points or blockage areas.

However, reflectarrays also show some limits in their application. First, the efficiency of electronic tuning is highly dependent on the array size and the characteristics of the environment. Especially in mmWave frequencies where the signal transmission paths can be easily distorted by any movement in the environment, the time efficiency and accuracy of channel estimation is critical in providing satisfying link quality to users. Second, at mmWave band the material for building reflectarrays needs to be reconsidered because that 120 GHz is deemed as the upper limit for MEMS which are the most commonly seen in current antenna architecture [53].

In [34], the authors proposed a smart reflectarray solution for new spectrum sharing in indoor environments. The reconfigurable reflectarray can be controlled via phase shift of each element in order to cancel interference or to enhance useful signals. The smart reflectarray can operate with microstrip antennas connected to electronically-controlled capacitors. There is a micro-controller to control the reflectors on their electromagnetic response sto the signals impinging on them. By tuning the phase of the reflectors which can add multipaths in-phase or canceling each other towards a user, the signal level can be boosted or diminished. This design shows potentials for reflectarrays to be utilized in ap-

plications on physical layer security and mitigating interference problem. A similar design named "Intelligent Reflecting Surfaces" in [31] has been proposed to use reflectarrays to enhance indoor wireless communication performance proved by theoretical analyses and simulations.

2.1.2 Metasurfaces

A metasurface is a planar, artificial structure which comprises a repeated element, the meta-atom, over a substrate. In most common compositions, the meta-atom is conductive and the substrate is dielectric. Common choices are copper over silicon, while silver and gold constitute other exemplary conductors [54]. Metasurfaces are able to control EM waves impinging on them, in a frequency span that depends on the overall dimensions. The size of the meta-atom is much smaller than the intended interaction wavelength (λ), with $\lambda/10$–$\lambda/5$ constituting common choices. The thickness of the metasurface is also smaller than the interaction wavelength, ranging between $\lambda/10$ and $\lambda/5$ as a rule of a thumb. Metasurfaces usually comprise a dense population of meta-atoms per unit area, which results into fine-grained control over the EM interaction control. In general, a minimum size of approximately 30×30 meta-atoms is required to yield an intended EM interaction [38]. Figure 2.1a) illustrates a well-studied metasurface design comprising split-ring resonators as the meta-atom pattern. Such classic designs that rely on a static meta-atom, naturally yield a static interaction with EM waves. The need for dynamic alteration of the EM wave control type has given rise to dynamic metasurfaces, illustrated in Figure 2.1b). Dynamic meta-atoms incorporate phase switching components, such as MEMS, CMOS transistors or microfluidic switches, which can alter the structure of the meta-atom. Thus, dynamic meta-atoms allow for time-variant EM interaction, while meta-atom alterations may give rise to multi-frequency operation [54]. Phase-switching components can also be classified into state-preserving or not. For instance, mechanical or micro-fluidic switches may retain their state and require powering only for state transitions, while semiconductor switches

require power to maintain their state.

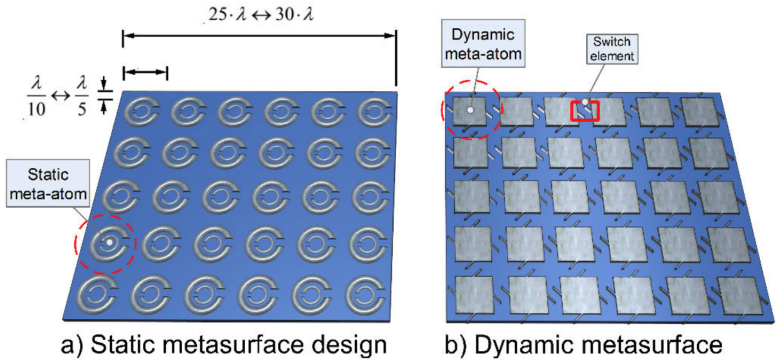

Figure 2.1: Split ring resonators (left) constituted a very common type of static metasurfaces, with fixed EM behavior. Novel designs (right) incorporate switch elements (MEMS, CMOS or other) to offer dynamically tunable EM behavior [45].

In the following subsections, we provide a synopsis of existing controllable surfaces.

VisorSurf HyperSurfaces

The layered structure to enable various operation modes of metasurfaces is given in Figure 2.2. The meta-atoms can have different shapes, including the shown split-ring structure and more complicated ones [52]. The total EM response of the metasurface is then derived as the total emitted field by all surface currents, and can take completely engineered forms, such as phase shift, polarization tuning, and so on. In fact, the meta-atoms can be viewed as either input or output antennas, connected in custom topologies via the switch elements. Impinging waves enter from the input antennas, get routed according to the switch element states, and exit via the output antennas, exemplary achieving customized reflection.

A metasurface can support a wide range of EM interactions, as shown in Figure 2.2, which can be categorized as follows,

- **Phase Shift:** Modifying the phase of impinging waves to enhance constructive multipath components and cancel destructive ones (as shown in Figure 2.2(a)).

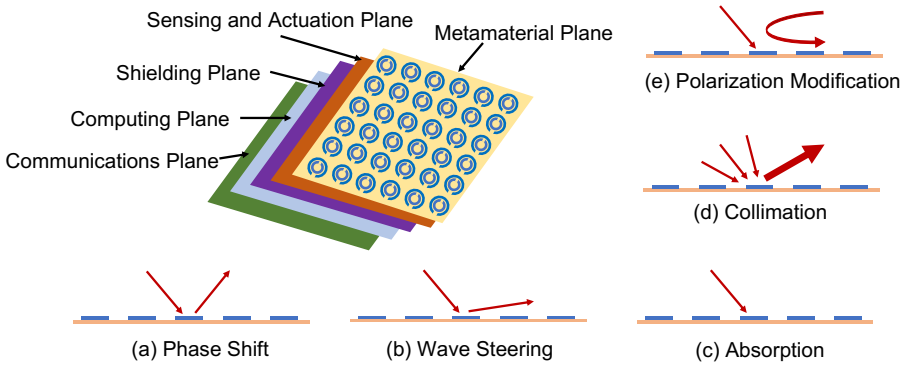

Figure 2.2: Illustration of the layered structure of metasurfaces and the enabling operation modes [52].

- **Wave Steering:** Reflection of an impinging wave, with a given direction of arrival, towards a completely custom direction. Refraction of EM waves via the metasurface towards any inwards direction. Both the reflection and refraction functions can override the outgoing directions predicted by Snell's law (as shown in Figure 2.2(b)).

- **Wave Absorption:** Absorbing waves to minimize reflected and/or refracted power for impinging waves (as shown in Figure 2.2(c)).

- **Wave Collimation:** Impinging waves from different directions can be collimated towards the same outgoing direction in order to enhance signals towards intended users, mitigate interference, and reduce probability of interceptions and detection (as shown in Figure 2.2(d)).

- **Polarization Modification:** Changing the oscillation orientation of the wave's electric and magnetic field. This can be modified between parallel and vertical polarizations and between linear and circular polarizations (as shown in Figure 2.2(e)).

Metasurfaces constitute the state-of-the-art in EM wave control in terms of capabilities and control granularity, which can be exploited in a variety of applications, such as in wide-band communications, highly efficient energy harvesting photovoltaics, and thermophotovoltaics, ultra-high resolution medical imaging, sensing, quantum optics and military applications [55].

Beside the intelligent surfaces which target to control the electromagnetic behavior of the environment or with sub-wavelength resolutions, recent research advances are aimed at controlling the characteristics of the propagation environments in order to improve the transmission distance and solve the non-line-of-sight (NLoS) problem. In the near future where IoT connects billions of devices, the reflectarrays and HyperSurfaces will serve as optimal solutions to satisfy the exponential growth in system throughput. Use cases include indoor meeting rooms or corridors with multiple sensors and devices connected and a single AP cannot satisfy the connectivity requirements, as shown in Figure 2.3.

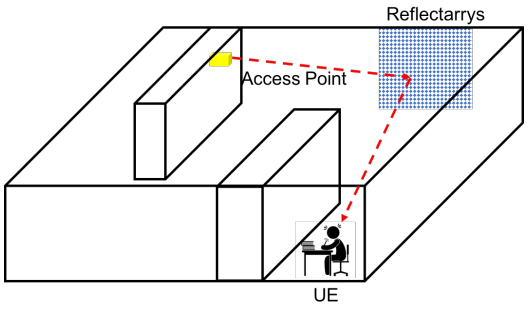

Figure 2.3: An illustration of an indoor use case of reflectarrays where the user equipment (UE) is in non-line-of-sight of the access point.

The HyperSurface is a new type of planar metasurface which can be coated on the surface of indoor environments and can be controlled via software programs to change its EM behavior. The key technology is enabled by metasurfaces, which consist of hundreds of element called meta-atoms, a conductor with the size smaller than half wavelength. Metasurfaces can control the EM waves that impinge on it at certain frequency bands at a very high spatial resolution. These elements are networked by a set of miniaturized controllers that connect the switches of the metasurfaces and a gateway serves as the connectivity unit to provide inter-element and external control [29]. The signal propagation routes can be optimized for each communication link with the novel design of HyperSurface tiles using metamaterials. Compared to reflectarrays, metasurfaces can exhibit unconventional electromagnetic properties by interacting with electromagnetic waves at a sub-wavelength scale. Metasurfaces allow one to manipulate incoming waves in ways that are not possi-

ble with conventional reflectarrays, including wave steering, wave absorption, and wave polarization [29].

Digital Coding Metasurfaces

The work in [33] proposed theoretical space-time modulated digital coding metasurfaces to control the EM waves in both space and frequency domains. The digital coding metasurfaces have the original structure of using two coding elements with opposite reflection phases (e.g., 0° and 180°) to represent digital bits "0" and "1". Further, the number of bits can be doubled by utilizing more phases of reflection, such as 0°, 90°, 180°, and 270°, in addition to the original two, which can finally achieve a two-bit digital code series of "00", "01", "10", and "11". The encoding and managing process can be implemented via a field-programmable gate arrays (FPGAs). Additionally, time-modulated metasurfaces have another degree of freedom in manipulating EM waves to improve the system efficiency.

The prototype design of such metasurfaces includes an array of 8×8 elements connected by biasing lines and shared a common control voltage. A coding element is composed of a rectangular-shaped metal patch printed on a grounded dielectric substrate, with a size of 15 mm $\times$ 15 mm. The sensing and actuation functionalities are realized by the control voltage loaded to the PIN diodes, and the communication functionality which is responsible to manipulate the behavior of metasurface element is realized by the wired connection between FGPA and the surface plane [33]. In order to manipulate the impinging EM waves, the digital coding metasurfaces can realize harmonic beam steering which is similar to adding a time shift t_q to the Fourier transform $\exp\left(-j2\pi f_0^{(m)} t_q\right)$ where $f_0^{(m)}$ is the resultant m-th harmonic frequency. Additionally, beam steering and shaping can also be achieved at the central frequency f_c by utilizing the 2-bit phase modulation scheme. Hence, the power radiation pattern of the metasurface arrays can be controlled according to the digital bits while maintaining a constant front-to-back ratio. Besides, the metasurfaces can also use similar approaches to alter phases at different harmonics in order to modify

the output signal amplitude, thus increasing or decreasing the main lobe's power.

Programmable Metasurface

A similar design to the digital coding metasurfaces, named "programmable metasurface", has been reported in [35], which can achieve dynamic control over polarization, scattering, and signal focusing. Different from the aforementioned design, this programmable metasurface utilizes a binary-coding-based genetic algorithm to optimize the coding matrix. This approach is proven to be efficient when the size of metasurface grows very large. This proposed programmable metasurface has the structure of five identical sub-metasurfaces, each of which consists of 320 active unit cells. Polarization is formed with reconfigurable phase by integrating a PIN node into each unit cell. Hence, a polarization conversion can be realized by voltage change induced on each unit.

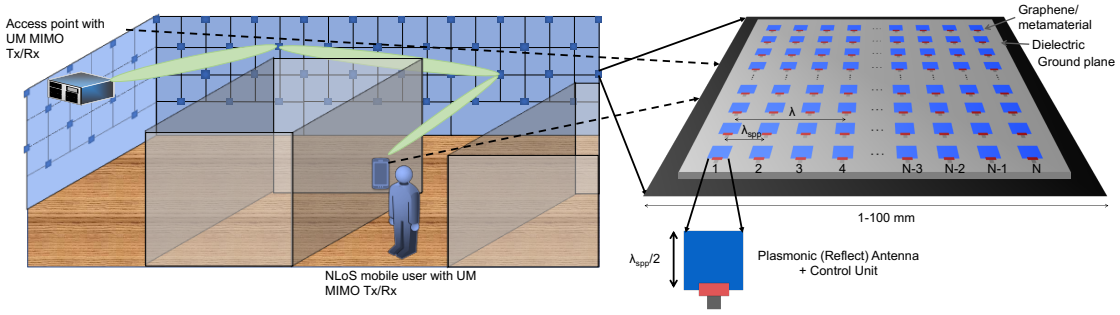

Figure 2.4: Illustration of intelligent environments based on UM MIMO plasmonic antenna arrays.

2.2 UM MIMO-Based Intelligent Communication Environments

Starting from this section, we describe our design of the UM MIMO-based Intelligent Communication Environments for mmWave and THz bands. UM MIMO platforms enable the creation of intelligent communication environments in both indoor and outdoor scenarios. With the derivations readily extendable to the outdoor case, in this chapter, we focus our modeling and analysis in the indoor case. The intelligent environments consist of

two major parts: the plasmonic antenna arrays at the transceivers (i.e., the transmitter and the receiver) and the reconfigurable reflectarray systems in the propagation environment. As illustrated in Figure 2.4, the reconfigurable reflectarrays can be embedded or applied to surfaces of indoor objects (e.g., walls and ceilings) like adhesive foil papers. Such reconfigurable reflectarrays, due to their small footprints, can locate at multiple places and perform controlled reflection towards another reflectarray or the receiver, depending on their proximity to the receiver and based on allocated resources.

2.2.1 A tri-layer structure of reconfigurable reflectarray

Distinct from the plasmonic antenna arrays at the transceiver side, the reconfigurable reflectarray in the environment adopts a three-layer structure, which is cost-effective and requires lower energy consumption.

The top layer, or the surface layer, consists of a planar array of plasmonic antenna elements. At mmWave frequencies, these antenna elements can be metamaterial-based subwavelength scatterers, such as split-ring resonators or metasurface patch elements, which have a size ranging in $\lambda/10$ to $\lambda/5$ (λ being the free-space wavelength). At THz band, such antenna elements are plasmonic patches suitable for operation in these higher frequencies, such as graphene-based plasmonic antenna with a dimension on the level of $\lambda/20$. The physics of plasmonics can be utilized to enable antenna arrays with much denser elements and go beyond the conventional $\lambda/2$ sampling of space towards more precise space and frequency beamforming. On that basis, it has been demonstrated that, at THz frequencies, graphene can be used to build nano-transceivers and nano-antennas with maximum dimension $\lambda/20$, allowing them to be densely integrated in very small footprints (1024 elements in less than 1 mm^2), as shown in Figure 2.4 [47, 21]. However, graphene does not perform well at mmWave bands. Instead, we consider to incorporate metasurfaces into the plasmonic transmit-receive arrays. Metasurfaces, the 2D representation of metamaterials which are a type of engineered material designed to exhibit EM properties not commonly found

in nature, have been well studied from the perspective of material science and technology [56]. The understanding of the benefits of utilizing them in transmission and reception from the communication perspective is missing and hence motivates this work.

The middle layer of the reconfigurable reflectarray is the control layer. The main function of this layer is to perform phase and amplitude control of the associated plasmonic antenna elements. By controlling the amplitude and phase shift of each element, the plasmonic layer can achieve controlled functionalities, which include controlled/anomalous reflection and wave absorption, as illustrated in Figure 2.5. In terms of hardware design, such control is realized by tuning the Fermi energy level of each plasmonic antenna element at THz band or tuning the bias voltage of the PIN diodes in mmWave frequencies [57].

The bottom layer of the reconfigurable reflectarray is the waveguiding layer, which is unique in plasmonic antenna arrays at THz band, due to the propagation of SPP waves at the interface between dielectric and air or metal medium. The waveguiding layer can pass along the absorbed energy to another plasmonic antenna element for re-radiation. The waveguiding functionality is promising for use cases where the path formed by the main beam of one reconfigurable reflectarray might be blocked and the SPP wave can propagate to an adjacent plasmonic reflectarry without being re-radiated in the wireless channel. Such functionality requires that multiple reconfigurable reflectarrays are deployed close to each other.

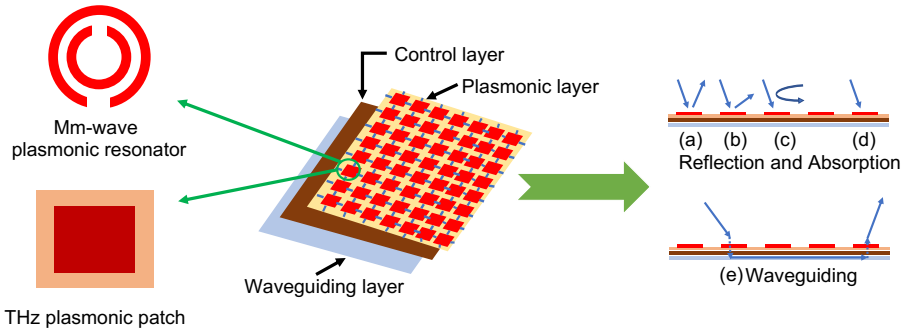

Figure 2.5: Conceptual design of a reconfigurable reflectarray able to unconventionally manipulate EM waves, including (a) specular reflection; (b) controlled reflection; (c) reflection with converted polarization; (d) absorption; and (e) signal waveguiding.

2.2.2 Reconfigurable reflectarrays in the Intelligent Communication Environments

The reconfigurable reflectarrays can be deployed freely in the 3D environment. Assuming a square-shaped array layout, the size of each reconfigurable reflectarray A is a function of the number of antenna element on each side N, the plasmonic confinement factor γ, as well as the operation wavelength λ, expressed as $A = \left(\frac{N\lambda}{\gamma}\right)^2$ [2]. The confinement factor is defined as the ratio between the free-space wavelength λ and the SPP wavelength λ_{SPP}, and depends on the plasmonic material properties and the operation frequency. The density of integratabtle plasmonic antenna elements increase monotonically with the confinement factor. Hence, depending on the operation frequency in the mmWave and THz bands, hundreds of or more than one thousand plasmonic antenna elements can be integrated with a size ranging from 1 mm^2 to 100 mm^2.

Owing to the sub-wavelength size of their elements, the reconfigurable reflectarrays are able to reflect signals in non-conventional ways, which include controlled reflections in non-specular directions as well as reflections with polarization conversion [58], as illustrated in Figure 2.5. These operations can be achieved by properly tuning the reflection coefficient Γ of the meta-atoms. To be more specific, suppose a pair of incident and reflected signal has the following wave vectors,

$$\mathbf{E}^{\text{i}} = \left(E_x\hat{x} + E_y\hat{y}\right) e^{i(-\omega z/c+\omega t)}, \tag{2.1a}$$

$$\mathbf{E}^{\text{r}} = \Gamma\left(E_x\hat{x} + E_y\hat{y}\right) e^{i(\omega z/c+\omega t)}, \tag{2.1b}$$

where ω is the angular frequency. The reflection coefficient Γ can be written as

$$\begin{aligned}\Gamma &= \mathbf{E}^{\text{r}}/\mathbf{E}^{\text{i}} \\ &= \Gamma e^{i(2\omega z/c)} \\ &= \Gamma e^{i\Phi(z)},\end{aligned} \tag{2.2}$$

where Γ is the reflection coefficient at the boundary of two materials and the wave propagation is along the z-axis. We can further express the phase component of the reflection coefficient as a function between the angles of incidence and reflection,

$$e^{i\Phi(z)} = e^{i(\sin\theta_\mathrm{i} - \sin\theta_\mathrm{r})\omega z/c}, \tag{2.3a}$$

$$\begin{aligned} \frac{d\Phi}{dz} &= \omega/c\,(\sin\theta_\mathrm{i} - \sin\theta_\mathrm{r}) \\ &= k\,(\sin\theta_\mathrm{i} - \sin\theta_\mathrm{r})\,, \end{aligned} \tag{2.3b}$$

where $k = \omega/c = 2\pi/\lambda$ is the wave number. It is obvious that when the phase gradient is zero, the angle of reflection equals the angle of incidence, following a specular reflection. However, when the phase gradient has a non-zero value, the angle of reflection is different from the angle of incidence, with respect to the normal of the impinging plane. Hence, by altering the phase component, the reflected signals can be tuned to a desired direction. If we extend the scenario to an impinging wave from an arbitrary direction on the x-y plane, as shown in Figure 2.6, the relationship between the incident and reflected angles can be expressed as

$$\sin\theta_r\cos\phi_r - \sin\theta_i\cos\phi_i = \frac{1}{kn_i}\frac{d\Phi}{dx}, \tag{2.4a}$$

$$\sin\theta_r\sin\phi_r - \sin\theta_i\sin\phi_i = \frac{1}{kn_i}\frac{d\Phi}{dy}, \tag{2.4b}$$

where n_i is the refractive index of the incidence medium and its value equals 1 in air.

The polarization conversion can be achieved by altering the reflection coefficients along two orthogonal directions in anisotropic meta-atoms [59], where the wave vector of reflected wave is expressed as

$$\mathbf{E}^\mathrm{r} = (\Gamma_x E_x\hat{x} + \Gamma_y E_y\hat{y})e^{i(\omega z/c + \omega t)}. \tag{2.5}$$

One step further, the absorption of incident EM waves can be maximized in metasurfaces

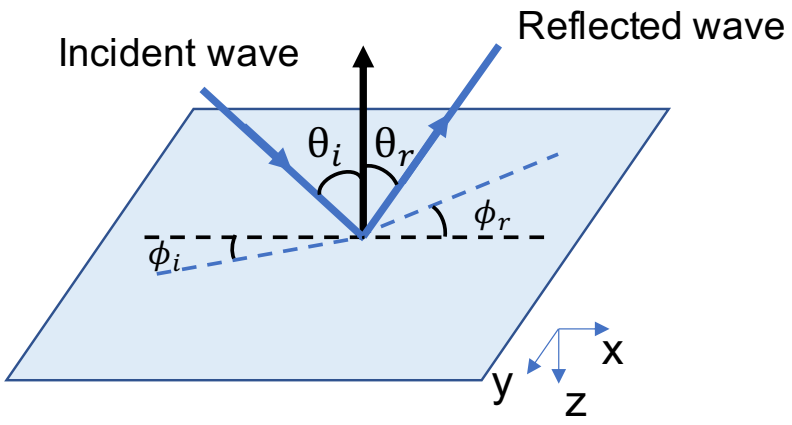

Figure 2.6: Controlled reflection of an impinging wave on the x-y plane.

with proper size and thickness selections of the meta-atoms, when the impedance matching with free space and transmission is minimized. According to conservation of energy, the absorptivity β can be maximized when the reflectivity R is minimized (suppose transmission via refraction is blocked by utilizing a metallic back plate, thus $T = 0$), where we have

$$\beta = 1 - R = 1 - \left| \frac{\mu_r - n}{\mu_r + n} \right|^2, \tag{2.6}$$

in which the refractive index n is a function of the relative permittivity μ_r and permeability ε_r, expressed as $n = \sqrt{\mu_r \varepsilon_r}$.

2.3 System Model

The realization of UM MIMO communications requires the development of a channel model that is able to capture the effect of the reconfigurable reflectarrays with controlled multipaths propagating in space. In this section we explore these characteristics. In particular, we first develop an end-to-end channel model, then we describe the plasmonic array design, and we analyze the performance in terms of transmission distance maximization.

2.3.1 Channel Impulse Response

In the propagation channel, the transmitter sends out signals in the propagation environment, which interact with objects or propagate in free space before reaching the receiver. These interactions include reflection, diffraction, and scattering. Existing channel modeling approaches normally treat the environments as passive channels, where equalization has to be performed at the receiver to combat the inter-symbol interference (ISI). However, with the deployment of the plasmonic arrays in the environment, these interactions become controllable, which can be reflected with tuned phase or totally absorbed before reaching the receiver. Hence, such reconfigurable reflectarrays can manipulate the paths in the environments to enhance signal transmission and diminish the effect of ISI. In the time domain, the channel with all multipaths can be characterized based on a narrowband indoor multipath model [60] as follows,

$$\begin{aligned} h(t) =& \alpha_{\mathrm{LoS}} \exp(-j\varphi_{\mathrm{LoS}})\delta(t-\tau_{\mathrm{LoS}})\mathbb{1}_{\mathrm{LoS}} \\ &+ \sum_{m=1}^{M} \alpha_m \exp(-j\phi_m)\delta(t-\tau_m) \\ &+ \sum_{s=1}^{S} \alpha_s \exp(-j\phi_s)\delta(t-\tau_s) \\ &+ \sum_{r=1}^{R} \alpha_r \exp(-j\phi_r)\delta(t-\tau_r) \\ &+ \sum_{w=1}^{W} \alpha_w \exp(-j\phi_w)\delta(t-\tau_w), \end{aligned} \tag{2.7}$$

in which $\alpha_{(\cdot)}$ denotes the amplitude of paths in different types, including the line-of-sight (LoS) path and multipath components (MPCs) that stem from absorption and other effects. The first term on the right-hand side of the equation denotes the LoS path with $\mathbb{1}_{LoS}$ as the presence indicator function. The second term represents the MPCs in conventional wireless environments (i.e., reflection/diffraction/scattering with natural materials in the channel),

and the third to fifth terms denote the MPCs undergone controlled absorption, controlled reflection, and waveguiding through reconfigurable reflectarrays, respectively. $\phi_{(\cdot)}$ denotes the phase of each multipath undergone the channel effects, $\tau_{(\cdot)}$ is the time of arrival of each multipath, subscripts s, i, w denote the indices of paths being absorbed, reflected, and waveguided, respectively.

Depending on different use cases, such as spectral efficiency maximization, physical-layer security, among others, the reconfigurable reflectarrays can be tuned to maximize reflectivity or maximize absorptivity. Under proper tuning of the reconfigurable reflectarrays' phase shifts to maximize their absorptivity, $\alpha_s \approx 0$, which means the MPCs that can cause inter-symbol interference or are detectable by unauthorized users will be absorbed. In this chapter, we focus on the case to maximize the spectral efficiency, or equivalently, to maximize the controlled reflection towards the desired UE in NLoS areas in the channel.

The amplitude of reflected path depends on the frequency and corresponding free-space path loss. In the THz band, it is also affected by the spreading loss and molecular absorption loss [17], and in the controlled reflection upon reconfigurable reflectarrays, it is also subject to the impinging reflection amplitude gain I ($I \in [0, 1]$)[1]. Since our focus in this chapter is to assess the potentials of the Intelligent Communication Environments, we can extend α_r in the manner of an end-to-end link (i.e., from AP to the reconfigurable reflectarray and then reflection from the reconfigurable reflectarray to the UE) as

$$\alpha_r^{(T)} = \frac{\lambda}{4\pi d_T} \exp\left(-\frac{\mathcal{K}(f) d_T}{2}\right) \exp\left(-j2\pi f \tau_r^{(T)}\right), \tag{2.8a}$$

$$\alpha_r^{(R)} = \frac{\lambda}{4\pi d_R} \exp\left(-\frac{\mathcal{K}(f) d_R}{2}\right) \exp\left(-j2\pi f \tau_r^{(R)}\right), \tag{2.8b}$$

where d_T and d_R are the path lengths in two segments: from AP to reflectarray and from the reflectarray to the UE, respectively. $\mathcal{K}(f)$ is the frequency-dependent molecular absorption coefficient, which is a summation over all gases in presence of a medium and is further

[1] with the ideal lossless reflection when $I = 1$ and full absorption when $I = 0$

expressed as

$$\mathcal{K}(f) = \sum_i \frac{\zeta}{\zeta_0} \frac{T_{\mathrm{STP}}}{T} \Omega^i \xi^i(f), \tag{2.9}$$

where ζ is the system pressure, T the ambient temperature, ζ_0 the reference pressure, T_{STP} the temperature at standard pressure, Ω^i the number of molecules per volume unit of gas i, and $\xi^i(f)$ the absorption cross-section of gas i at corresponding frequencies [17]. The resultant path gain from the controlled reflection is the product of the two terms, which is

$$\alpha_r = \alpha_r^{(T)} \alpha_r^{(R)}. \tag{2.10}$$

In the frequency domain, the channel transfer matrix $\mathbf{H}$ between the AP and UE via controlled reflection over the reconfigurable reflectarray can be expressed as

$$\mathbf{H} = \mathbf{H}_{\mathrm{R}} \mathrm{P} \mathbf{H}_{\mathrm{T}}, \tag{2.11}$$

where $\mathrm{P} = \mathrm{diag}\left[\rho_1 \exp(j\varphi_1), ..., \rho_M \exp(j\varphi_M)\right]$ is the amplitude and phase shift matrix of the reconfigurable reflectarray with $\rho \in [0, 1]$ and $\varphi \in [0, 2\pi)$. In particular, the channel transfer matrix between the AP and the reconfigurable reflectarray, denoted as $\mathbf{H}_{\mathrm{T}}$ and that between the UE and the reconfigurable reflectarray, denoted as $\mathbf{H}_{\mathrm{R}}$, can be further elaborated as

$$\mathbf{H}_{\mathrm{T}} = \sqrt{N_t M} \alpha_r^{(T)} \mathbf{a}_{\mathrm{P}}\left(M, \theta_a, \phi_a\right) \mathbf{a}_{\mathrm{T}}^*\left(N_t, \theta_t, \phi_t\right), \tag{2.12a}$$

$$\mathbf{H}_{\mathrm{R}} = \sqrt{N_r M} \alpha_r^{(R)} \mathbf{a}_{\mathrm{R}}\left(N_r, \theta_r, \phi_r\right) \mathbf{a}_{\mathrm{P}}^*\left(M, \theta_{ar}, \phi_{ar}\right), \tag{2.12b}$$

where $\theta_{(\cdot)}$ and $\phi_{(\cdot)}$ denote the angles in elevation and azimuth planes, with subscripts r, ar, a, and t representing the receiving, anomalously reflected, arriving, and transmitting angles, respectively, $\mathbf{a}_{\mathrm{T}}$, $\mathbf{a}_{\mathrm{R}}$, and $\mathbf{a}_{\mathrm{P}}$ denote the array steering vectors of these aforementioned angles at the AP, the UE, and the reconfigurable reflectarray, respectively, which can be expressed

as (here we use $\mathbf{a}_{\mathrm{P}}$ as an example)

$$\begin{aligned}\mathbf{a}_{\mathrm{P}} = \big[1 \ \ldots \ e^{(jkm_x\Delta_x \sin\theta_a \cos\phi_a + jkm_y\Delta_y \sin\theta_a \sin\phi_a)} \ \ldots \\ e^{(jk(M_x-1)\Delta_x \sin\theta_a \cos\phi_a + jk(M_y-1)\Delta_y \sin\theta_a \sin\phi_a)}\big]^{\mathsf{T}},\end{aligned} \tag{2.13}$$

where $M = M_x M_y$, with M_x and M_y denote the number of plasmonic antenna elements along the x- and y-axis, Δ_x and Δ_y are the element spacing values along the x- and y-axis when we assume the uniform planar array is in the xy-plane.

2.3.2 Received Signal Model

Suppose the Intelligent Communication Environments include an AP with N_t antennas, a reconfigurable reflectarray with M antennas, and a single user with N_r antennas. In our current study, we assume there is only one reconfigurable reflectarray in the environment to serve the controlled propagation between the AP and the UE in order to overcome the NLoS problem. Hence, to compensate for the high path loss while maintaining a practically achievable architecture, both the AP and the UE will perform analog beamforming and combining using phase shifters. Therefore, at the receiver side, the received signal can be expressed as

$$\begin{aligned} y &= \mathbf{w}_{\mathrm{R}}^{*}\mathbf{H}\mathbf{w}_{\mathrm{T}}x + n \\ &= \mathbf{w}_{\mathrm{R}}^{*}\mathbf{H}_{\mathrm{R}}\mathrm{P}\mathbf{H}_{\mathrm{T}}\mathbf{w}_{\mathrm{T}}x + n, \end{aligned} \tag{2.14}$$

where x is the transmitted signal with $\mathbb{E}[|x|^2] = P_t$ where P_t is the transmit power,and $n \sim \mathcal{N}_c(0, \sigma^2)$ is the additive white Gaussian noise at the UE side. $\mathbf{w}_{\mathrm{R}}$ is the beamforming vector at the UE with $|w_{\mathrm{R}}[i]| = \frac{1}{\sqrt{N_r}}$, $i = 1, ..., N_r$, and $\mathbf{w}_{\mathrm{T}}$ is the beamforming vector at the AP with $|w_{\mathrm{T}}[i]| = \frac{1}{\sqrt{N_t}}$, $i = 1, ..., N_t$, the details of which will be discussed in Chapter 3. By properly designing the beamforming and combining vectors at the AP and UE, we can steer the high-gain narrow beams towards the strongest propagation path. Thus, the effective UM MIMO channel is transformed into a single-input single-output (SISO) channel in a single-user single-stream case. Hence, the received signal power at the receiver

side is expressed as

$$P_{\mathrm{R}} = P_t |\alpha_r^{(T)}|^2 |\alpha_r^{(R)}|^2 |\mathrm{AF_t AF_r AF_P}|^2. \tag{2.15}$$

With channel knowledge known by the AP, the beam from the AP to the plasmonic array can be steered towards the direction pointing towards the array, with angles θ_0 and ϕ_0, which aligns with the LoS path between the AP and the reconfigurable reflectarray. The distance between the AP and the reconfigurable reflectarray is assumed to be fixed. The transmission distance maximization problem is transformed to maximize the received power at receiver.

Our goal is to maximize the transmission distance , the point-to-point LoS MIMO channel between the reconfigurable reflectarray and the user can be effectively reduced to a SISO channel where the capacity can be expressed as

$$\Gamma = B \log_2 \left(1 + \frac{|\mathbf{w}_{\mathrm{R}}^* \mathbf{H} \mathbf{w}_{\mathrm{T}}|^2}{\sigma^2}\right) \quad = B \log_2 \left(1 + \frac{P_t |\alpha_r^{(T)}|^2 |\alpha_r^{(R)}|^2 |\mathrm{AF_t AF_r AF_p}|^2}{\sigma^2}\right). \tag{2.16}$$

According to the pattern multiplication rule, the total field pattern is the product of the single element pattern and the array factor. For the single element pattern, an isotropic element is assumed. Hence, the array factor of the reconfigurable reflectarray can be expressed as

$$\mathrm{AF}_p = \sum_{m_x=0}^{M_x-1} \sum_{m_y=0}^{M_y-1} \rho_{\mathrm{m_x,m_y}} \exp\left(-j\varphi_{\mathrm{m_x,m_y}}\right) G_p \exp\left(-jkd\left(m_x \sin\theta\cos\phi + m_y \sin\theta \sin\phi\right)\right), \tag{2.17}$$

where d denotes the element spacing and is assumed to be the same along the x- and y-axis (i.e., $\Delta_x = \Delta_y = d$).

2.4 Performance Evaluation

Based on the received signal in the effective channel in Equation 2.14, we can evaluate the performance of the Intelligent Communication Environments in transmission distance enhancement, or equivalently, the spectral efficiency improvement at a given distance. We

Table 2.2: Parameters in simulations

Symbol	Parameter	Value
N_t	Number of antenna elements at AP	16×16
N_r	Number of antenna elements at UE	8×8
G_{ele}	Gain of individual antenna element	1
B_{sc}	Bandwidth of one sub-band	5 GHz
T	Ambient noise temperature	300 K
d	Antenna element spacing	$\lambda/2$

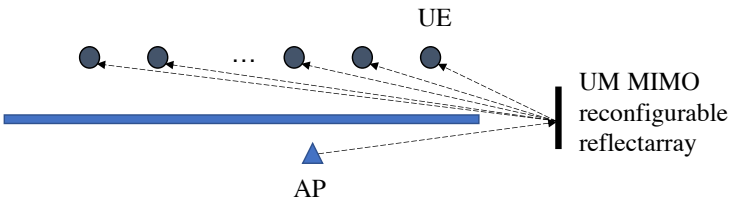

Figure 2.7: Simulation scenario of an intelligent communication environment with a fixed AP and reconfigurable reflectarray, and a UE with gradually increasing distance from the reflectarray.

first consider a scenario where the AP and the reconfigurable reflectarrays are fixed, while the UE can be at locations with distances gradually increase, as shown in Figure 2.7. The simulation parameters are listed in Table 2.2. With the knowledge of transmissible windows in the THz spectrum, we study two frequency bands, which are 300 and 410 GHz, respectively. It is observable that at both simulated frequencies, as the UE moves further away from the reconfigurable reflectarray, the spectral efficiency gradually decreases. However, when the number of elements at the reconfigurable reflectarray increases, we can observe a steady spectral efficiency increase of 2 bits/s/Hz starting at $M = 256$ (as compared to values when $M = 128$ outside the circled area). This result indicates a minimum effective size of the reconfigurable reflectarray to balance the tradeoff between spectral efficiency and energy consumption when larger sizes are used.

One step further, we exploit the possibilities to utilize the UM MIMO design at the

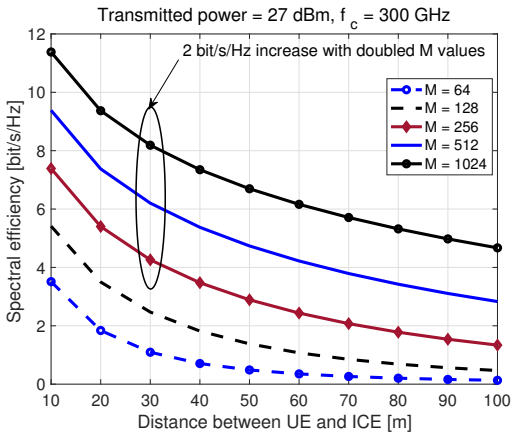

(a) Spectral efficiency at 300 GHz with various distances between the UE and the ICE.

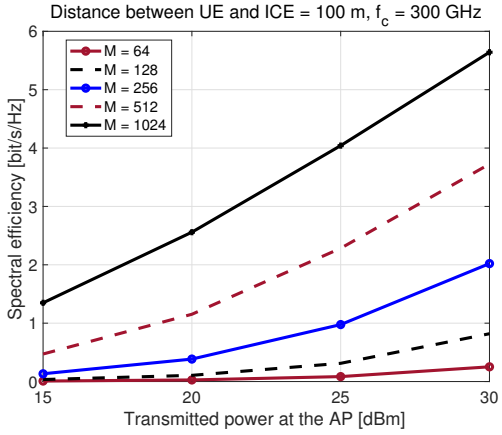

(b) Spectral efficiency with different transmit power levels at the AP at 300 GHz.

Figure 2.8: Simulation results in spectral efficiency improvement at 300 GHz with UEs in NLoS area of the AP.

AP and UE, while coating a real-world environment with the reconfigurable reflectarray and target for maximum distance improvement. The simulation environment is a "E"-shape indoor hallway as shown in Figure 2.10, which resembles the layout of the Van Leer building in School of ECE at Georgia Tech. In particular, an AP is utilized to provide THz links to the UEs along the hallway. When users are blocked by walls, LoS transmissions are obstructed and only paths through reflections can provide viable links. In our simulation environment, the indoor space has a height of $\mathrm{H} = 3\ \mathrm{m}$. All walls, floors, and ceilings are

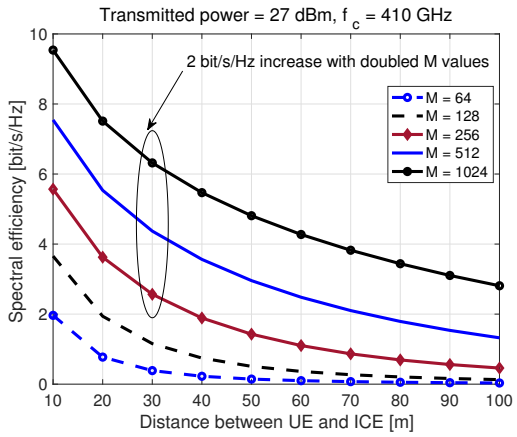

(a) Spectral efficiency at 410 GHz with various distances between the UE and the ICE.

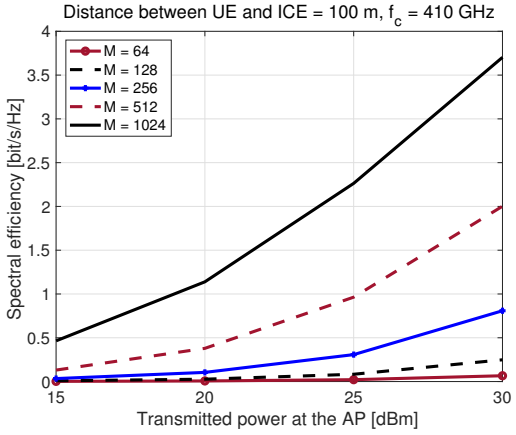

(b) Spectral efficiency with different transmit power levels at the AP at 410 GHz.

Figure 2.9: Simulation results in spectral efficiency improvement at 410 GHz with UEs in NLoS area of the AP.

regarded as planar surfaces comprised of concrete and plywood coverings.

Specifically, as shown in our simulation environment in Figure 2.10, there are in total 15 UE locations including nine in LoS area and six in NLoS areas, as well as one AP location located in the hallway on the ceiling level. The UE locations are chosen in order to compare the same distance in both LoS and NLoS areas. Due to the specific environment layout, some UE with distances less than 40 m and of 70 m cannot be found in NLoS areas. The nine UE in LoS area have the distance of 10 m to 90 m from the AP, while six

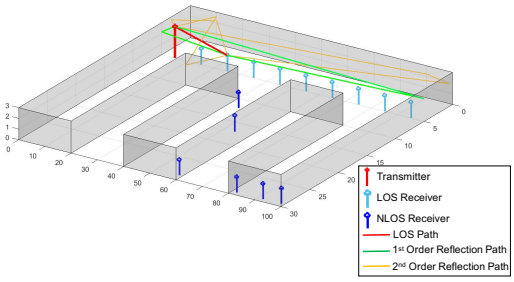

(a) The layout and transceiver locations of the "E" shape simulation environment with ray-tracing results shown for a pair of AP-UE link in the LoS area.

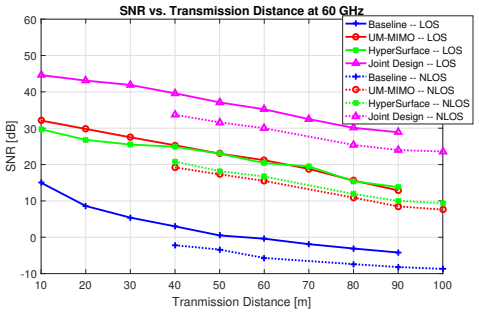

(b) SNR at various distance with different techniques (UM-MIMO, HyperSurface, and the joint design) at center frequencies of 60 GHz.

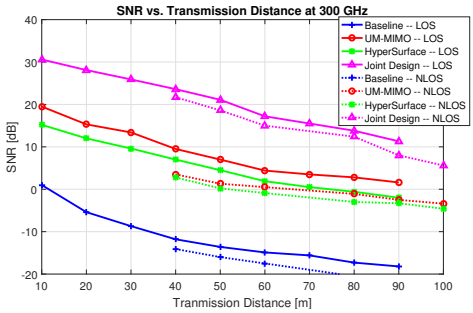

(c) SNR at various distance with different techniques (UM-MIMO, HyperSurface, and the joint design) at center frequencies of 300 GHz.

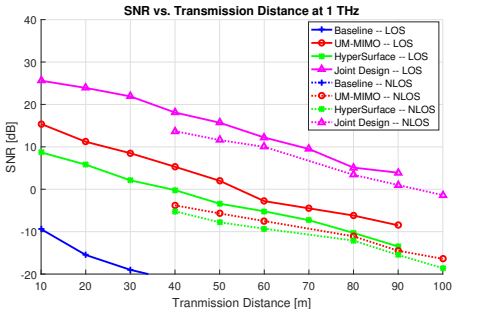

(d) SNR at various distance with different techniques (UM-MIMO, HyperSurface, and the joint design) at center frequencies of 1 THz.

Figure 2.10: Simulation results in an indoor hallway with one AP and 15 UE locations.

UE in NLoS areas have the distance of 40–60 m, and 80–100 m from the AP, all with a spacing of 10 m. The AP is located at $(5\ \mathrm{m}, 5\ \mathrm{m}, 2.95\ \mathrm{m})$ and the UE has a uniform height of $\mathrm{h} = 1.5$ m. We utilize a three-dimensional dynamic ray-tracer developed for mmWave and THz bands, specifically to perform ray tracing from the AP to all UE locations in 3D space, which has been used to support the simulation work in [61]. This map-based ray-tracer is built based on 3D channel models in mmWave and THz frequency bands. With the capability to configure the simulation environment based on real-world scenarios in both indoor and outdoor space, the ray-tracer provides accurate and realistic spatial channel properties with detailed path information on LoS, reflection, diffraction, and scattering paths. In this simulation, we evaluate three distinct frequency bands at 0.06, 0.3, and

1 THz, and the bandwidth is set as 10% of the center frequency in each simulation case. The transmitted signal power is set to be 10 dBm at the AP. In the case of UM MIMO, the gain of antenna arrays is 30 dBi at both AP and UE where in the baseline case, omnidirectional antennas are used at both sides. Without loss of generality, in our simulation, we assume the reflectance values of the walls, floors, and ceilings are 0.75, 0.5, and 0.8, respectively [61]. The noise power spectral density is -160 dBm/Hz [17].

Based on the 3D ray-tracing simulation results at 0.06, 0.3, and 1 THz, we are able to examine the transmission distance improvement in mmWave and THz frequency bands. As shown in Figure 2.10b, the distance to reach a threshold of SNR of 10 dB is around 18 m in the baseline case at 60 GHz in LoS. After applying either the UM MIMO communication technique, reconfigurable reflectarray, or the joint design, the distance to reach the same threshold of SNR is increased to more than 90 m. Even for UE located in NLoS areas, the distance improvement is significant. Similar trend can be observed in both cases at 300 GHz and 1 THz. As shown in Figure 2.10c, at 300 GHz, the SNR threshold of 10 dB cannot be reached without any techniques deployed, while the joint design provide satisfying link up to 85 m for UEs in both LoS and NLoS areas. Moreover, the joint design offers robust transmission until 60 m for both cases even at 1 THz, as shown in Figure 2.10d. The simulation results also show that the distance improvement of these technologies and the joint design is consistent throughout mmWave and THz bands, with the average gains introduced by UM MIMO communication, reconfigurable reflectarray, and the joint design to be approximately 17 dB, 15 dB, and 32 dB, respectively.

2.5 Summary

In this chapter, UM MIMO platforms consisting of reconfigurable antenna arrays, enabled by either graphene or metasurfaces and utilized in transmission, reception, and reflection, have been proposed. An end-to-end analytical physical model has been developed and analyzed to highlight the significant enhancement in both transmission distance and achievable

spectral efficiency. Further, we analyze the distance limitation problem and NLoS issue faced by both mmWave and THz bands caused by atmospheric attenuation and molecular absorption in wireless communication systems. Based on the analyses, simulation results demonstrate a substantial distance improvement in utilizing the proposed Intelligent Communication Environments in simulated real-world communication scenarios.

CHAPTER 3

BEAMFORMING IN INTELLIGENT COMMUNICATION ENVIRONMENTS

3.1 Motivation and Related Work

On the basis of the UM MIMO-based Intelligent Communication Environment design discussed in the previous chapter, the next relevant question is to develop beamforming solutions for the reconfigurable reflectarray in order to maximize throughput for desired users. In this chapter, beamforming solutions are analyzed, as well as a precoding design for the reconfigurable reflectarray that leverages the benefit of polarization diversity in the system.

In reported work on the Programmable Wireless Environments (PWEs) and Intelligent Reflecting Surfaces (IRSs) that aim to transform passive propagation environments into an active component in the wireless transmission, most research efforts have been dedicated to studies at lower frequency bands. However, these solutions might not be directly applicable the mmWave and THz bands, which in fact could be the most suitable candidate for such intelligent surfaces, due to the severe fading effects, which yield a spatially sparse channel [20, 62, 63]. In such spatially sparse channel, only a limited number of multipaths exist to propagate the signals, and the LoS component usually is the dominant one. Thus, in a realistic wireless communication environment where a transmitter and a receiver are not visible to each other and multipaths due to specular reflection suffer from significant attenuation, it is desirable to have the intelligent surfaces perform controlled reflection to improve the link performance.

As discussed in the previous chapter, reconfigurable reflectarrays of the UM MIMO communication platform provide the potential of focusing and steering beams towards various directions. In particular, this design can bring unprecedented path gain for users in NLoS regions of the AP.

It is worth pointing out some fundamental differences among existing intelligent surface solutions, namely, the UM MIMO communication-based intelligent environments, conventional reflectarrays, IRS, and relays with multiple antennas. The efficiency of electronic phase tuning in reflectarrays is highly dependent on the form factor of the arrays as well as the complexity of the environment, which means that in case of reflectarrays with large dimensions or in a scatterer-rich environment, the efficiency might reduce [64]. Similarly, channel estimation at multi-antenna relays becomes unwieldy as current decode-and-forward relays need to perform decoding and encoding before forwarding signal streams. The IRSs, which can realize efficient reconfigurations of antenna elements via a remote controller, currently are designed for microwave bands in the sub-6 GHz, which might not be directly applicable at higher frequency bands such as mm-wave and THz bands due to channel peculiarities such as the frequency selective fading and the aforementioned spatial sparsity.

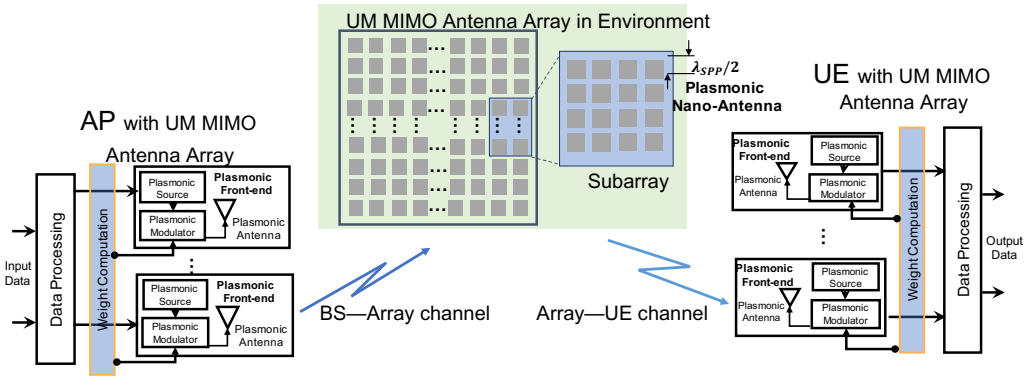

Figure 3.1: Illustration of the UM MIMO channel between an AP (left), the reconfigurable reflectarray (middle) and a UE (right).

Owing to the advantages offered by the UM MIMO communication platform at both the transceiver and in environment, a relevant challenge is the beamforming solution design in order to maximize the targeted UE's signal-to-noise ratio (SNR) in a noise-limited channel. In previous studies, the phase shifts of reconfigurable intelligent surfaces are optimized for the purpose of energy efficiency maximization in a multiple-input-single-output downlink communication system [32], as a part of the holographic MIMO surfaces for the

6G wireless networks [65].

In this chapter, we present two beamforming solutions: one that considers continuous phase shifts and one based on phase-gradient metasurfaces with discrete phase shifts with no RF chains. We also propose a dual-polarized precoding design for diversity.

3.2 System Model

In the environment, similar to the configuration in Chapter 2, we study the UM MIMO channel consisting of an access point (AP) with N_t antennas, a user equipment (UE) with N_r antennas, as well as a reconfigurable reflectarray with M antenna elements in an indoor space. In particular, the reconfigurable reflectarray is based on metasurfaces in mm-wave and graphene for THz bands where demonstrated results in [47] have shown nano-transceivers and nano-antennas with maximum dimension of $\lambda/20$ (with λ being the signal wavelength), allowing them to be densely integrated in very small footprints (e.g., 144 elements in 1 cm^2 at 60 GHz and 1024 elements in 1 mm^2 at 1 THz [2]). As shown in Figure 3.1, at THz band, each element in the array includes an on-chip THz source built with high electron mobility transistor based on III-V semiconductors [66] and a modulator built on graphene-based plasmonic waveguide to modify the propagation speed of the surface plasmon polariton wave [67, 21].

In the indoor environment, we assume the AP and UE are not visible to each other, but both are visible to the reconfigurable reflectarray, as indicated in Figure 3.1. We also assume that the AP has good channel knowledge. With the help of external sensor, the reconfigurable reflectarray can learn the direction of the UE. The channels of the AP–array link and the array–UE link can be denoted as $\mathbf{H}_{\mathrm{T}} \in \mathbb{C}^{M \times N_t}$ and $\mathbf{H}_{\mathrm{R}} \in \mathbb{C}^{N_r \times M}$, respectively.

In the UM MIMO-based intelligent communication environments, the channel contains two parts: one being the channel between the transmitter and the reconfigurable reflectarray, and other other being the reconfigurable reflectarray and receiver. We denote these two channels as $\mathbf{H}_{\mathrm{T}}$ and $\mathbf{H}_{\mathrm{R}}$, respectively. These two channels are connected with a diagonal

tuning matrix of the reconfigurable reflectarray, denoted by $\mathrm{P} = \mathrm{diag}[\rho_1 e^{j\varphi_1}, ..., \rho_M e^{j\varphi_M}]$, which has an amplitude and phase shift on each element. We assume that the reconfigurable reflectarray is visible to both the transmitter and the receiver, while the latter two are not directly visible; however, there exist possible multipaths stemmed from specular reflections off natural materials.

Based on the channel shown in Figure 3.1, the received signal can be expressed as

$$\begin{aligned} y &= \mathbf{w}_{\mathrm{R}}^{*} \mathbf{H} \mathbf{w}_{\mathrm{T}} x + n \\ &= \mathbf{w}_{\mathrm{R}}^{*} \left(\mathbf{H}_{\mathrm{R}} \mathrm{P} \mathbf{H}_{\mathrm{T}} \right) \mathbf{w}_{\mathrm{T}} x + n, \end{aligned} \tag{3.1}$$

where x is the transmitted signal with $\mathbb{E}[|x|^2] = P_t$ where P_t is the transmit power, $\mathbf{w}_{\mathrm{R}}$ is the beamforming vector at the UE with $|w_{\mathrm{R}}[i]| = \frac{1}{\sqrt{N_r}}$, $i = 1, ..., N_r$, and $\mathbf{w}_{\mathrm{T}}$ is the beamforming vector at the AP with $|w_{\mathrm{T}}[i]| = \frac{1}{\sqrt{N_t}}$, $i = 1, ..., N_t$, and $n \sim \mathcal{N}_c(0, \sigma^2)$ is the additive white Gaussian noise at the UE side.

3.3 Optimal Beamforming at Reconfigurable Reflectarray

As shown in the previous chapter, the controlled reflection off reconfigurable reflectarray can add significant gain to the received signal compared to the natural reflection off natural materials, the beamforming vectors at the AP and UE will aim to steer the beams towards the direction of the reconfigurable reflectarray in order to maximize the array gain to mitigate the high path loss. Specifically, we can elaborate the channels $\mathbf{H}_{\mathrm{T}}$ and $\mathbf{H}_{\mathrm{R}}$ as

$$\mathbf{H}_{\mathrm{T}} = \sqrt{N_t M} \alpha_r^{(T)} \mathbf{a}_{\mathrm{P}} \left(M, \theta_a, \phi_a \right) \mathbf{a}_{\mathrm{T}}^{*} \left(N_t, \theta_t, \phi_t \right), \tag{3.2a}$$

$$\mathbf{H}_{\mathrm{R}} = \sqrt{N_r M} \alpha_r^{(R)} \mathbf{a}_{\mathrm{R}} \left(N_r, \theta_r, \phi_r \right) \mathbf{a}_{\mathrm{P}}^{*} \left(M, \theta_{ar}, \phi_{ar} \right), \tag{3.2b}$$

where θ and ϕ denote the angles in elevation and azimuth planes, respectively, with subscripts r, ar, a, and t representing the receiving, anomalous reflected, arriving, and transmitting angles, respectively, $\mathbf{a}_{\mathrm{T}}$, $\mathbf{a}_{\mathrm{R}}$, and $\mathbf{a}_{\mathrm{P}}$ denote the array steering vectors of the AP, the

UE, and the reconfigurable reflectarray, respectively, which can be expressed as (here we use $\mathbf{a}_{\mathrm{P}}$ as an example)

$$\mathbf{a}_{\mathrm{P}} = \begin{bmatrix} 1 & \dots & e^{(jkm_x\Delta_x \sin\theta\cos\phi + jkm_y\Delta_y \sin\theta\sin\phi)} & \dots & e^{(jk(M_x-1)\Delta_x \sin\theta\cos\phi + jk(M_y-1)\Delta_y \sin\theta\sin\phi)} \end{bmatrix}^{\mathsf{T}}, \tag{3.3}$$

where $M = M_x M_y$, with M_x and M_y denoting the number of plasmonic antenna elements along the x- and y-axis, respectively.

3.3.1 Beamforming at the AP and UE

Since the AP and the UE also operate in mm-wave and THz bands, where large antenna arrays are necessary to mitigate the high path loss and atmospheric attenuation. Under the assumptions of large planar arrays and a single-stream transmission, the optimal singular value decomposition-based beamforming vectors at both the AP and the UE are proven to converge to array steering vectors corresponding to the dominant path direction [68], which can be expressed as

$$\mathbf{w}_{\mathrm{T}}^{\star} = \mathbf{a}_{\mathrm{T}}\left(N_t, \theta_{\mathrm{T}}^{(0)}, \phi_{\mathrm{T}}^{(0)}\right), \tag{3.4a}$$

$$\mathbf{w}_{\mathrm{R}}^{\star} = \mathbf{a}_{\mathrm{R}}\left(N_r, \theta_{\mathrm{R}}^{(0)}, \phi_{\mathrm{R}}^{(0)}\right), \tag{3.4b}$$

where $\theta_{\mathrm{T}}^{(0)}$ and $\phi_{\mathrm{T}}^{(0)}$ are the elevation and azimuth angles of the dominant path connecting the AP and the reconfigurable reflectarray (i.e., the LoS path), and $\theta_{\mathrm{R}}^{(0)}$ and $\phi_{\mathrm{R}}^{(0)}$ are the elevation and azimuth angles of the dominant path connecting the UE and the reconfigurable reflectarray, respectively.

3.3.2 Beam-steering at the reconfigurable reflectarray

With the optimal beamforming solutions obtained at the AP and the UE, the remaining task is the beamforming design at the reconfigurable reflectarray. For a desired direction to

which the main beam is expected to be steered of the reconfigurable reflectarray, denoted as $\left(\bar{\theta}, \bar{\phi}\right)$ [69],

$$\begin{aligned} \mathrm{AF_P}\left(\bar{\theta}, \bar{\phi}\right) = & \frac{\sin\left(\frac{M_x k \Delta_x}{2}\left(\sin\theta\cos\phi - \sin\bar{\theta}\cos\bar{\phi}\right)\right)}{\sin\left(\frac{k\Delta_x}{2}\left(\sin\theta\cos\phi - \sin\bar{\theta}\cos\bar{\phi}\right)\right)} \\ & \times \frac{\sin\left(\frac{M_y k \Delta_y}{2}\left(\sin\theta\sin\phi - \sin\bar{\theta}\sin\bar{\phi}\right)\right)}{\sin\left(\frac{k\Delta_y}{2}\left(\sin\theta\sin\phi - \sin\bar{\theta}\sin\bar{\phi}\right)\right)}, \end{aligned} \tag{3.5}$$

where the progress phase shifts along the x- and y-axis are $-k\Delta_x \sin\bar{\theta}\cos\bar{\phi}$ and $-k\Delta_y \sin\bar{\theta}\sin\bar{\phi}$, respectively. The phase response of the (m_x, m_y)-th element is

$$\varphi_{m_x,m_y} = -k\left(\Delta_x \sin\bar{\theta}\cos\bar{\phi} + \Delta_y \sin\bar{\theta}\sin\bar{\phi}\right),$$

where $k = 2\pi/\lambda$ is the wave number. We assume the amplitude excitation is uniformly assigned to be $\rho_{m_x,m_y} = 1$. In particular, when the antenna element spacing along the x- and y-axis is the same, which means $\Delta_x = \Delta_y = \lambda/2$ in order to avoid grating lobes and minimize mutual coupling effect, the phase shift matrix of the reconfigurable reflectarray is then

$$\mathrm{P} = \mathrm{diag}\left[1, ..., e^{-j\pi(m_x \sin\bar{\theta}\cos\bar{\phi} + m_y \sin\bar{\theta}\sin\bar{\phi})}, ..., e^{-j\pi\left((M_x-1)\sin\bar{\theta}\cos\bar{\phi} + (M_y-1)\sin\bar{\theta}\sin\bar{\phi}\right)}\right].$$

With the help of a sensing device at the reconfigurable reflectarray feeding the desired direction of the beam (e.g., the direction of the UE to be served), the maximum signal strength can be thus achieved.

3.3.3 Beamforming with phase-gradient metasurfaces

In the previous section, we assume that the phase shifts can take continuous values, which implicitly presume that they have an infinite resolution. However, on the one hand, in practical digital phase shifter designs, such assumption might not be realizable. On the

other hand, the metasurfaces do not necessarily need continuous phase shifts to perform controlled reflection. Researchers have demonstrated that the generalized Snell's law with non-specular reflection or refraction can be achieved with a constant phase gradient across the metasurface [70, 71]

$$\cos\theta_r \sin\phi_r = \frac{1}{kn_i}\frac{d\Phi}{dx}, \tag{3.6a}$$

$$\sin\theta_r - \sin\theta_i = \frac{1}{kn_i}\frac{d\Phi}{dy}, \tag{3.6b}$$

where n_i is the refractive index of the medium containing both the incident and reflected beams ($n_i = 1$ in free space), θ_i and ϕ_i are incident angles in the elevation and azimuth planes, θ_r and ϕ_r are reflected angles in the elevation and azimuth planes, according to [71], defined slightly different from that in Figure 2.6 for the convenience of angle computation. The radiation pattern in far field can be expressed as

$$F(\theta,\phi) = \sum_{m=1}^{M} e^{jk\Gamma_x(m-1)\sin\theta\cos\phi+\mathrm{P}_x(m)} \sum_{n=1}^{N} e^{jk\Gamma_y(n-1)\sin\theta\sin\phi+\mathrm{P}_y(n)}, \tag{3.7}$$

where P_x and P_y are the phase shift vectors of elements along the x- and y-axis, respectively. The adjacent elements has a phase difference equal to the constant phase gradient in Equation 3.6a and Equation 3.6b according to the desired angle of reflection.

3.4 Beamforming in Dual-Polarized Channel

In previous sections, we have analyzed beamforming and beam-steering solutions under an implicit assumption of a channel with a single polarization state. Most existing work has also adopted the same underlying assumption regarding polarization but focuses on maximizing other parameters, including throughput and energy efficiency. A sum rate maximization approach is adopted in [72] under a hybrid beamforming scheme with the practical consideration of limited discrete phase shifts. A joint active and passive beam-

forming scheme is proposed in [73] for energy efficiency optimization and radio frequency (RF) chain reduction.

Distinct from existing designs which employ passive patch elements to realize controlled reflection through discrete phase shifts [74], recent designs based on advanced materials, such as metasurfaces [29, 39] with individual element size much smaller than the signal wavelength, can provide more diverse functionalities to manipulate EM waves, especially at mm-wave and THz bands. Specifically, these advanced materials allow polarization modulation [75, 76], a scheme where the advanced materials reflects or emits EM waves with a different polarization state compared to that of the impinging one. Such unique electromagnetic characteristic lays the theoretical foundation for our proposed polarization diversity scheme in UM MIMO communication. In this section, we focus on a precoding design for the dual-polarized UM MIMO-based Intelligent Communication Environments and study performance improvement in spectral efficiency and diversity gain.

3.4.1 Dual-polarized UM MIMO Antenna Array

The polarization state in an electric field is commonly expressed using the Jones vector in optics, which can also be applied to EM field and expressed as

$$\mathbf{E} = \begin{pmatrix} E_{x0} \exp\left(j\varphi_x\right) \\ E_{y0} \exp\left(j\varphi_y\right) \end{pmatrix},$$

where E_{x0} and E_{y0} denote the amplitude of the electric field along the x- and y-axis, φ_x and φ_y denote the phase of the electric field along the two axes, respectively. This expression implies the EM wave propagating along the z-axis. When the EM wave is horizontally polarized (along the x-axis), the Jones vector becomes $[1\ 0]^\intercal$ with a normalized amplitude, and $[0\ 1]^\intercal$ when the EM wave is vertically polarized (along the y-axis). Usually when the propagation medium is free of interacting objects, the polarization state will be preserved along propagation. However, such ideal case is extremely rare in realistic wireless com-

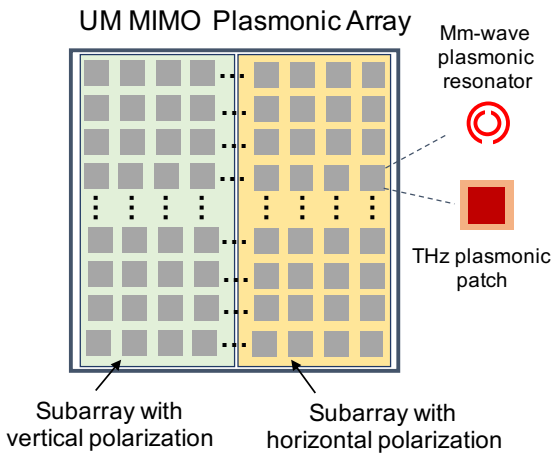

Figure 3.2: Illustration of an array with two subarrays with two polarization states shown in different colors.

munication environments, where objects in the vicinity of transceivers or transverse EM waves can influence the propagation. Resultant effects include lossy reflections, scattering towards different directions, and polarization state change, or depolarization. When antenna arrays at both transceiver ends share the same single polarization configuration, depolarized EM waves cannot be captured, resulting in energy loss. Therefore, equipping antennas with different polarization states can effectively mitigate such issue.

In the design of UM MIMO plasmonic antenna arrays, one of the appealing features is their capability to control EM wavefront, which includes a polarization state alteration [59]. Additionally, as shown in Figure 3.2, unlike the commonly deployed 2D cross-polarized array with fixed polarization states [77], it is also feasible to dynamically reconfigure the polarization for each element in the plasmonic antenna array in order to further boost polarization diversity when depolarization is not balanced or a particular polarization can be strengthened in practical environments.

In this section, we assume all EM waves have two mostly commonly seen linear polarization states, which are vertical and horizontal polarization states. Depolarization along propagation occurs between these two states often leads to a cross-polarization ratio, which is an energy loss in the process. The system model in the following subsection characterizes

such loss in the channel. As such, a polarization diversity can be utilized in the UM MIMO communications when transmitting the same signal stream under two orthogonal polarization states. However, in order to achieve satisfying spectral efficiency under the constraint of power consumption while utilizing the polarization diversity, a well-orchestrated precoding design that maximizes the mutual information between both ends of a link becomes a relevant problem.

3.4.2 Channel model under dual polarization

Suppose the UM MIMO plasmonic antenna array-coated environment illustrated in Figure 3.1 sharing the same configuration parameters in previous sections. There is no direct path between the AP and UE, but all are visible to the antenna array in the environment. Different from the previous sections in this chapter, we focus on the channel between the antenna array in the environment and the UE with dual linear polarization states, shown as the *Array–UE channel* in Figure 3.1. In particular, within each plasmonic front-end, there exists a plasmonic source and modulator to control the phase shift and amplitude of the plasmonic antenna [57].

In realistic propagation environments, the LoS path usually preserves its polarization state while scattered multipaths can be depolarized. Hence, the channel matrix between the antenna array in the environment and the UE, denoted as $\mathbf{H}_{\mathrm{R}}$ in Equation 3.2, can be written as the sum of the channel consisting of the LoS path $\mathbf{H}_{\mathrm{LoS}}$ and all multipath components (MPCs) from reflection and scattering $\mathbf{H}_{\mathrm{NLoS}}$,

$$\mathbf{H}_{\mathrm{R}} = \sqrt{\frac{\kappa}{1+\kappa}}\mathbf{H}_{\mathrm{LoS}} + \sqrt{\frac{1}{1+\kappa}}\mathbf{H}_{\mathrm{NLoS}}, \tag{3.8}$$

where κ is the Rician K-factor, which is the ratio between the power of the direct path and the sum of power from all MPCs. Previous studies have shown that in mm-wave and THz channels, the LoS path dominates the total received power, yielding a high κ with

a maximum observed value of around 19 dB in an indoor environment at 60 GHz [78]. Similar results are also reported in ray-tracing simulations in THz bands [79]. Such high Rician K-factor would lead to a very high singular value spread in the channel matrix, which is not favorable in realizing spatial diversity or multiplexing in traditional massive MIMO communication paradigm. In order to compensate very high path loss in the mm-wave and THz bands, beamforming solutions are usually adopted at both ends of the link with adjusted phase shifts to yield satisfying beamforming gain.

One step further, each component in Equation 3.8 can be further expressed in a dual-polarized format, in order to reflect possible alternation between the two linear polarization states and the polarization diversity from dual-polarized antenna arrays[1],

$$\mathbf{H}_{\text{LoS}} = \begin{bmatrix} \mathrm{H}^{\text{VV}} & \mathbf{0} \\ \mathbf{0} & \mathrm{H}^{\text{HH}} \end{bmatrix}, \mathbf{H}_{\text{NLoS}} = \begin{bmatrix} \mathrm{H}^{\text{VV}} & \mathrm{H}^{\text{VH}} \\ \mathrm{H}^{\text{HV}} & \mathrm{H}^{\text{HH}} \end{bmatrix}, \tag{3.9}$$

where the superscripts (VV, VH, HV, and HH) represent four possible polarization combinations of the paths, in which VV and HH preserve the polarization states, while VH and HV describe the depolarized states. Suppose among all M and N_r antenna elements at the array and UE side, the two linear polarization state are equally distributed, which means each polarization state takes $M/2$ and $N_r/2$ elements at each end, respectively. Using antenna array manifold concept, each entry in Equation 3.9 can be elaborated as

$$\mathbf{H}^{\text{VV}} = \Xi \sum_{l=0}^{L} \alpha_l \mathbf{a}_{\text{R}} \left(\theta_{\text{D},l}, \phi_{\text{D},l}\right) \mathbf{a}_{\text{P}}^{*} \left(\theta_{\text{A},l}, \phi_{\text{A},l}\right), \tag{3.10a}$$

$$\mathbf{H}^{\text{VH}} = \Xi \sum_{l=1}^{L} \frac{\alpha_l}{\sqrt{\gamma_l}} \mathbf{a}_{\text{R}} \left(\theta_{\text{D},l}, \phi_{\text{D},l}\right) \mathbf{a}_{\text{P}}^{*} \left(\theta_{\text{A},l}, \phi_{\text{A},l}\right), \tag{3.10b}$$

where $\Xi = \sqrt{\frac{N_r M}{4L}}$, L is the total number of resolvable paths in the environment (in co-polarized channel the total path is L+1 with the LoS path as indicated in Equation 3.10a), α_l

[1]The subscript R is ignored in later expressions of channel matrices, as this section focuses on the channel $\mathbf{H}_{\text{R}}$.

is the complex path gain of the l-th path, γ_l denotes the aforementioned energy loss (i.e., the cross-polarization ratio, or XPR) in depolarization of the l-th path. The XPR value usually varies per path along propagation. $\mathbf{a}_{\mathrm{R}}$ and $\mathbf{a}_{\mathrm{P}}$ denote the antenna arrays' responses with respect to the l-th path at UE and antenna array, respectively, and * denotes the Hermitian transpose.

3.4.3 Precoding codeword design

In order to design the precoding vector for the dual-polarized channel, the optimization problem is formulated in order to maximize the mutual information in the antenna array to UE channel, which is expressed as

$$\mathcal{I} = \log_2 \det \left(\mathbf{I} + \frac{p}{\sigma^2} \mathbf{H} \mathbf{w}_{\mathrm{a}} \mathbf{w}_{\mathrm{a}}^* \mathbf{H}^* \right). \tag{3.11}$$

As discussed in subsection 3.4.2, in mm-wave and THz bands, the LoS path contains most power and the channel is sparse with limited multipaths [63]. In order to compensate for the high path in these frequency bands, the goal is to optimize the precoding matrix to maximize the beamforming gain in the LoS direction. We can therefore approximate the effective channel as

$$\tilde{\mathbf{H}} = \bar{\alpha} \sqrt{\frac{\kappa N_d N_a}{4(1+\kappa)}} \begin{bmatrix} 1 & \frac{1}{\sqrt{\gamma\kappa}} \\ \frac{1}{\sqrt{\gamma\kappa}} & 1 \end{bmatrix} \otimes \mathbf{a}_{\mathrm{D}} \left(\bar{\theta}_{\mathrm{D}}, \bar{\phi}_{\mathrm{D}} \right) \mathbf{a}_{\mathrm{A}}^* \left(\bar{\theta}_{\mathrm{A}}, \bar{\phi}_{\mathrm{A}} \right), \tag{3.12}$$

where $\bar{\theta}_{\mathrm{D}}$ and $\bar{\phi}_{\mathrm{D}}$ denote the angles of departure in both elevation and azimuth planes, while $\bar{\theta}_{\mathrm{A}}$ and $\bar{\phi}_{\mathrm{A}}$ denote the arrival angles, $\bar{\alpha}$ denotes the LoS path gain. The channel gain with a coefficient of $\frac{1}{\sqrt{\gamma\kappa}}$ further attenuates the cross-polarized channel, which can be approximated as $\frac{1}{\sqrt{\gamma\kappa}} \approx 0$. We can then regard this effective channel as two independent channels with V-V and H-H polarization. The precoding design can then be conducted based on each polarization combination state. In the V-V channel where the channel matrix

is

$$\tilde{\mathbf{H}}_{\mathrm{V}} = \bar{\alpha}\sqrt{\frac{\kappa N_d N_a}{4(1+\kappa)}}\mathbf{a}_{\mathrm{D}}\left(\bar{\theta}_{\mathrm{D}}, \bar{\phi}_{\mathrm{D}}\right)\mathbf{a}_{\mathrm{A}}^{*}\left(\bar{\theta}_{\mathrm{A}}, \bar{\phi}_{\mathrm{A}}\right), \tag{3.13}$$

we can perform the singular value decomposition as $\tilde{\mathbf{H}}_{\mathrm{V}} = \mathbf{U}_{\mathrm{V}}\mathbf{S}_{\mathrm{V}}\mathbf{V}_{\mathrm{V}}^{*}$ to find the optimal precoder without restriction as $\mathbf{w}^{\mathrm{opt}} = \mathbf{V}_{\mathrm{V},1}$ where $\mathbf{V}_{\mathrm{V},1}$ is the first column of $\mathbf{V}_{\mathrm{V}}$ [63]. Our goal of constructing a codeword is to minimize the distance between the designed codeword and the optimal one, which can be expressed as

$$\mathbf{w}_{\mathrm{a}}^{*} = \underset{\mathbf{w}_{\mathrm{a}} \in \mathbf{W}}{\arg\min} ||\mathbf{w}^{\mathrm{opt}} - \mathbf{w}_{\mathrm{a}}||_F^2, \tag{3.14}$$

under a constraint of $\|\mathbf{w}_{\mathrm{a}}\|^2 \leq P_{\max}$ per data stream transmitted. In the plasmonic array, the control over the amplitude m_i and phase v_i of the i-th element of the plasmonic array is coupled by varying the Fermi energy level of the modulator within each front-end [57]. Hence, $\mathbf{w}_{\mathrm{a}}$ is further expressed as $\mathbf{w}_{\mathrm{a}} = \mathbf{m}_{\mathrm{a}} \circ \mathbf{v}_{\mathrm{a}}$ where $\circ$ denotes the Hadamard product. Hence, in order to solve for the desired codeword, an iterative approach based on orthogonal matching pursuit (OMP) is deployed. The codebook is constructed based on a set of codewords pointing towards different LoS directions with maximal spectral efficiency. It is clear that the size of the channel matrix sets a prohibitively high cost in performing exhaustive search per antenna array element. Therefore, based on the scarcity of mm-wave and THz channels, we can group multiple antenna elements according to their polarization states into subarrays and steer these subarray beams towards LoS paths in the channel.

3.5 Performance Evaluation

Based on the proposed beamforming schemes, we evaluate the overall performance of the UM MIMO-based intelligent communication environment in a channel with ten paths (including the LoS path). A user is located in a direction with an angle of 30° from the broadside of the reconfigurable reflectarray fixed in the environment. In the beamforming design with a single polarization state, we assume that the reconfigurable reflectarray is

Table 3.1: Simulation parameters

Parameter	Value
Number of paths in channel	10
Number of elements at reconfigurable reflectarray/plasmonic array	200
Total number of antenna elements at UE	128
Rician K-factor	15 dB

equipped with 256 antennas elements. In order to maintain a square-shaped subarray with each polarization state, in the dual-polarization beamforming study, the reconfigurable reflectarray has a size of 200 antennas. The rest of the simulation parameters are shown in Table 3.1.

The main beam in the reconfigurable reflectarray can be steered towards different different pointing at the UE. As shown in Figure 3.3, with continuous phase shift assumed, the main beam of the reconfigurable reflectarray can be steered with a predefined angle (shown in examples as $\theta = 30^\circ$ and $\theta = 45^\circ$) with a constant maximum array gain. The phase-gradient metasurface is assumed to have a phase gradient of 90°, which means it allows four phase shifts in each element, $0^\circ, 90^\circ, 180^\circ$, and 270°, as shown in four colors in Figure 3.4a and Figure 3.4c. In particular, Figure 3.4a demonstrates a column-wise phase shifting pattern, which yields an array pattern with a steered main beam towards $\theta = 30^\circ$. In Figure 3.4c, an element-wise phase shift pattern is adopted based on the calculation in subsection 3.3.3 to yield a main beam towards $\theta = 45^\circ$. Note that an isotropic element is assumed in simulation, which results in the relatively side lobes near 90°. Such strong side lobes will diminish when a practical element design is used. We also note that in the element-wise phase shift pattern, in addition to the main direction, we could also utilize other strong beam directions to serve users in other directions. For instance, $\theta = 15^\circ$ demonstrates a beam where another user can also receive the reflected signal. Based on the pattern iteration, these side beams can be enhanced or suppressed.

In the dual-polarized channel, based on the proposed codebook design, we can evaluate the overall performance of the UM MIMO plasmonic array analytically in a 3D channel

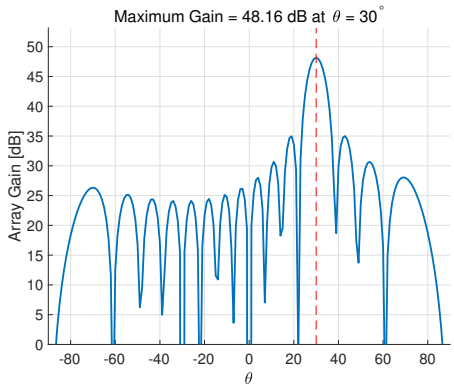

(a) A planar reflectarray with a steered angle of 30°.

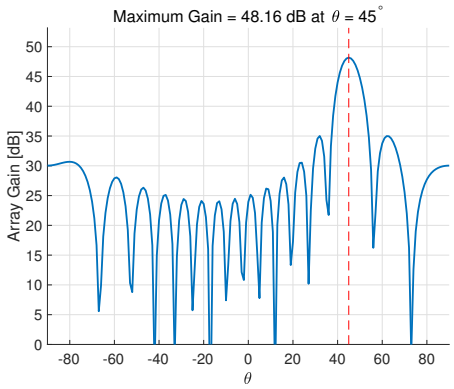

(b) A planar reflectarray with a steered angle of 40°.

Figure 3.3: Beam-steered pattern of a 16 × 16 planar reflectarray at 300 GHz.

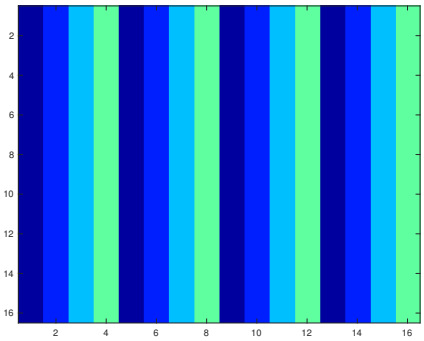

(a) A 16 × 16 phase-gradient metasurface with a phase gradient of 90° following a column-wise phase-shifting pattern.

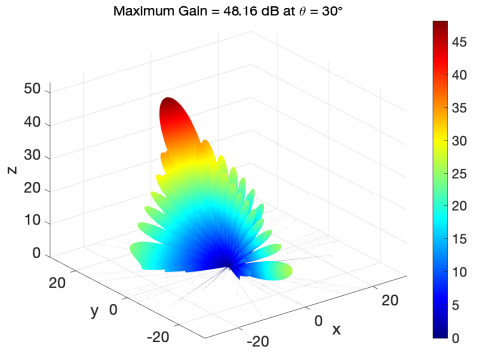

(b) Far-field scattering pattern of the phase-gradient metasurfaces at 300 GHz with a steered direction of reflection at $\theta = 30°$.

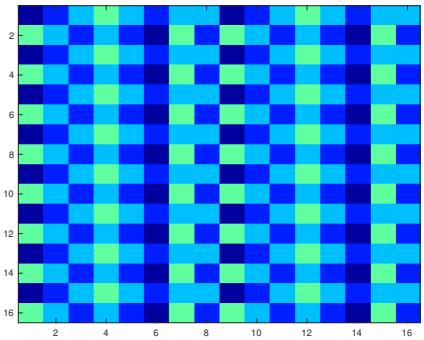

(c) A 16 × 16 phase-gradient metasurface with a phase gradient of 90° following a column-wise pattern.

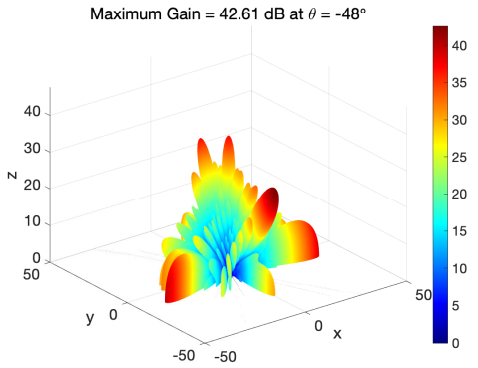

(d) Far-field scattering pattern of the phase-gradient metasurfaces at 300 GHz with a steered direction of reflection at $\theta = 45°$.

Figure 3.4: Controlled reflection with a phase-gradient metasurface using different phase shift patterns.

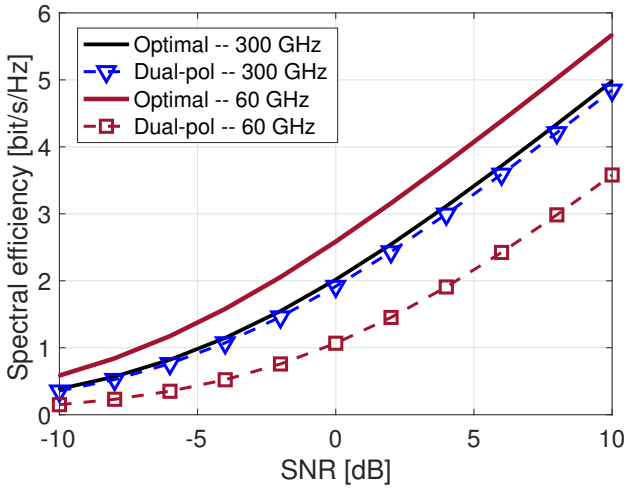

Figure 3.5: Achieved spectral efficiency at 60 and 300 GHz with optimal precoding and dual-polarization codebook.

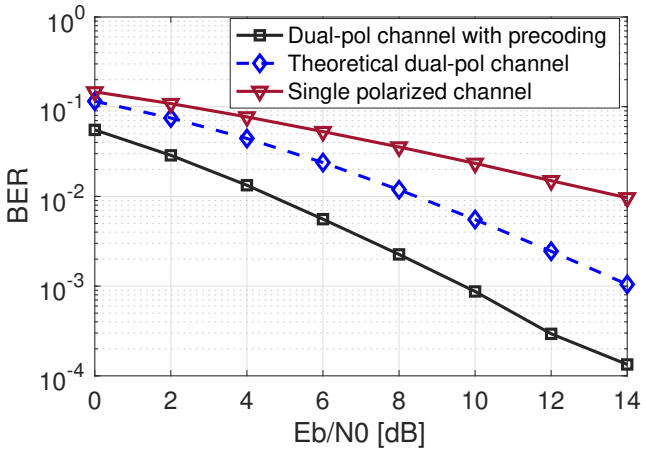

Figure 3.6: Bit error rate performance at 300 GHz with single and dual-polarization codebook design.

at 60 and 300 GHz and compare with the optimal case. In order to compute the spectral efficiency, we assume that good channel knowledge is known at the UE side so it can perform optimal combining. The metric of evaluation adopted in this simulation is the link spectral efficiency, which is computed based on a wide SNR range in mmWave and THz band channel. We assume the distance between the plasmonic antenna array and the UE is greater than the Fraunhofer distance, where plane waves travel between the devices. The depolarization loss is modeled as a function of the path's excess loss, which is the residual

of total loss after subtracting the free-space path loss [80].

As shown in Figure 3.5, the dual-polarized codebook-based link demonstrates near-optimal spectral efficiency at 300 GHz. This is due to the relatively strong LoS path power being further strengthened. We also draw a comparison with respect to the case when perfect channel knowledge is available for the UM MIMO surface array. The Rician K-factor is assumed to be 15 dB in the simulation. For each case, the simulation is run 1000 times and the resultant throughput is averaged. We also study the link performance under the QPSK modulation to analyze the polarization diversity in channel. As shown in Figure 3.6, a polarization diversity gain around 4 dB is obtained from the dual-polarized channel at a bit error rate of 10^{-3} compared to the theoretical dual-polarized channel.

3.6 Summary

In this chapter, we present beamforming and beam-steering designs to achieve high spectral efficiency at mmWave and THz-band frequencies in order to enhance the communication distance. Two beamforming schemes based on optimal continuous phase shifts with reconfigurable reflectarray and a phase-gradient metasurfaces are discussed. In addition, a dual-polarization channel model based on UM MIMO plasmonic array is proposed and analyzed under an array-of-subarray architecture. Owing to the feature of reconfigurable electromagnetic characteristic of advanced artificial 2D materials such as metasurfaces, dynamic polarization states can be achieved and utilized to realize polarization diversity in wireless channels. A precoding design based on optimizing the dominant paths' strengths is proposed and analyzed. Simulation results are obtained to verify such polarization diversity gain.

CHAPTER 4
PATH TRACKING IN A THREE-DIMENSIONAL TERAHERTZ BAND CHANNEL

4.1 Motivation and Related Work

As mentioned in previous chapters, the THz band is deemed as a promising enabling solution for satisfying the ever-increasing requirements on data rates, end-to-end latency, and end-user experience [81]. In order to utilize the THz band with its full potential, a good understanding of the characteristics becomes the priority for channel modeling and system design on the physical layer. In indoor environments, the most common communication scenario is the local area network (LAN), which requires the APs to provide satisfying connections to the UE. However, in mmWave and THz bands, the indoor channel is observed as non-stationary, since both the UE and random objects can be moving [82]. Therefore, the conventional assumption of channel stationarity or quasi-stationarity is no longer valid for THz band communication. Additionally, the channel capacity is influenced by the molecular composition of the propagation medium and propagation distance [17], so a comprehensive three-dimensional (3D) channel model is required to describe the THz band.

Several research efforts have been dedicated to the THz channel modeling. One of the earliest channel models in the THz band analyzes the important channel parameters and emphasizes the molecular absorption effect and channel capacity as a function of propagation distance [17]. Furthermore, a multi-ray-based channel model provides a detailed analysis on distance-varying and frequency-selective characteristics in THz band [61]. A 3D end-to-end channel model based on graphene antenna provides a feasible approach for realizing ultra-high-speed THz communication links [83]. The work in [84] analyzes the reflectivity properties of various building materials and the scattering effect in indoor en-

vironments based on Kirchhoff theory of scattering. A channel model for small particle scattering effect has been developed for nanonetworks in THz band in both frequency and time domains [85]. Moreover, several measurements have been reported at 0.3 THz with various antenna types and transceiver locations [86]. These models are mostly based on a static link which assumes both ends do not change locations along time variation.

In this chapter, we start with describing the THz band in both time and frequency domains by the channel impulse response, transfer function, as well as other important channel parameters for line-of-sight (LoS) path and multipaths, respectively. We then propose to use the continuous-time Markov chain (CTMC) to depict the evolution of multipaths while develop an accurate channel tracking algorithm based on the extended Kalman filtering (EKF) approach for the LoS path, which is considered the most significant path in the THz channel. In order to deploy such tracking algorithm in real system design, we also study the channel model with ray-tracing simulation and demonstrate the capacity performance in a real-world environment.

4.2 3D Time-Varying Channel Model in THz Band

In this section, we start by describing the general channel behavior from both time and frequency domains. Then we separately discuss the LoS path and multipaths. We assume that the transmitter (Tx) is fixed at a ceiling level in order to emulate the LAN setting. The receiver (Rx) is assumed to have arbitrary moving velocities. The initial locations of both Tx and Rx are known. The trajectory of Rx along time can be assumed as $\nu(t) \in \mathbb{R}^3$. The full list of parameters used in this work can be found in Table Table 4.1.

4.2.1 Time-varying THz channel in time and frequency domains

The channel impulse response in a time-varying channel can be expressed as a function of delay τ, Doppler frequency f_d, and angular parameters ϕ and θ in the following form,

$$\begin{aligned} h(t,\tau,f_d,\phi,\theta) = & \\ & \sum_{i=1}^{I(t)} \alpha_i(t) e^{j f_d(t)(t-\tau_i(t)) - 2\pi f_c \tau_i(t)} \\ & \cdot \delta(\tau - \tau_i(t)) \delta(\phi - \phi_i(t)) \delta(\theta - \theta_i(t)), \end{aligned} \tag{4.1}$$

in which $\delta(\cdot)$ is the Dirac delta function, $I(t)$ denotes the total number of multipath components (MPCs) at time t, α_i the fading process, τ_i the delay of the path, ϕ_i the azimuth angle of arrival, and θ_i the elevation angle of arrival, all of which are for the i-th MPC at time t. In the frequency domain, the end-to-end multipath-wise channel transfer function should also include the Fresnel reflection coefficient for the transverse magnetic (TM) polarized waves, the Rayleigh factor for surface roughness, and the scattering coefficient according to the modified Beckman-Kirchhoff theory [83]. Additionally, the molecular absorption effect should also be considered in the THz channel [17]. Therefore, we have the following complex channel transfer function for the i-th MPC at time t,

$$H_i(t,f) = \left| \frac{g_c(f,t)}{\sqrt{4\pi d(t)^2}} e^{-\frac{1}{2} k_{ma}(f) d(t)} \right| e^{-j2\pi f \tau_i(t)}, \tag{4.2}$$

$$d(t) = \int_t^{t+\Delta t} |\mathbf{v}(t)| dt, \tag{4.3}$$

$$g_c(f,t) = \begin{cases} 1, & \text{LoS paths,} \\ \gamma_{TM}(f) \cdot \rho(f,t), & \text{Reflected paths,} \\ S(f,t), & \text{Scattered paths.} \end{cases} \tag{4.4}$$

Table 4.1: Parameters in the 3D Time-Varying THz Channel Model

Parameter Notation	**Description**
$\mathbf{v}(t)$	Velocities of the Rx
$\nu(t)$	Moving trajectory of Rx
$d(t)$	Distance between the Tx and Rx in 3D space
Δf	Bandwidth of channel
$f_d(t)$	Doppler frequency of channel
t_{coh}	Coherence time of channel
$\tau^{(i)}, \phi^{(i)}, \theta^{(i)}$	Parameter set for the i-th MPC
P_{Tx}	Transmitted power from Tx antenna
G_{Tx}	Antenna gain at the Tx side
σ^2	Square error of Kalman filtering

where $d(t)$ is a time-varying propagation distance between Tx and Rx, $k_{ma}(f)$ denotes the frequency-dependent medium absorption coefficient, $\mathbf{v}(t)$ is the velocity of Rx, $g_c(f,t)$ is the frequency and time dependent loss function at the surface of incidence, $S(f,t)$ is the scattering coefficient of rough surfaces based on the modified Beckmann-Kirchhoff theory, γ_{TM} is the Fresnel reflection coefficient for the transverse magnetic (TM) polarized wave on a smooth surface, and $\rho(f,t)$ is the Rayleigh factor to describe the roughness of surface. Detailed derivation of the above parameters can be found in [17] and [83]. Apparently, the LoS path conserves the most energy of signal compared to multipath components through reflection and scattering. Therefore, in design of path tracking algorithms, we should focus on the dynamic moving direction of the LoS path in order to keep a satisfying signal-to-noise ratio.

4.2.2 Path propagation with time variation

In THz band, the LoS path provides an unobstructed link from Tx to Rx, hence its power is only affected by free space path loss and molecular absorption. The attenuation caused by molecular absorption is considered as a constant given center frequency f_c and static temperature. The Friis free-space path loss and delay for the LoS component can be expressed as

$$PL_{LoS}(t) = 20\log_{10}\left(\frac{4\pi d(t)}{\lambda_c}\right), \tag{4.5}$$

$$\tau_{LoS}(t) = \frac{d(t)}{c}, \tag{4.6}$$

where c is the speed of light.

Unlike the LoS path, multipaths undergo more complicated interactions with the surroundings along time variation and each interaction will induce extra attenuation. Among the most common mechanisms seen in channels (i.e. specular reflections, edge and wedge diffractions, and diffuse scatterings), specular reflections and diffuse scatterings are of most interest in THz channel. As for reflections and scatterings, we divide the paths into three types of path segments, which are from Tx to the first point of incidence at the surface of material $PS_{Tx\to n_1}$, between points of incidence $PS_{n_m\to n_{m+1}}$, and the last point of incidence to the Rx $PS_{n_M\to Rx}$, respectively. In particular, from Kirchhoff theory of scattering with statistics of surface roughness [84], the total path loss of the i-th multipath at the time t can be expressed as the summation of those path segments and the losses at points of incidence which are dependents of the type of surface material and the angle of incidence, as follows,

$$PL_{NLoS}(t) = 20\log_{10}\Bigg(\frac{4\pi}{\lambda_c}\Big(\Big|d_{PS_{Tx\to n_1}}\Big| \cdot g_c(f_c,t)_{Tx\to n_1} + \sum_{m=1}^{M-1}\Big|d_{PS_{n_m\to n_{m+1}}}\Big| \cdot g_c(f_c,t)_{n_m\to n_{m+1}} + \Big|d_{PS_{n_M\to Rx}}\Big| g_c(f_c,t)_{n_M\to Rx}\Big)\Bigg), \tag{4.7}$$

where $d_{PS_{(\cdot)\to(\cdot)}}$ denotes the path length between two ends of the path segment.

4.3 Dynamic Channel Tracking in THz Band

In a time-varying channel, the channel state changes as UE moves, which results in the channel state outdate problem. Due to the extreme small wavelength at THz, even with a small moving speed of a pedestrian at $1.2\ \mathrm{m/s}$, the Doppler frequency $f_d = |\mathbf{v}|/\lambda_c$ yields a large number with approximately 1.2 kHz at 0.3 THz, and the coherence time of channel $\tau_{coh} = \sqrt{9/16\pi}/f_d$ is approximately 0.35 millisecond (ms), which shows a very fast variation. Therefore, the current solution in IEEE 802.11 standard series which updates the channel at least every $10\ \mathrm{ms}$ cannot be applied in THz band system. Additionally, too frequent channel state update is not feasible since the overhead in each transmitted frame will be extremely large that reduces the spectrum efficiency. To overcome this problem, we propose to separately track the LoS path and multipaths and use the extended Kalman filtering for an accurate trajectory tracking for LoS path while apply the CTMC for approximate tracking for multipaths in THz band without sacrificing system efficiency.

4.3.1 Extended Kalman filtering for LoS path tracking

Kalman filtering is an accurate prediction algorithm to estimate the unknown variables in a linear system [87]. However, the spatial and temporal parameters' evolution along time in a THz channel may not form a linear system. In order to characterize the most important path parameters in a comprehensive 3D space as well as time domain, we apply the *extended*

Kalman filtering (EKF) in the state space model of spatial and temporal attributes. First, we discretize the continuous channel into various time slots with a group factor of coherence time. The group factor chosen in an indoor office environment is 10 since it represents a very small movement of the UE ($\sim 4\,\mathrm{mm}$). Then we express the sate vector at the j-th time slot as $\chi^{(j)} = \left[\alpha^{(j)}, \tau^{(j)}, \phi^{(j)}, \theta^{(j)}\right]^{\mathsf{T}}$, which represents the LoS path's strength, delay, azimuth angle of arrival, and elevation angle of arrival, respectively. The state vector has a dimension of $\mathrm{L} \times 1$, where L represents the number of channel parameters of interest and in this case $\mathrm{L} = 4$. The dimension of L can also be extended for higher estimation accuracy. The EKF requires the following parameters, χ as the state vector, μ as the estimated error covariance matrix, Ψ as the state transition matrix, y as the observation vector, and Φ as the observation matrix [87].

State transition model

The discrete-time state transition equation of the EKF in THz channel is given as

$$\chi^{(j+1)} = \Psi\chi^{(j)} + \mathbf{w}^{(j)}, \tag{4.8}$$

in which $\mathbf{w}^{(j)} \sim \mathcal{N}(\mathbf{0}, \mathbf{Q}^{(j)})$ is the state noise with a covariance matrix $\mathbf{Q}^{(j)}$ defined as $\mathbf{Q}^{(j)} = \mathrm{diag}(\sigma_\alpha^2, \sigma_\tau^2, \sigma_\phi^2, \sigma_\theta^2)$. Since the four entries in the state vector are independent to each other, Ψ can be expressed as

$$\Psi = \mathrm{diag}(\Psi_\alpha, \Psi_\tau, \Psi_\phi, \Psi_\theta), \tag{4.9}$$

where $\Psi_{(.)}$ denotes the transition of each channel parameter. The observation model is expressed as a function between predicted χ and observation matrix Φ as well as observation noise $\mathbf{u} \sim \mathcal{CN}(\mathbf{0}, \mathbf{R})$,

$$y^{(j+1)} = \Phi\chi^{(j+1)} + \mathbf{u}^{(j+1)}, \Phi = 0.1 \cdot \mathbf{I}_4. \tag{4.10a}$$

Path tracking and updating

Based on the relationships among Kalman filtering parameters, we can form the update equations as follows,

$$\chi^{(j+1|j)} = \Psi\chi^{(j|j)}, \tag{4.11}$$

$$\mu^{(j+1|j)} = \Psi\mu^{(j|j)}\Psi^{\intercal} + \mathbf{Q}, \tag{4.12}$$

$$K^{(j+1|j+1)} = \mu^{(j+1|j)}\Phi^{\intercal}(\Phi\mu^{(j+1|j)}\Phi^{\intercal} + \mathbf{R})^{-1}, \tag{4.13}$$

$$\chi^{j+1|j+1} = \chi^{j+1|j} + K^{j+1|j+1}(y - \Phi\chi^{j+1|j}), \tag{4.14}$$

$$\mu^{j+1|j+1} = \mu^{j+1|j} - K^{j+1|j+1}\Phi\mu^{j+1|j}. \tag{4.15}$$

Therefore, the state transition is updated along time with the feedback of observation in real THz channel. The timer function in MATLAB shows that the average update time for 1000 interactions is less than $3\ \mathrm{ms}$ which is within the duration of one time slot. In subsubsection 4.4.2 we demonstrate the performance of the EKF tracking method for LoS path.

4.3.2 Continuous-time Markov chain for multipaths

Some previous work proposed to use EKF for tracking multipaths since this approach provides a robust estimation for time-varying channel parameters [88]. However, in THz channels, the multipaths are highly attenuated compared to LoS path (as shown in Equation 4.4), and the fact that some old MPCs will disappear and new ones will appear will increase time complexity in computation. Therefore, we propose to use the continuous-time Markov chain (CTMC) to track multipaths.

Since Markov chain has an important memoryless property that future behavior of the model only depends on the current state and not on previous ones, we can characterize the ray behavior in time-varying channel utilizing the special case of the continuous-time

Markov chain, which is the birth-death process. The paths' behavior in the continuous-time Markov chain can be categorized into three states corresponding to birth, presence, and death, respectively [82]. In CTMC, the probability of appearance between two time intervals, which is defined as δ_B and is much smaller than the coherence time, follows an exponential distribution as $\delta_B \sim \exp(1/\lambda_B(t, f_c))$, in which $\lambda_B(t, f_c)$ is the time and frequency dependent birth rate of the birth-death process. The lifespan of a MPC (denoted as δ_l) also follows an exponential distribution $\delta_l \sim \exp(1/\lambda_D(t, f_c))$, and $\lambda_D(t, f_c)$ is the death rate of the birth-death process and also depends on time and frequency.

4.4 Channel Simulation and Characterization

4.4.1 Channel simulation procedures

The simulation starts from the initialization, in which we deploy a 3D ray-tracing method to determine the environment and the initial fading process, delay, and the directions of departure and arrival of paths. The deterministic statistics are obtained by a MATLAB-based ray-tracing tool that we developed and validated with current 3GPP channel models [89] to characterize the 3D channel. The simulation input parameters include the initial positions and velocities of Tx and Rx, the antenna patterns used by both parties, layout and resolution of the surrounding environment, relative permittivity of surrounding materials, and so on. In this chapter, we assume that the Tx antenna is the graphene antenna array described in subsection 4.3.2 and Rx is an isotropic antenna, and the main lobe of the Tx antenna array is steered towards the direction of the Rx. The second step of simulation is deploying the EKF for LoS path and CTMC for multipaths that characterizes the dynamic behavior of MPCs based on environment parameters. The final step is the parameterization of the channel along time evolution. An office environment is adopted in our work as the simulation environment, which includes common furniture, such as office desks, chairs, and bookshelves.

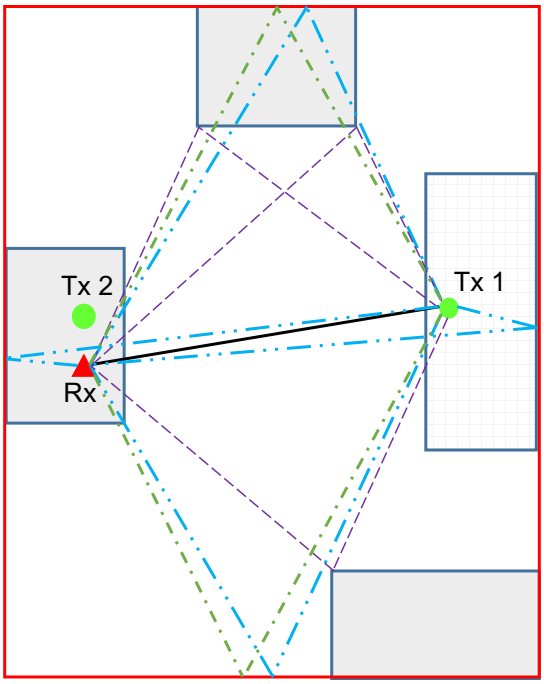

Figure 4.1: The ray-tracing result at the initial time at 0.3 THz from the simulated indoor office environment. The black solid line represents the LoS path, the blue dash lines denote the reflection paths, while the purple dash lines represent the scattering paths.

4.4.2 Channel characterization and analysis

Using the proposed time-varying channel model, we can characterize the channel parameters.

LoS path tracking

With the EKF tracking algorithm, we can examine simulation results of the LoS path along UE's movement. Since both the Tx and Rx are above the surrounding objects, the LoS path always exists as the strongest path. Figure 4.2 shows the tracking results for the LoS path based on the AoA, AoD, and delay. The mean square error from comparison of estimation and observation is shown in Figure 4.3. The estimation accuracy increases as the transmission distance becomes larger because the Tx has better knowledge about the channel as Rx moves.

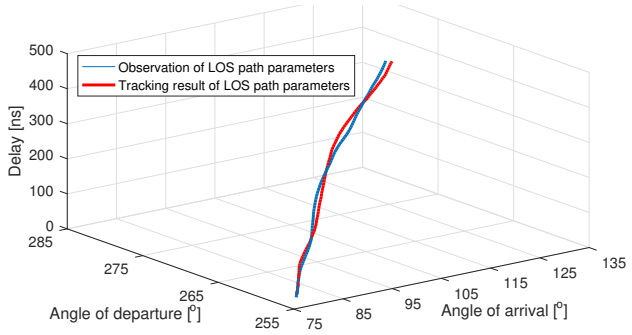

Figure 4.2: Comparison of tracked LoS path parameter set and the actual data.

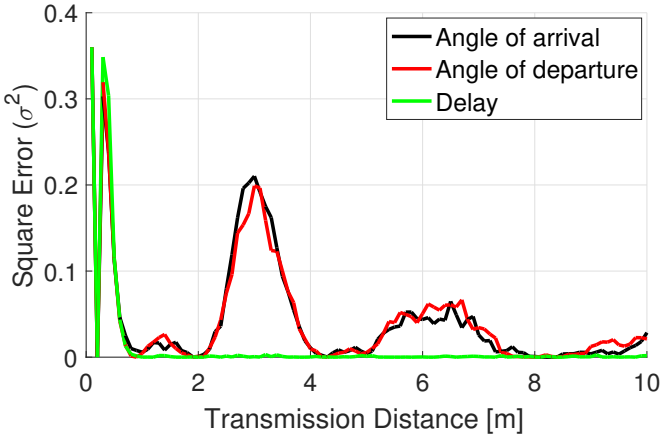

Figure 4.3: Square error of the Kalman filtering results compare to actual data.

Rician K-factor

The Rician K-factor is an important and commonly used parameter to describe the relative power strength of the LoS component. In a time-varying THz channel, the Rician K-factor is time and frequency dependent, which can be expressed as

$$K(t) = 10\log_{10}\left(\frac{P_{LoS}(t)}{\sum_{i=1}^{I_{NLoS}} P_{NLoS,i}(t)}\right), \tag{4.16}$$

where $P_{LoS}(t)$ and $P_{NLoS,i}(t)$ are the power of the LoS path and the i-th multipath, respectively. Our simulation result shows that the K-factor increases as the transmission distance increases since the total power of multipaths fades faster than that of the LoS path. Figure 4.4 shows the K-factor for different frequencies along time-varying transmission

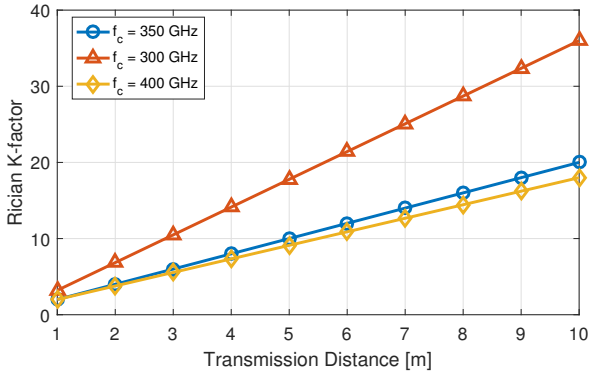

Figure 4.4: Rician K-factor at 0.3 – 0.4 THz based on ray-tracing simulation results.

distance.

Path Gain and System Capacity

The large scale parameters of path gain and system capacity are also crucial in characterizing time-varying channels. The path gain can be calculated by summing the received power of all arrived rays and subtract the transmit power, as follows,

$$PG(t) = \sum_{i=1}^{I(t)} \alpha_i(t)^2 - P_{Tx}. \tag{4.17}$$

As both ends move, we can observe the difference in path presence and absence, path strengths, and delay spreads. We assume that the frequency-selective channel contains additive white Gaussian noise, with N_0 as the noise power spectral density, and received power as $P_{Rx}(t)$. The capacity of a time-varying channel model can thus be expressed by [17]

$$C = \sum_{n=1}^{N_B} \Delta f_n \log_2 \left(1 + \frac{P_{Tx}|H(t, f_n)|^2}{N_0(t, f_n)\Delta f_n}\right), \tag{4.18}$$

in which n is the index of subband, N_B is the total number of subbands allocated in the spectrum, and $H(t, f)$ is the channel transfer function as shown in Equation 4.2. Figure 4.5 depicts the comparison of channel capacity between the theoretical value using the water-filling algorithm in [83] and the dynamic LoS path tracking algorithm. It is shown that

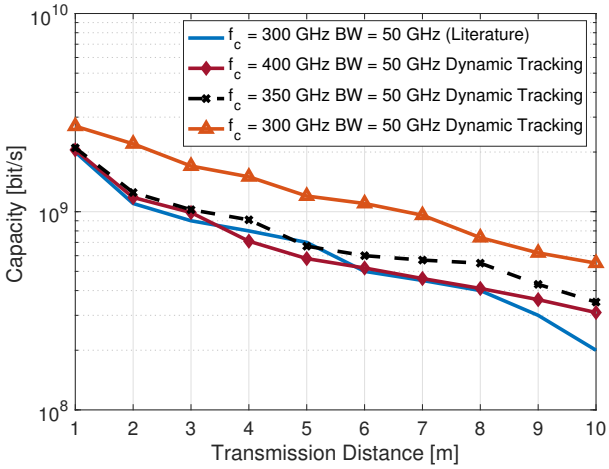

Figure 4.5: The capacity comparison between the proposed dynamic tracking method and the theoretical value from [83] in 0.3 THz time-varying channel.

with the dynamic tracking enabled by graphene antenna array, even when only Rx knows the time variation in channels, the capacity still yields satisfying performance.

4.5 Summary

In this chapter, we present a time-varying channel modeling and tracking approach in 3D indoor environments for THz band communication systems. The channel model can be especially useful in facilitating realistic channel estimation that requires a high level of accuracy without sacrificing the time efficiency. Our model introduces the extended Kalman filtering and continuous-time Markov chain to model and track the dynamic path behavior for LoS path and multipaths, respectively. Moreover, the simulation results at various frequency bands show a good general applicability of the time-varying channel model in THz channel, with analysis of major time-varying channel characteristics. Finally, the simulation results based on the proposed model are validated by 3D ray-tracing.

CHAPTER 5
CHANNEL MODELING AND ANALYSIS FOR INTER-SMALL-SATELLITE LINKS

5.1 Motivation and Related Work

The growing demands in the Internet of Things motivate a faster and more reliable network to accommodate more verticals of communication scenarios, which include aerial and space communications in addition to conventional terrestrial networks. To this end, a recently proposed concept of the *Internet of Space Things (IoST)* has focused on enabling CubeSats to form a space network to transfer data with ubiquitous coverage [90]. The CubeSats (or nanosatellites) are a category of small satellites (with classification shown in Table 5.1), which usually weigh less than 180 kilograms and have smaller profiles in size, weight, and power (SWaP) compared to conventional satellites [91]. Previously, the scope of design and deployment of small satellites has been limited to astronomical spectroscopy and remote sensing [92]. The IoST, enabled by a network of small satellites, is envisioned to utilize small satellites for data communications and achieve a high throughput on the level of multi-hundred-gigabits-per-second (Gbps), in parallel to serve inaccessible areas of traditional network infrastructure and provide secure connectivity [93].

Distinct from conventional satellites serving in LEOs, MEOs, and GEOs that have long development cycles and high development costs, small satellites are more flexible and cost-friendly with the utilization of commercial off-the-shelf components. In addition to the small satellite missions on passive sensing applications in Earth science, astronomy, and astrophysics observations, there also emerges a surge in *satellite formation flying* missions [94], where multiple small satellites join a pattern with close proximity to perform remote sensing, data exchange, among other tasks. The success of such missions requires

Table 5.1: Classification of small satellites (SmallSats) [91, 95]

Category of small satellites	Mass [kg]
Minisatellites	100–180
Microsatellites	10–100
Nanosatellites (CubeSats)	1–10
Picosatellites	0.1–1
Femtosatellites	< 0.1

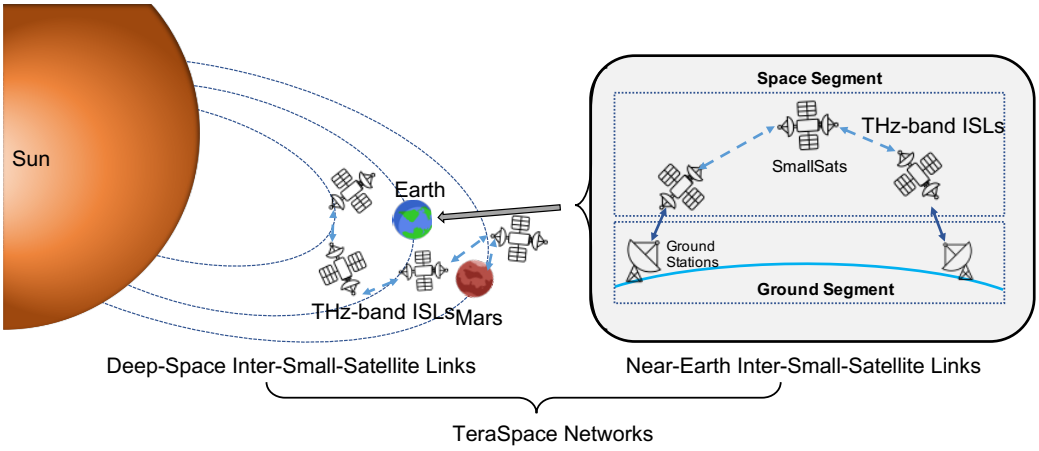

Figure 5.1: Illustration of the TeraSpace Networks with two types of inter-small-satellite links: deep-space and near-Earth links, respectively (small satellites are enlarged in drawing to show the links).

reliable connection among satellites to efficiently transfer both data and state information. In addition, rising exploration missions to study the solar system and beyond also necessitate low-delay communication links over millions of kilometers.

Current satellite communications rely on microwave bands, ranging from the L-band (1–2 GHz) till the Ka-band (26.5–40 GHz), as well as optical/laser communications [93]. On one hand, although having proved their efficacy in data transmission over the past decades, with an increasing number of deployed satellites sharing the allocated spectrum, these frequency bands gradually become congested and are barely capable to sustain desired performance [95, 96]. Moreover, the densely allocated spectrum shared by thousands of satellites currently orbiting the Earth leads to strong interference, which further de-

grades the link quality. On the other hand, optical/laser communications for satellites have attracted attention due to their wide and unlicensed spectrum resource to support gigabits-per-second links among satellites. However, optical links have rather strict requirements on pointing accuracy, for example, 14.6 arcsec at 580 km to achieve 20 Mbps throughput [97], due to their very narrow beamwidth. Hence, optical links are susceptible to orbital perturbations caused by gravitational and solar effects, which can lead to beam misalignment in inter-satellite links. Nevertheless, the THz band has not been extensively studied for data communications in satellite networks. Such underexplored spectrum band has recently been analyzed for terrestrial networks, due to their abundant spectrum resources; however, due to the presence to water vapor molecules and other terrestrial propagation effects, the THz band faces the issue of transmission distance limitation [20]. However, such concern does not exist in either deep space or Earth's upper atmosphere, where the atmosphere becomes extremely sparse. As shown in Figure 5.1, the inter-small-satellite links are the major components of the space segment of the TeraSpace Networks in both near-Earth and deep-space scenarios. Therefore, the THz band becomes a natural candidate for inter-small-satellite links to achieve the Tbps-level throughput with its broad spectrum.

So far, current usage of some THz frequencies is limited in the passive sensing to study solar and astronomical activities [98]. It is foreseeable that a joint sensing (including both passive and active sensing) and communication scheme will utilize the THz band for ultra-high throughput links on the same satellite. In addition, since the THz band has a higher tolerance of beam misalignment due to the relative wider beamwidth supported by phased antenna arrays, compared to the optical communication counterpart, the same symbol estimation performance can be achieved with less stringent pointing accuracy [99]. Moreover, the advantage of much reduced footprints of antenna array design in the THz spectrum makes it deployable on small satellites, as compared with antennas with diameters on the order of several meters at microwave frequencies.

However, before these prospects of THz band satellite links become a reality, research

challenges for inter-satellite communications, especially at THz band, need to be resolved. Current research gap includes a lack of understanding of the propagation characteristics in the inter-satellite channel, which locates at the Earth's upper atmosphere and in the deep space, and a detailed analysis on link performance. Therefore, in this chapter, we propose the TeraSpace communication link design for both near-Earth and deep-space scenarios with an orbital perturbation model to analyze the spectral efficiency. This chapter consists of the following aspects:

- A detailed analysis of the effect of Earth's upper atmosphere on near-Earth ISLs and solar activities on deep-space ISLs operated in the THz band. The effects of the charged particles in both the ionosphere and in circumstance of solar wind are characterized. In particular, it is demonstrated that even though ionized particles are active in the ionosphere and can affect the stability of microwave links in existing satellite networks, it will not cause noticeable impact on THz links, making THz band a feasible carrier for ISLs. Furthermore, for deep-space links, the relationship between the angle of beam misalignment with the ISL's distance from the Sun is quantified.

- A study of the relative motion between a pair of small satellites during formation flying with a proposed a model for orbital perturbation caused by gravitational force, Earth's oblateness, and solar radiation pressure. It is proven that the relative motion of satellite beams in the same circular orbit is bounded, which provides a theoretical foundation to characterize the beam misalignment using a wrapped Gaussian distribution.

- Based on characterization of inter-small-satellite channels and recognizing the potentials of polarization and frequency diversity in achieving high throughput, a channel model that exploits these channel peculiarities and diversity schemes is proposed. In particular, the link metric of spectral efficiency under different link conditions,

transmit power levels, and polarization configurations for the TeraSpace Networks is analyzed.

The following notations are used in this chapter: $\mathbf{a}$ represents a vector, $\dot{\mathbf{a}}$ represents a velocity, $\ddot{\mathbf{a}}$ represents an acceleration, a denotes a scalar, $\mathbf{A}$ denotes a matrix, * represents the Hermitian transpose, and $||\cdot||$ denotes a vector norm.

5.1.1 Inter-Satellite Link Capability and Channel Modeling

In current satellite communication systems, data links between two satellites are implemented using existing microwave bands or optical/laser beams. For example, an 800 nm ($\sim$375 THz) laser was deployed in the Artemis satellite to achieve a 50 Mbps throughput for remote sensing [100].In addition, the Artemis was equipped with an S-band (at 2.1 GHz) or Ka-band (at 23/26 GHz) data relay link with a maximum 150 Mbps achievable rate[1]. In another case, the S-band channels are configured with multi-antennas for ISLs to relay data in the Tracking and Data Relay Satellite System (TDRSS) [101]. The Starlink satellites, launched by SpaceX, undergo different phases of ISL design. The first batch of 60 Starlink satellites were not equipped with the ISL capability, which had to rely on ground stations to relay data, thus resulting in excessive delays. Later launched Starlink satellites use laser beams for ISLs. The heavily used microwave bands, along with limited or no ISL capability, restrict satellite communication network's potentials to achieve higher throughput and better service quality. Moreover, current satellites which are equipped with both microwave and optical transceiver systems for separate sensing and data relay purposes generally have a larger form factor in payload than those with a single transceiver system, making them less energy efficient and more costly in deployment.

Existing satellite communication channel models mostly focus on the channel in the ground segment, which is between a mobile or ground terminal and a satellite. In [102], a statistical model is derived to characterize the received signal power with multipath effect

[1] https://earth.esa.int/web/eoportal/satellite-missions/a/artemis

induced by scattering and shadowing due to channel fluctuation. Moreover, the Ka-band channel is also strongly affected by environmental factors that can impact the quality of received signal. In [103, 104], since the uplink and downlink Ka-band signals need to traverse multiple layers of the Earth's atmosphere, a model is thus proposed that suggests weather effects, including rain attenuation, gaseous absorption, cloud attenuation, and scintillation, can impose BER degradation to signals. Furthermore, with the maturity of multiple-input-multiple-output (MIMO) communication techniques, spatial and polarization diversity can be achieved in channels between satellites and ground stations [105]. These studies have laid a solid foundation for establishing a reliable link between space and ground. However, to the best of our knowledge, there exists a research blank in THz band communication channel model and analysis for inter-small-satellite links, and currently available models at microwave frequencies cannot be applicable due to frequency-dependent channel attributes. With the rising potentials of small satellites forming networks in space, it is essential to fill the research gap of THz band channel characterization in the space segment.

While several space-borne telescopes adopted infrared and THz bands for celestial observation, there has been no active data link or channel model available in this spectrum for ISLs. A related channel model characterizing the usage of THz spectrum between ground stations and satellites is reported in [106], which describes the impact of atmospheric precipitable water vapor on link quality and suggests feasible locations for ground stations to establish THz band links. Later work by the same author suggests the feasibility of Tbps-link between ground and satellite with a link at altitudes ranging from low-Earth to geostationary orbits using large-aperture antennas at dry locations [107]. However, these studies also focus solely on the ground segment of the satellite communication network, while the space segment should also be brought attention to complete the Tbps-level data link paradigm for future satellite communication network.

5.1.2 Satellite Beam Pointing, Acquisition, and Tracking

Establishing a reliable satellite link requires high precision in beam pointing. Additionally, due to the constant movement of satellites, beam acquisition and tracking along orbit pose strict time and accuracy requirement. The pointing error had led to a complete mission failure of the Malaysian small satellite RazakSAT in 2009, rendering no image usable for its originally planned remote sensing study. Moreover, in deep space, solar weather affects satellite pointing accuracy. For example, the Galileo orbiter, whose mission is to study the Jovian system, experiences solar conjunctions every 13 months. Especially in case of a superior solar conjunction, during which the Galileo spacecraft, the Sun, and the Earth are aligned perfectly (with the Sun in between), the on-board S-band communication link can be severely degraded due to the charged particles densely distributed along the link. The strategy deployed at Galileo is that when the Sun-Earth-probe (SEP) angle becomes smaller than 22°, the modulation index and bandwidth are adjusted. Specifically, the modulation index is reduced to increase the emitted power and the bandwidth is increased to maintain a locked phase loop under induced phase scintillation. However, when the SEP angle is less than 7°, commanding becomes prohibited [108].

Current pointing, acquisition, and tracking (PAT) solutions for small satellites employ narrow laser beams due to their small footprint to avoid interference and good cost efficiency in SWaP. Among existing prototypes, the Cubesat Infrared CrosslinK (CLICK) mission is developed for a CubeSat with a goal of achieving 20 Mbps for ISL range greater than 855 km [97]. In this mission, the PAT is realized through a two-stage procedure: an initial pointing is realized by the attitude determination and control system (ADCS) with a wide field of view and limited accuracy, and then supplemented with a fine-pointing procedure to improve pointing precision. Such fine pointing is achieved using a feedback mechanism from a quadrant photodiode detector controlled by a micro-electron-mechanical (MEMS) fast-steering mirror. The resultant precision can tolerate up to 14.6 arcsec (0.004 degree) of angle divergence from its full-width half-maximum (FWHM), or

half-power (3-dB) beamwidth (HPBW). Another reported solution for NASA's TeraByte InfraRed Delivery (TBIRD) demonstration in [109] also utilized a similar scheme with a quadrant photodetector sensor. However, this approach is proposed to execute pointing control and communication simultaneously. It is worth noting that these reported PAT approaches mainly target at LEO satellites with ISL capabilities; hence, in deep-space scenarios where more complicated and dynamic perturbation factors cause beam divergence, the performance may undergo a higher degradation. Therefore, a perturbation model for both near-Earth and deep-space orbits should be characterized to take into account different disturbing forces.

Summarizing the surveyed related work, current satellite communications lack a thorough understanding of channel behavior in the space segment, which should take into account the space environment, including charged particles due to solar activities, as well as orbit perturbation caused by numerous factors including the Earth's irregular shape and other external forces. Based on a fully characterized channel model, a link performance analysis is necessary to demonstrate the potential of THz band communications in space.

5.2 Characterization of THz Band ISL Channels

In this section, we characterize the propagation channel in THz spectrum for ISLs. Depending on the altitude or distance of satellites from Earth, ISL channels can be categorized as (i) near-Earth and (ii) deep-space channels, respectively. In this section, we analyze propagation features of these two channels separately.

5.2.1 Near-Earth Channel

The near-Earth propagation channel has an altitude above 400 km and is upper bounded by the geostationary orbit at around 36,000 km. The inter-satellite communications within such range bear significant differences from the ground-to-satellite link. First, the previously considered tropospheric effects, such as attenuation and absorption caused by rain,

cloud, and fog which occur in the 8–14 km altitude range, can be ignored in the near-Earth ISLs. Second, in the Earth's upper atmosphere, the air becomes remarkably thin, indicating a scarcity of gas or water molecules. Hence, the inter-satellite channels are immune from scintillation effect caused mainly by such small particles.

Nevertheless, the inter-satellite channels at THz band face other issues. A typical one is the electromagnetic (EM) wave propagation through the plasma in the ionosphere. The ionosphere is an ionized layer of Earth's upper atmosphere that overlaps with the exosphere. It spans in a wide altitude range from approximately 60 km to 1,000 km. Ionized by solar radiation, the layer can be seen as an infinitely large and magnetized plasma, whose parameters vary greatly per location and time (an example shown from Figure 5.2a to Figure 5.2d at different times and altitudes). Accordingly, the EM wave propagation in the ionosphere is influenced by the free electrons and ions, which forms the ionospheric plasma. Two metrics are widely used to describe the EM wave propagation in the medium of ionospheric plasma, namely, the plasma frequency and the depolarization caused by the Faraday rotation.

Plasma frequency

The plasma frequency is a measure of oscillation frequency of free electrons and ions due to the Coulomb force in the electric field and it can be expressed as

$$f_{pe} = \frac{1}{2\pi}\sqrt{\frac{n_e e^2}{\varepsilon_0 m_e}}, \tag{5.1}$$

where n_e denotes the electron density in the ionosphere, $e = 1.6021 \times 10^{-19}$ Coulombs is the electron charge, $m_e = 9.109 \times 10^{-31}$ kg is the mass of a single electron, and $\varepsilon_0 = 8.854 \times 10^{-12}\ \mathrm{F/m}$ denotes the vacuum permittivity. Since an ion has a much larger mass compared with that of an electron, the plasma frequency of ions is much lower, which can be ignored in the discussion of RF propagation. It is observed that the plasma frequency

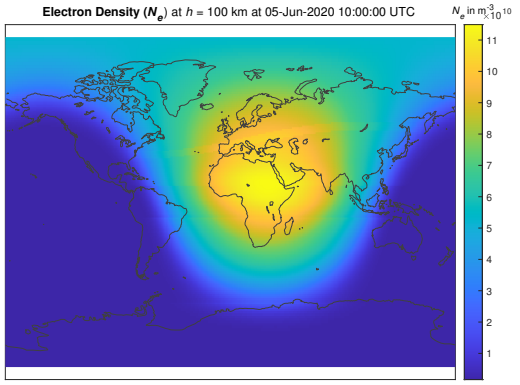

(a) Electron density profile with an altitude of 100 km at 10:00 UTC on June 5, 2020.

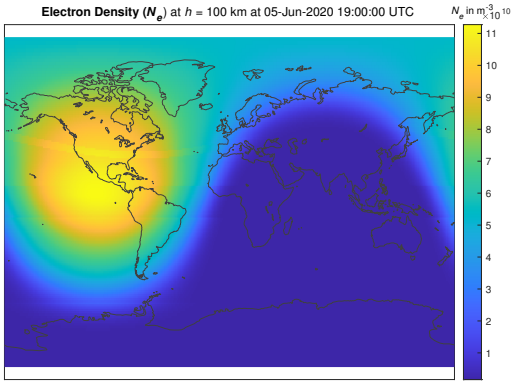

(b) Electron density profile with an altitude of 100 km at 19:00 UTC on June 5, 2020.

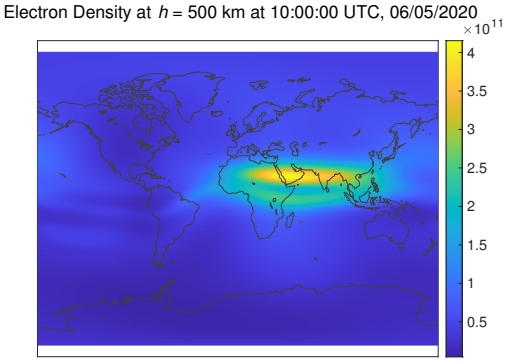

(c) Electron density profile with an altitude of 500 km at 10:00 UTC on June 5, 2020.

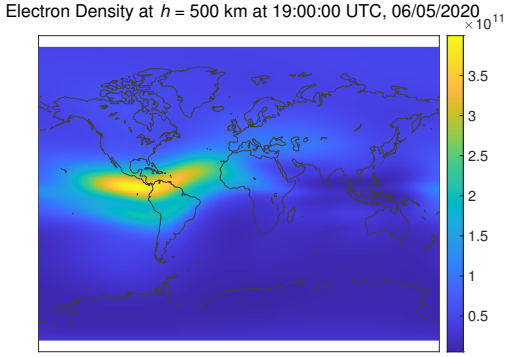

(d) Electron density profile with an altitude of 500 km at 19:00 UTC on June 5, 2020.

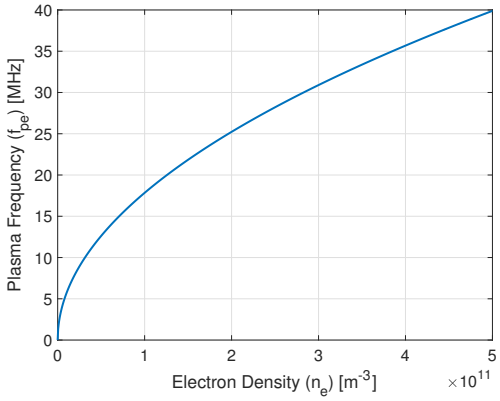

(e) Plasma frequency vs. electron density profile.

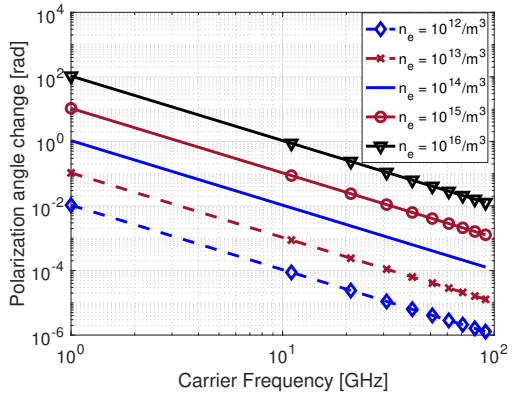

(f) Faraday rotation vs. electron density profile.

Figure 5.2: Variations in electron densities globally and corresponding plasma frequencies.

solely depends on the electron density, which varies with geographic location, altitude, observation time, electron temperature, and so on. A comprehensive model to profile the

global distribution of electron density is the international ionosphere reference (IRI) model. As shown in Figure 5.2a and Figure 5.2b, at different observation times (e.g., at 10:00 and 19:00 UTC) on the same day at an altitude of 100 km, the global peak on the order of $10^{10}/\mathrm{m}^3$ of electron density migrates westward. In addition, as shown in Figure 5.2c and Figure 5.2d, a similar electron density peak migration trend can be found, while such peak values are higher (reaching the level of $4 \times 10^{11}/\mathrm{m}^3$) as the altitude increases. When computing the plasma frequency with the IRI statistics using Equation 5.1 and plotting the result in Figure 5.2e, it is observed that the corresponding plasma frequencies fall into the high frequency (HF) range. Typically, if the frequency of an RF signal is above the plasma frequency, the signal will be refracted according the Snell's law; however, if the RF frequency is much higher compared to the plasma frequency, its propagation will not be affected. Therefore, the propagation channel in THz spectrum will not be affected by the variation of electron density in presence of a quiet ionosphere with electron density below the level of $10^{12}/\mathrm{m}^3$.

However, when the ionosphere undergoes occasional extreme conditions such as severe solar flares, an excessive amount of electrons can be radiated from the Sun before reaching Earth. Solar flares cause strong fluctuation in electron density to disrupt various communication activities. For instance, a reported observation of a super flare at the level of X9.3[2] during solar cycle 24 on September 6, 2017. Under the severe solar cycle, the electron density can reach a level of $10^{12}/\mathrm{m}^3$, resulting a plasma frequency in the very high frequency (VHF) band, which causes interruptions to terrestrial wireless communication systems, such as analog television operating at this band. The strongest solar flare thus far recorded occurred on November 4, 2003 with an intensity of X45, leading to a temporary failure of the Solar and Heliospheric Observatory (SOHO) satellite and a damaged Advanced Composition Explorer (ACE) by NASA[3]. Such excessive solar activities can disrupt up to L-band, at which the Global Positioning System (GPS) operates, lead-

[2]X represents the highest severity of solar flares with solar flux at the level of 10^{-4} W/m^2.
[3]https://www.nasa.gov/topics/solarsystem/features/halloween_storms.html

ing to erroneous satellite ranging and navigation. Consequently, misaligned ISLs lead to communication failure.

Even though particles within plasma can be accelerated in magnetic and electric field and hence cause collisions, the effective collision frequencies of all possible combinations of charged particle scattered in plasma, including electrons and ions, do not exceed 50 kHz [110], hence preserving mmWave and THz band signal power along propagation.

Depolarization

The ionosphere can also cause depolarization of EM waves, an effect known as the Faraday rotation. However, the resultant change in polarization angle is a function inversely proportional to the square of carrier frequency [110], which can be expressed as

$$\Delta\phi_{\mathrm{FR}} = 236\bar{B_{\mathrm{G}}}f^{-2}\int_{\mathrm{L}} n_e(l)dl, \tag{5.2}$$

where $\bar{B_{\mathrm{G}}}$ is the average Earth magnetic field with a range of 25 to 65 $\mu\mathrm{T}$, f the carrier frequency, $n_e(l)$ the electron density along path L. As the carrier frequency increases, the depolarization effect becomes less significant, making the THz band immune to this issue. It is observed from Figure 5.2f that ionospheric plasma with an average quiet level of $n_e = 10^{12}/\mathrm{m}^2$ will not cause noticeable angle rotation for signals above 10 GHz, and only excessively strong electron density (at the level of $10^{16}/\mathrm{m}^2$) will affect low THz spectrum with a rotation of 0.012 radian. Moreover, this attribute becomes favorable as polarization diversity can be utilized to strengthen link performance (as will be discussed in section 5.4).

5.2.2 Deep-Space Channel

The deep-space channel is herein defined as ISLs between satellites located beyond Earth's geostationary orbits, including cislunar space, Mars, and beyond. In such channel, due to some satellites' proximity to the Sun, solar activities, such as the solar conjunction effect,

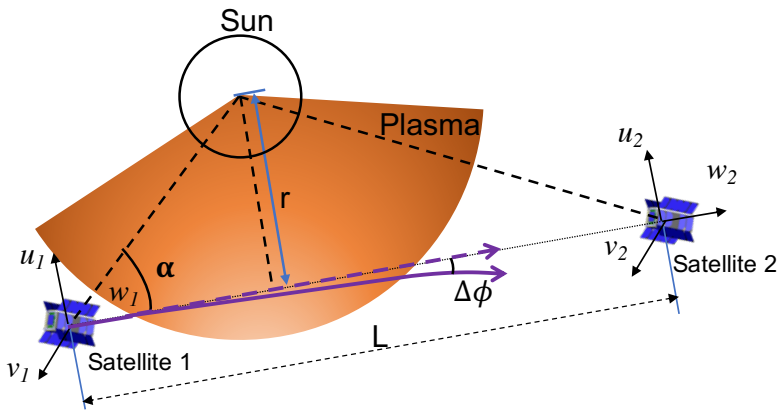

Figure 5.3: Illustration of an ISL in deep space during solar conjunction. The impact distance is denoted as r, and α is the angle formed by the lines connecting the Sun and satellites. At and beyond the critical angle $\alpha_{\min}$, super solar conjunction happens and prohibits communication.

exacerbate link degradation. In addition, cosmic noise is not negligible in characterizing total received noise.

Cosmic microwave background radiation

In deep space, besides the effect of solar activities, another source of radiation that affects the receiver performance is the cosmic microwave background (CMB) radiation, which originates from the cosmic expansion. The CMB has a peak radiance at 282.1 GHz with a thermal blackbody temperature at $T_{\text{CMB}} = 2.72548 \pm 0.00057$ K [111]. The second term denotes an uncertainty due to measurement instruments.

Solar conjunction

The solar activities that can affect the deep-space communications include solar flares and solar wind. Solar flares are discrete events that occur with the 11-year solar cycle, which is less frequently than the solar wind. The solar wind contains constant release of charged particles from the Sun. In deep-space links, when the transceivers locate at different sides of the Sun, the phenomenon of solar conjunction happens, as illustrated in Figure 5.3. Communications are prohibited when satellites undergo solar conjunctions. Similar to the

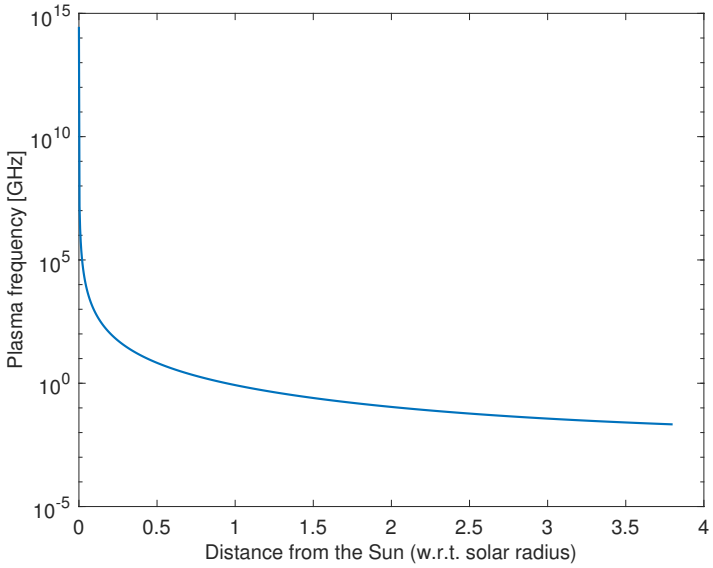

Figure 5.4: Plasma frequency as a function of heliocentric distance r to the signal path between two satellites.

ionospheric plasma, there exists a relationship between the severity of solar activity and signal carrier frequencies where communications will be interrupted. In addition, a critical metric deciding such relationship is the angle formed by the Sun and the two satellites joining the link. Such critical angle provides a reference for which we can assess the link stability in deep space.

Similar to the near-Earth case, we analyze the impact of space weather on deep-space links by characterizing the relationship between the plasma frequency and beam angular variation. Different from the IRI model used in the ionosphere to extract electron density profiles, the electron density model in deep space during solar wind is developed in [112, 113] and can be expressed as

$$n_{\mathrm{e}}\,[\mathrm{m}^{-3}] = \frac{2.21 \times 10^{14}}{(r/R_{\odot})^{6}} + \frac{1.55 \times 10^{12}}{(r/R_{\odot})^{2.3}}, \tag{5.3}$$

where $R_{\odot} = 6.96340 \times 10^{8}$ m is the solar radius and r is the impact distance from the sun perpendicular to the direct signal path between the satellites (shown in Figure 5.3). The resultant plasma frequency computed from Equation 5.1 is plotted in Figure 5.4 and

it is noticed that only when the signal path moves in immediate vicinity to the Sun (i.e., $r/R_{\odot} \approx 0$ or $\alpha \approx 0^{\circ}$) that the plasma frequency approaches THz spectrum.

5.3 Orbit Perturbation Modeling and Beam Tracking for Small Satellites

Even though links at THz band are less vulnerable to both ionospheric and deep-space weather effects, as compared to their microwave band counterparts, the satellite body suffers from orbital perturbations caused by external forces. Such disturbance can cause satellites drift from their original positions in their designated orbit. When both satellites forming a data link drift from their planned positions, beam misalignment will occur and cause communication degradation or even disruption. In this section, we focus on the Earth-centered orbits; however, for satellites orbiting other celestial bodies, the approach is also applicable, only with a different standard gravitational coefficient per celestial body. We characterize notable perturbation effects and propose a model to quantify the resultant misalignment for small satellites.

5.3.1 Perturbation Modeling

One of the commonly used perturbation analysis methods is called the general perturbations, which is based on analytical solution for general differential equations pertaining to satellites' position and velocity vectors. For satellites in a circular or elliptical orbit around the Earth, the main force that Earth exerts on them stems from the Earth's gravity, the strength of which depends on the geocentric distance of the satellite. For the convenience of theoretical analysis, the Earth is often modeled with a spherical gravitational field. Hence, for satellite in a circular orbit, such gravitational perturbation remains constant. However, due to the actual shape of the Earth as an oblate spheroid where the equatorial radius is larger than polar radius by approximately 22 km, such oblateness cast a non-negligible effect on satellites, which is called the J_2 effect and will be discussed in detail. We start with the perturbation model with a spherical Earth.

Gravitational effect

When a pair of identical small satellites (denoted as a leader and a follower for differentiation) locate at the same circular orbit with a relatively small distance (usually smaller than the geocentric distance of the orbit), as shown in Figure 5.5, their respective equations of motion per unit mass, or perturbative accelerations $\ddot{\mathbf{r}}_{\mathrm{F/L}}$, are

$$\ddot{\mathbf{r}}_F = -\mu \frac{\mathbf{r}_F}{||\mathbf{r}_F||^3} + \mathbf{f}_F, \tag{5.4a}$$

$$\ddot{\mathbf{r}}_L = -\mu \frac{\mathbf{r}_L}{||\mathbf{r}_L||^3} + \mathbf{f}_L, \tag{5.4b}$$

where μ is the standard gravitational parameter ($\mu \approx 3.986 \times 10^{14}\ [m^3 s^{-2}]$ for Earth), $\mathbf{r}_{\mathrm{F/L}} = [x_{\mathrm{F/L}}\ y_{\mathrm{F/L}}\ z_{\mathrm{F/L}}]^\intercal$ denotes the position vector and $\mathbf{f}_{\mathrm{F/L}}$ denotes other perturbation forces on the follower or leader, respectively. The magnitude of position vectors equals the radius of the orbit (i.e., $||\mathbf{r}_{\mathrm{F/L}}|| = r$). Hence, the relative motion of the follower with respect to the leader under general perturbations can be expressed as

$$\begin{aligned} \ddot{\mathbf{p}} &= \ddot{\mathbf{r}}_F - \ddot{\mathbf{r}}_L \\ &= -\mu \frac{\mathbf{r}_F}{||\mathbf{r}_F||^3} + \mu \frac{\mathbf{r}_L}{||\mathbf{r}_L||^3} + \mathbf{f}_F - \mathbf{f}_L \\ &= -\mu \frac{\mathbf{r}_\mathrm{L} + \mathbf{p}}{||\mathbf{r}_\mathrm{L} + \mathbf{p}||^3} + \mu \frac{\mathbf{r}_\mathrm{L}}{||\mathbf{r}_\mathrm{L}||^3} + \mathbf{f}_\mathrm{F} - \mathbf{f}_\mathrm{L}, \end{aligned} \tag{5.5}$$

where $\mathbf{p} = \mathbf{r}_\mathrm{F} - \mathbf{r}_\mathrm{L}$. Consider the gravitational effect under the assumption of a spherical Earth, where $\mathbf{f}_\mathrm{F} - \mathbf{f}_\mathrm{L} = \mathbf{0}$, Equation 5.5 has the solution known as the *Clohessy-Wiltshire (CW) Equations* [114]. These equations are based on a local-vertical-local-horizontal (LVLH) frame, shown as vectors in solid lines in Figure 5.5 and expressed as

$$\ddot{x} = -2\omega\dot{z}, \tag{5.6a}$$

$$\ddot{y} = -\omega^2 y, \tag{5.6b}$$

$$\ddot{z} = 3\omega^2 z + 2\omega\dot{x}, \tag{5.6c}$$

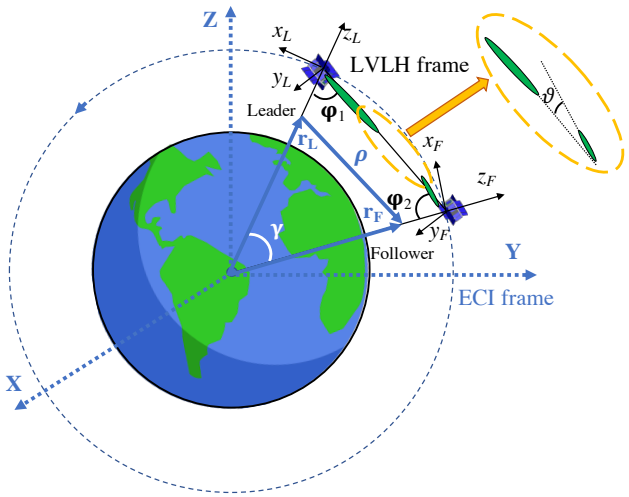

Figure 5.5: Satellite formation flying in the same circular low-Earth orbit. The leader, of which the coordinates have an "L" in subscripts, is regarded as a reference mass point, with the following satellite (i.e., the follower) denoted as an "F" in subscripts.

where $\omega = \sqrt{\mu/r^3}$ is the orbit velocity. In the LVLH frame, as illustrated in Figure 5.5, the z-axis is along the radius vector of the satellite, the x-axis is along the angular momentum vector of the satellite, and the y-axis follows the right-hand rule. So, $\ddot{x}, \ddot{y}$, and $\ddot{z}$ represent the accelerations in these corresponding local directions, $\dot{x}$ and $\dot{y}$ denote the velocities along local directions, while x and y denote local positions. Using Laplace transform, a closed-form solution for the relative position of the follower with respect to the leader as a function of time can be obtained as

$$x(t) = 6(\sin\omega t - \omega t)z_0 + x_0 - \frac{2}{\omega}(1 - \cos\omega t)\,\dot{z}_0 + \frac{4\sin\omega t - 3\omega t}{\omega}\dot{x}_0, \tag{5.7a}$$

$$y(t) = y_0\cos\omega t + \frac{\dot{y}_0}{\omega}\sin\omega t, \tag{5.7b}$$

$$z(t) = (4 - 3\cos\omega t)z_0 + \frac{\sin\omega t}{\omega}\dot{z}_0 + \frac{2}{\omega}(1 - \cos\omega t)\dot{z}_0. \tag{5.7c}$$

It is observed that as time progresses, the terms $y(t)$ and $z(t)$ are always bounded, whereas $x(t)$ has a secular drift term of $-(6\omega z_0 + 3\dot{x}_0)\,t$. To mitigate such secular drift, a condition has to be satisfied that such term equals zero, which means $\dot{x}_0 = -2\omega z_0$.

The J_2 effect

Since the classical CW equations do not take into account the irregularities in the celestial body, such as the Earth's oblateness, which may impose a noticeable disturbance to satellites' orbit, we hereby quantify such perturbation effect when $\mathbf{f}_F - \mathbf{f}_L \neq \mathbf{0}$. In particular, the total external forces exerted on satellites can be written as $\mathbf{f}_{(\cdot)} = \mathbf{f}_{\mathrm{J}_2} + \mathbf{f}_{\mathrm{S}} + \mathbf{f}_{\mathrm{AD}}$, where $\mathbf{f}_{\mathrm{J}_2}$ is due to the Earth's oblateness and $\mathbf{f}_{\mathrm{S}}$ is induced by solar radiation pressure. Another force is the atmospheric drag $\mathbf{f}_{\mathrm{AD}}$, which is more critical for satellites in lower Earth orbits where atmosphere is denser in range below the mesosphere, thus it will not cause significant effect in the upper atmosphere including the exosphere discussed in this work.

In particular, the force caused by the J_2 effect per unit mass is expressed as

$$\mathbf{f}_{\mathrm{J}_2} = \frac{3\mu \mathrm{J}_2 R_e^2}{2r^5}\left[\left(\frac{5\left(\mathbf{r}\cdot\mathbf{z}_{\mathrm{G}}\right)^2 - r^2}{r^2}\right)\mathbf{r} - 2\left(\mathbf{r}\cdot\mathbf{z}_{\mathrm{G}}\right)\mathbf{z}_{\mathrm{G}}\right], \tag{5.8}$$

where $R_e = 6,378$ km is the equatorial radius, J_2 is the second zonal gravitational harmonic with a constant value of 1.08265×10^{-3} at Earth's equator [115]. Mathematically, it is the second moment in the Legendre polynomial to describe the Earth's gravitational field and is greater than other higher-order moments.

Solar radiation pressure

The solar radiation pressure-induced force is expressed as

$$\begin{aligned}\mathbf{F}_{\mathrm{S}} = \int_{\mathrm{S}_\odot} d\mathbf{f}_{\mathrm{S}} &= \int_{\mathrm{S}_\odot} -P_\odot c_{\mathrm{R}} \cos\varsigma ds\mathbf{e} \\ &= -P_\odot c_{\mathrm{R}}\mathbf{e}\int_{\mathrm{S}_\odot} \mathbf{n}\cdot\mathbf{e}ds,\end{aligned} \tag{5.9}$$

where $P_\odot$ is the solar pressure on the unit surface of satellite facing the Sun with a magnitude of 4.5×10^{-6} N/m^2, c_{R} the coefficient for solar radiation pressure in a range between 0 and 2, usually a fixed value of 1 is used in orbit calculation. $\mathrm{S}_\odot$ the area of satellite

facing the Sun, and $\mathbf{e}$ the unit vector pointing towards the satellite from the Sun. The maximum magnitude of force occurs when satellite and the Sun are aligned with Earth, where $\mathbf{n} \cdot \mathbf{e} = |\mathbf{n}||\mathbf{e}|$ where $\cos \varsigma = 1$.

For satellites, the area-to-mass ratio AMR is a useful parameter to quantify solar radiation pressure on space objects and determine corresponding orbit perturbation. For small satellites, the AMR value is usually smaller than $1\ \mathrm{m}^2/\mathrm{kg}$ while satellites with large solar panels expanded have larger AMR values. The perturbation force per unit mass induced by solar radiation pressure can be thus approximated as

$$\mathbf{f}_{\mathrm{S}_\odot} \approx -P_\odot c_\mathrm{R} \mathrm{AMR} \mathbf{e}. \tag{5.10}$$

Therefore, based on the effect from individual external perturbation forces, we have the following lemma to quantify the beam misalignment for a pair of small satellites during formation flying.

Lemma. *The relative secular motion of a pair of satellites is bounded when the pair is in the same circular orbit during formation flying. The beam misalignment angles in roll and pitch can be modeled as following a wrapped Gaussian distribution with corresponding mean and variance values, expressed as* $\vartheta \sim \mathcal{WN}\left(\bar{\vartheta}, 1 - e^{-\sigma^2/2}\right)$.

Proof. See Appendix. □

Based on the initial state and velocity of the Envisat satellite and parameters in Table 5.2, the cumulative distribution function (CDF) of beam misalignment is shown in Figure 5.6. It is observed that the angles follow a wrapped Gaussian distribution with different statistics, due to the external forces exerted on satellites.

5.4 THz Communications in TeraSpace Networks

Based on the characterized ISL channel in section 5.2 and developed orbit perturbation model in section 5.3, we are able to perform the channel modeling and performance esti-

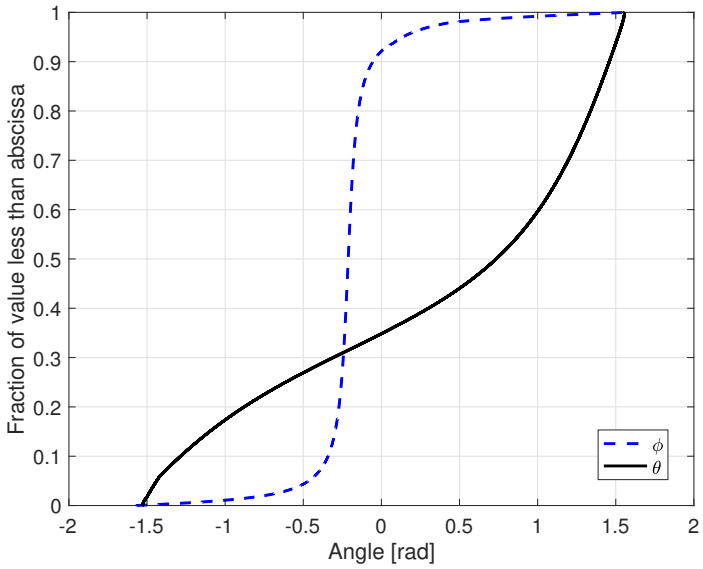

Figure 5.6: The CDF plot of the angular drift in relative motion in a circular orbit period.

Table 5.2: Fixed orbital-related parameters of a sample satellite

Parameter	**Value**
Solar radiation coefficient C_R	1.0
Satellite's effect area for solar radiation [m^2]	110.5
Satellite's mass [kg]	8000

mation at THz band ISLs in both near-Earth and deep-space scenarios. In this section, we analyze the link performance with respect to its achievable spectral efficiency.

5.4.1 Channel model with polarization and frequency diversity

A main factor which affects the THz band ISL performance is the free-space path loss, which necessitates high power gains generated by large-scale antenna arrays for compensation. Such antenna arrays can provide diversity gains from beam polarization, presuming appropriate configuration for each antenna element[4]. Such a polarization-diverse channel is illustrated in Figure 5.7, where we assume multiple polarization states can be deployed, including linear, slanted $\pm 45^o$, or circular polarizations. For a satellite transmitter with a

[4]Spatial diversity is not guaranteed due to the small form factor of distributed array placement and the lack of rich scatterers in channel, especially in deep space.

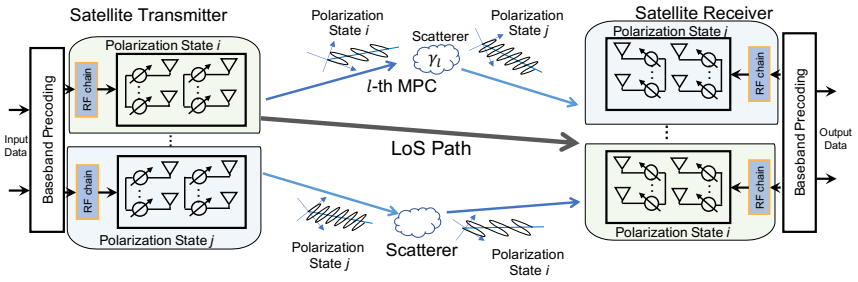

Figure 5.7: Illustration of satellite link with signal depolarization caused by scattering. The two polarization states are orthogonal to each other, which can be vertical and horizontal linear polarization, slanted $\pm 45^o$ polarization, or circular polarization.

planar array of N_t total antenna elements, $N_{\mathrm{RF}} < N_t$ RF chains are assumed with N_p polarization states ($2 \leq N_p \leq N_{\mathrm{RF}}$). The satellite receiver has N_r antenna elements with a total number of N_{RF} RF chains equal to the number of polarization states ($N_{\mathrm{RF}} \leq N_r$). The multi-polarized antennas are co-located, which evenly divide the total number of antenna element for each polarization state. Such co-located multi-polarized antenna structure can fit in a small form factor without spatial correlation due to their orthogonality [116]. In addition to the potential diversity gain that multi-polarization transmission brings, it is especially suitable for circumstance of an off-axis orientation of beams, due to possible attitude control error.

Additionally, given the large amount of spectrum resource available at THz band, it is preferable to divide the whole bandwidth into several non-overlapping subbands. Each ISL can be assigned or actively sense an idle subband for their usage. Thus, such frequency diversity can further improve spectral efficiency. This design with polarization and frequency diversity is illustrated in Figure 5.8, where a total of N_p polarization states are considered, each of which occupies a bandwidth of $\mathrm{B}_{\mathrm{N}_f}$. The whole bandwidth is further divided into several subbands, each with a bandwith of B_{SC}. From the perspective of system and signal processing complexity, since the technique of frequency diversity has been widely applied in the Ka-band satellites [117] and the polarization diversity concerns only the antenna array design which is also mature in commercial RF (sub-6 GHz and millimeter wave)

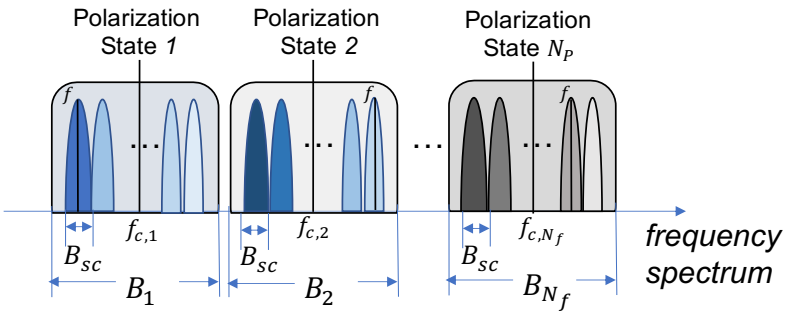

Figure 5.8: Illustration of transmitted signal with polarization and frequency diversity. The polarization states are orthogonal to each other with $N_p \geq 2$.

transceiver products, signals with a polarization will not be picked up by an orthogonally polarized antenna.

In the time-space channels, the LoS path usually preserves its polarization state while reflected/scattered multipaths can be depolarized to a different state, as illustrated in Figure 5.7. The fading process for different polarization states is independent; however, due to the presence of a direct path, the large-scale fading across polarization and frequency diversity follows a Rician distribution, where the ultra-wideband channel $\mathbf{H} \in \mathcal{C}^{N_r \times N_t \times N_f}$ is a three-dimensional matrix across different frequency bands, each sub-band within which can be written as the sum of the channel consisting of the deterministic LoS path $\mathbf{H}_{\text{LoS}} \in \mathcal{C}^{N_r \times N_t}$ and the one with all multipath components (MPCs) from reflection and scattering $\mathbf{H}_{\text{NLoS}} \in \mathcal{C}^{N_r \times N_t}$,

$$\mathbf{H}_f = \sqrt{\frac{\kappa}{1+\kappa}}\mathbf{H}_{\text{LoS},f} + \sqrt{\frac{1}{1+\kappa}}\mathbf{H}_{\text{NLoS},f}, \tag{5.11}$$

where f denotes the central frequency of the subband with a bandwidth of B_{SC} with flat-fading, κ is the Rician K-factor, which is the ratio between the power of the direct path and the sum of all MPCs. In an ISL in space, the multipath channel $\mathbf{H}_{\text{NLoS}}$ can be further expressed in a multi-polarized format, in order to reflect possible alternation across different polarization states. In the most common case where two orthogonal linear polarization states are adopted, which are vertical and horizontal polarization, the channel matrix for

MPCs can be expressed as

$$\mathbf{H}_{\mathrm{NLoS},f} = \begin{bmatrix} \mathbf{H}_f^{\mathrm{VV}} & \mathbf{H}_f^{\mathrm{VH}} \\ \mathbf{H}_f^{\mathrm{HV}} & \mathbf{H}_f^{\mathrm{HH}} \end{bmatrix}. \tag{5.12}$$

At the receiver side, the received signal $\mathbf{y}$ can be expressed as

$$\mathbf{y}_f = \mathbf{H}_f \mathbf{W}_f \mathbf{s} + \mathbf{n}, \tag{5.13}$$

where $\mathbf{W}_f \in \mathbb{C}^{N_t \times N_s}$ is the precoding matrix of the planar antenna array, $\mathbf{s} \in \mathbb{C}^{N_s \times 1}$ is the modulated transmit signal, and $\mathbf{n} \sim \mathcal{N}_c(0, \sigma^2 \mathbf{I}_{\mathrm{N}_r})$ the additive complex white Gaussian noise with zero mean. Each entry in $\mathbf{H}_{\mathrm{NLoS},f}$ can be further expressed as

$$\mathbf{H}_f^{\mathrm{VV}} = \sqrt{\frac{N_r N_t}{4L}} \sum_{l=1}^{L} \alpha_l(f) \mathbf{a}_{\mathrm{R,V}} \left(\hat{\theta}_{\mathrm{R},l}, \hat{\phi}_{\mathrm{R},l} \right) \mathbf{a}_{\mathrm{T,V}}^* \left(\theta_{\mathrm{T},l}, \phi_{\mathrm{T},l} \right), \tag{5.14a}$$

$$\mathbf{H}_f^{\mathrm{HH}} = \sqrt{\frac{N_r N_t}{4L}} \sum_{l=1}^{L} \alpha_l(f) \mathbf{a}_{\mathrm{R,H}} \left(\hat{\theta}_{\mathrm{R},l}, \hat{\phi}_{\mathrm{R},l} \right) \mathbf{a}_{\mathrm{T,H}}^* \left(\theta_{\mathrm{T},l}, \phi_{\mathrm{T},l} \right), \tag{5.14b}$$

$$\mathbf{H}_f^{\mathrm{VH}} = \sqrt{\frac{N_r N_t}{4L}} \sum_{l=1}^{L} \alpha'_l(f) \mathbf{a}_{\mathrm{R,V}} \left(\hat{\theta}_{\mathrm{R},l}, \hat{\phi}_{\mathrm{R},l} \right) \mathbf{a}_{\mathrm{T,H}}^* \left(\theta_{\mathrm{T},l}, \phi_{\mathrm{T},l} \right), \tag{5.14c}$$

$$\mathbf{H}_f^{\mathrm{HV}} = \sqrt{\frac{N_r N_t}{4L}} \sum_{l=1}^{L} \alpha'_l(f) \mathbf{a}_{\mathrm{R,H}} \left(\hat{\theta}_{\mathrm{R},l}, \hat{\phi}_{\mathrm{R},l} \right) \mathbf{a}_{\mathrm{T,V}}^* \left(\theta_{\mathrm{T},l}, \phi_{\mathrm{T},l} \right), \tag{5.14d}$$

where L is the number of resolvable MPCs in the environment, $\alpha_l(f)$ is the complex path gain of the l-th MPC depending on the center frequency of the deployed subband, $\alpha'_l = \alpha_l / \sqrt{\gamma_l}$, γ_l denotes the energy loss in depolarization (i.e., the cross-polarization ratio) of the l-th MPC, $\mathbf{a}_{\mathrm{R,V/H}}$ and $\mathbf{a}_{\mathrm{T,V/H}}$ denote the antenna arrays' responses with respect to the l-th MPC at Rx and Tx under the corresponding polarization states, respectively. $\theta_{\mathrm{T},l} \in [-\pi/2, \pi/2]$ and $\phi_{\mathrm{T},l} \in [-\pi, \pi]$ denote the l-th path's angle of departure in elevation (EoD) and azimuth (AoD), respectively. Due to the relative movement of satellites, $\hat{\theta}$ and $\hat{\phi}$ are used to denoted the actual angle of arrival in elevation (EoA) and azimuth (AoA)

Table 5.3: Parameters in simulations

Symbol	Parameter	Value
N_t	Number of antenna elements at Tx	12×10
N_{RF}	Number of RF chains at Tx and Rx	4
N_r	Number of antenna elements at Rx	6×4
G_{ele}	Gain of individual antenna element	3.2 dBi
N_{P}	Number of polarization states	2 and 3
B_{sc}	Bandwidth of one sub-band	500 MHz
P_{t}	Transmitted power at Tx	10 dBW
γ	Cross-polarization ratio	10 dB
κ	Rician K-factor	15 dB
T	Ambient noise temperature in LEO	283.32 K
T_{cmb}	Deep space cosmic microwave background noise	2.73 K
d	Antenna element spacing	$\lambda/2$
L	Number of multipath components	3

of signals which are taken as random variables from a wrapped Gaussian distribution based on the theoretical angles off scattering, with the relations that $\hat{\theta} = \theta + \vartheta$, $\hat{\phi} = \phi + \varphi$, where ϑ and φ are taken from the wrapped Gaussian distribution in Figure 5.6. In the planar antenna arrays, each element response encompasses phases from both elevation and azimuth angles, denoted as θ_l and ϕ_l, respectively. Hence, an individual element $\mathbf{a}_{\mathrm{R}}\left(\theta_{\mathrm{R},l}, \phi_{\mathrm{R},l}\right)$ at the receiver has a response of

$$a_{\mathrm{R}} = \frac{2}{N_r} \exp\left(\frac{jd2\pi}{\lambda}\left(n_y \sin\hat{\theta}_{\mathrm{R},l} \cos\hat{\phi}_{\mathrm{R},l} + n_z \cos\hat{\theta}_{\mathrm{R},l}\right)\right), \tag{5.15}$$

where $d = \lambda/2$ is the element spacing and equals half signal wavelength to avoid grating lobes, n_y and n_z ($\mathbb{Z} \in [0, \sqrt{N_r/2} - 1]$) denote the indices of element along the y and z axis in the LVLH frame.

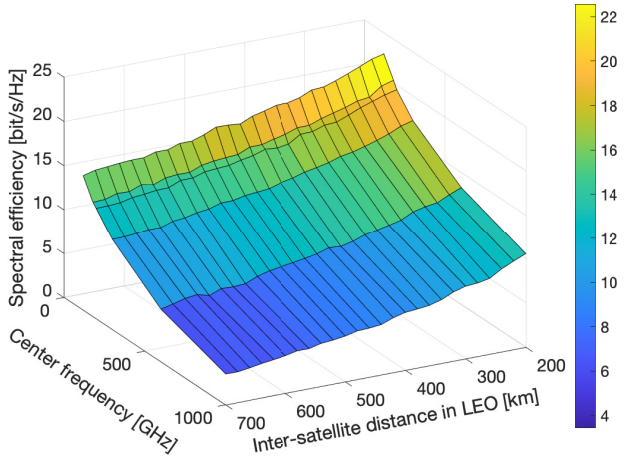

(a) Simulation results on achievable throughput in LEO with 10 dBW transmitted power.

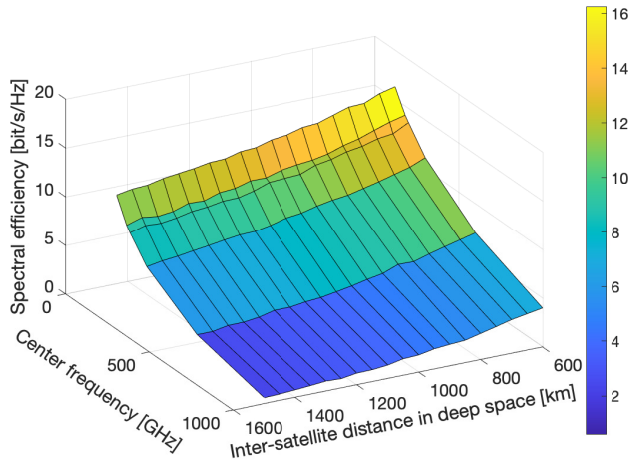

(b) Simulation results on achievable throughput in deep space with 10 dBW transmitted power.

Figure 5.9: Link performance results under near-Earth and deep-space link scenarios.

5.4.2 Link Performance Analysis

We focus on the link spectral efficiency, one of the most critical figures of merit to evaluate ISL performance. The choice of frequency and bandwidth will affect the resultant maximum achievable throughput, while channel perturbation cause errors in reception. The main parameters and their values are shown in Table 5.3.

In the proposed channel model, the achievable spectral efficiency can be expressed us-

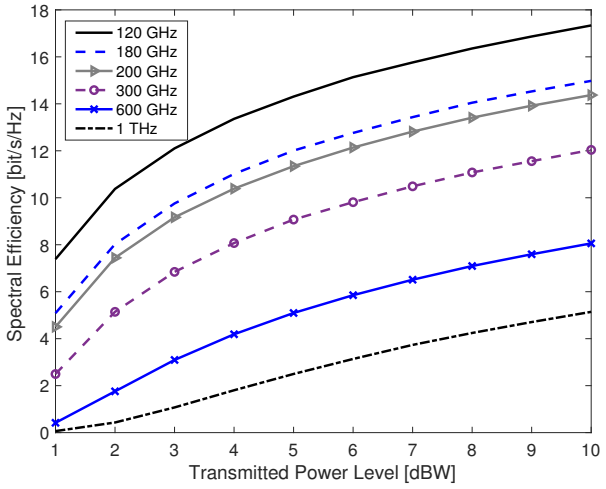

(a) Simulation results on achievable throughput in LEO with a fixed ISL distance of 500 km.

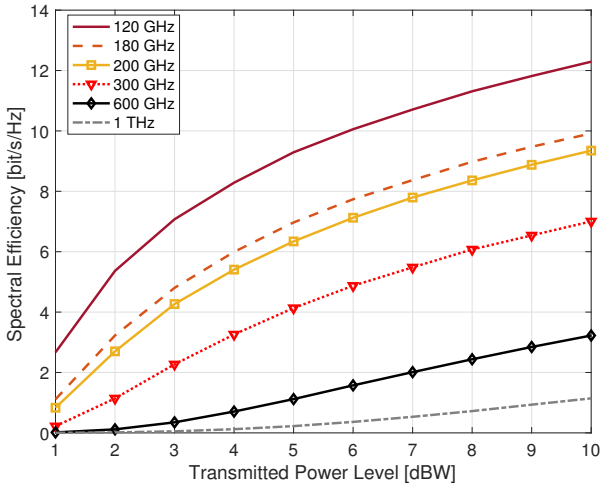

(b) Simulation results on achievable throughput in deep space with a fixed ISL distance of 1200 km.

Figure 5.10: Simulated spectral efficiency results with fixed link distances under near-Earth and deep-space link scenarios.

ing the Shannon capacity under MIMO channel across polarization and frequency diversity as

$$\Gamma = \log_2 \det \left(\mathbf{I}_{\mathrm{N}_r} + \frac{1}{\sigma^2} \mathbf{H}\mathbf{W}\mathbf{W}^*\mathbf{H}^* \right). \tag{5.16}$$

We assume that during beam pointing and acquisition stage, the channel state information is known by the transmitter satellite, such that W can be optimized through maximum

ratio transmission. We simulated the ISL at the following frequency bands: 120, 180, 200, 300, 600, and 1000 GHz, each with a bandwidth of 10 GHz. Such bandwidth is further equally divided into 20 subbands, each with 500 MHz. For the near-Earth ISLs, due to the proximity in formation flying satellites, we set the inter-satellite distance in a range of $[200, 700]$ km, while in deep space, the distance range is $[600, 1500]$ km. The spectral efficiency results are shown in Figure 5.9.

It is observed that when the transmitted power is fixed at 10 dBW, which is the maximum power level for a CubeSat, the spectral efficiency can achieve a peak of around 22 bits/s/Hz at 200 km at 120 GHz for near-Earth ISL, while a similar peak is shown at 700 km at the same frequency with a value of 16 bits/s/Hz in deep-space ISL. Furthermore, when the ISL distance is fixed during formation flying, we can analyze the performance under different power levels. As shown in Figure 5.10, it is shown that when two small satellites have a link distance of 500 km, a 17.2 bits/s/Hz can be achieved at a single subband of 500 MHz when a maximum transmit power is set, leading to a 172 Gbps throughput at 120 GHz. Even with half the maximum power at 300 GHz, a throughput of 80 Gbps provides a promising prospect for utilizing small satellites to achieve high-speed inter-satellite links for future communications.

5.5 Summary

In this chapter, a design for small satellite communication network at THz band for both near-Earth and deep-space links is presented. We first describe the effects of Earth's upper atmosphere and solar activities with respect to communications in the THz spectrum. In particular, we show that even though ionized particles are active in the ionosphere, no significant impact will be cast on THz links, making THz band a feasible carrier for near-Earth links. Furthermore, for deep-space links, only severe solar activities can cause angular instability at THz band. We further analyze the orbit perturbation caused by various factors in space and propose a model characterizing such effects. Finally, based on the character-

ization of space channels, we present a link-level analysis for diversity-based TeraSpace channel. In particular, we demonstrate the spectral efficiency over various THz frequency bands and link distances. Simulation results show that with the TeraSpace link can achieve a maximum throughput of 172 Gbps at 120 GHz, proving a promising space communication application using the THz band.

CHAPTER 6
MULTI-BAND CUBESAT DESIGN IN SATELLITE COMMUNICATION NETWORKS

6.1 Motivation and Related Work

The commercial use of space requires the development of reliable and economic solutions to serve various applications including sensing, imaging, navigation, and communication, among others. Such services are currently supported by traditional satellites in Low Earth Orbits (LEOs), Medium Earth Orbits (MEOs) and Geosynchronous Equatorial Orbits (GEOs). Nevertheless, existing satellites have several major drawbacks. First, the very high costs associated with the design, construction, launch, and operation of traditional satellites and satellite networks result in a very high entry barrier for new operators and vendors. For example, the cost of developing and deploying the Iridium Next system is expected to exceed $3 billion. Consequently, the use of satellites has been restricted to a few major players. In addition, traditional satellites have very long development cycles, which can range from three years for commercial ventures to ten or more years for government initiatives. Moreover, traditional satellite programs do not make use of sequential redundancy [118], i.e., a new development program is usually started only after the previous program has been fully deployed, making it difficult to adapt to the rapidly changing market needs.

Recognizing those deficiencies, the satellite landscape has witnessed the emergence of a new class of miniaturized satellites known as CubeSats. Originally envisioned for university education and research purposes, CubeSats are seen as a promising solution to realize global satellite networks at much lower costs [119]. In addition, the short timeframe from development to operation makes CubeSats an efficient deployment option, very different

from traditional satellite networks. CubeSats have uniform cubic sizes of payload systems denoted as 1U, 2U, etc., where "U" means a cube with a dimension of $10 \times 10 \times 10$ cm^3, and can be used for applications in numerous research fields including biochemistry, astrophysics, and telecommunications [120].

Recently, several commercial solution providers have targeted CubeSats to serve in LEOs to provide services including Earth remote sensing, weather forecasting, and machine-to-machine communication, as shown in Table 6.1 on the following page. For instance, Planet Labs has recently launched a total of 175 CubeSats named "Doves" to support high-resolution Earth imaging services[1]. CubeSats are also deployed in deep space for missions including interplanetary data relaying, sensing and monitoring on the Moon, Mars, and several asteroids, as well as even further in deep space. For example, the Mars Cube One (MarCO) mission from NASA consists of a pair of CubeSats aimed at the exploration of Mars. The pair, MarCO-A and MarCO-B, was successfully launched in May 2018 and planned to fly by Mars in November 2018[2]. In the range of small satellites, which are larger than CubeSats but still significantly smaller than traditional satellites, the Starlink constellation developed by SpaceX has planned to provide satellite Internet service with global coverage[3]. It is foreseeable that more promising CubeSat and small satellite missions will be enabled with future advancements in physics, electronics, and telecommunications.

With the proliferation of CubeSat-enabled applications and, subsequently, the increase in the number CubeSats in different orbits, there has been an exponential increase in the use of the space communication frequency spectrum [121].

[1] https://www.nasaspaceflight.com/2018/01/planet-labs-targets-search-engine-world/
[2] https://www.jpl.nasa.gov/cubesat/missions/marco.php
[3] https://www.starlink.com/

Table 6.1: Existing or Planned CubeSats-based Satellite Services

Name of CubeSat	**Iridium NEXT SensorPoD**	**Dove**	**MarCO**	**Astrocast**	**Fleet**	**KIPP**	**AISTECHSAT**
Company/Agency, Country	Iridium Communications, U.S.	Planet Labs, U.S.	NASA, U.S.	ELSE, Switzerland	Fleet, Australia	Kepler, Canada	Aistech, Spain
Purpose	Sensing and communication	Earth imaging	Mars exploration	IoT and M2M	IoT	Satellite backhaul	IoT, M2M, asset tracking
ISL Capability	Only to the host Iridium NEXT satellites	No	No	Yes	n/a	n/a	n/a
Year of First Launch	2015	2015	2018	2018	2018	2018	2018
Orbit Altitude	780 km	420 and 475 km	n/a	n/a	580 km	n/a	n/a
Number of CubeSats in Constellation	66	175	2	64	100	140	100
Form Factor	4.5U	3U	6U	n/a	3U + 12U	3U	6U
Weight	4–5 kg	5.8 kg	14 kg	n/a	n/a	n/a	n/a
Frequency	Ku-band	X-band	X-band	L-band	n/a	Ku-band	n/a
Self-sustained	No	Yes	Yes	Yes	Yes	Yes	Yes

Note: "n/a" means the parameter is not available in published sources.

Communication between satellites is needed both to enable the exchange of control and data information between CubeSats as well as to realize a globally connected network with ground infrastructure. Currently, conventional satellite networks as well as recently-deployed CubeSat networks rely on the use of specific frequency sub-bands within the authorized spectrums regulated by the Federal Communications Commission (FCC) under 47 CFR 97.207 and regulatory framework of the International Telecommunications Union (ITU). Traditionally, the use of higher frequency bands has been discouraged due to their much higher path loss and, thus, shorter transmission distance between satellites, which would have required the deployment of denser satellite constellations. Nevertheless, the much lower cost and development timeline of CubeSats open the door to considering higher frequency bands for communication, including the millimeter wave (mmWave) (30–300 GHz) and the Terahertz (THz) bands (0.1–10 THz) as well as the infra-red and visible spectral bands (200–400 THz). Ultimately, efficient techniques for spectrum access, management, and sharing are needed to support the next generation satellite services.

In this chapter, we propose an initial CubeSat design able to support multi-band wireless communication at microwaves, mmWave, THz band and optical frequencies. Multi-band communication is needed for CubeSats to meet the throughput requirements for inter-satellite data-intensive applications. In our proposed architecture, CubeSats with altitudes between 500 and 900 km above the Earth ground can transmit, receive, and store data with high throughput in a global coverage constellation. This architecture can significantly leverage the capabilities of current CubeSat networks, and will be fundamental for future interplanetary CubeSat networks. We envision that the CubeSat networks will conceive the "*Internet of Space Things* (IoST)", a paradigm-shift architecture to leverage the cyber-physical system with another degree of freedom in the space for global process control and optimization.

The novelties of our architecture include:

1. Multi-band radios covering wide spectrums at microwaves, mmWave, THz band, and

optical frequencies to accommodate high-throughput services. The key enabling device technologies include (i) a hybrid integration of two complementary signal generation, modulation, detection and demodulation approaches, namely, an electronics-based approach and a photonics-based approach, and (ii) an enhancement and exploitation of the intermediate products and harmonics generated in the process of frequency up- and down-conversion;

2. Foldable multi-band antenna arrays based on new materials such as graphene, which allow the creation of programmable antenna architectures with tunable frequency and radiation diagram. The frequency and space beamforming capabilities of such arrays are dynamically exploited to accommodate different communication requirements;

3. Deep-neural-networks-enabled resource allocation strategies for self-learning and optimization of CubeSat networks to adaptively determine the optimal combination of specific frequency channel, transmit power, antenna gain, modulation and coding scheme, among others.

In the rest of this chapter, after introducing the existing CubeSat architecture in section 6.2, in section 6.3, we describe the multi-band communication technology for the next generation CubeSats, including innovative transceivers and antennas. Then, we describe the communication aspects between CubeSats as well as between CubeSats and ground devices, including types of links, physical and link layers solutions, and open research challenges, in section 6.4.

6.2 CubeSat Architecture and Subsystems

The design of a CubeSat follows standards based on the research collaborations among universities and research labs, which guarantees the unification among payloads and launchers and optimize the capabilities of miniaturized payloads [122]. According to the specifications set by NASA, CubeSats cannot contain any propulsion systems, hence they can only

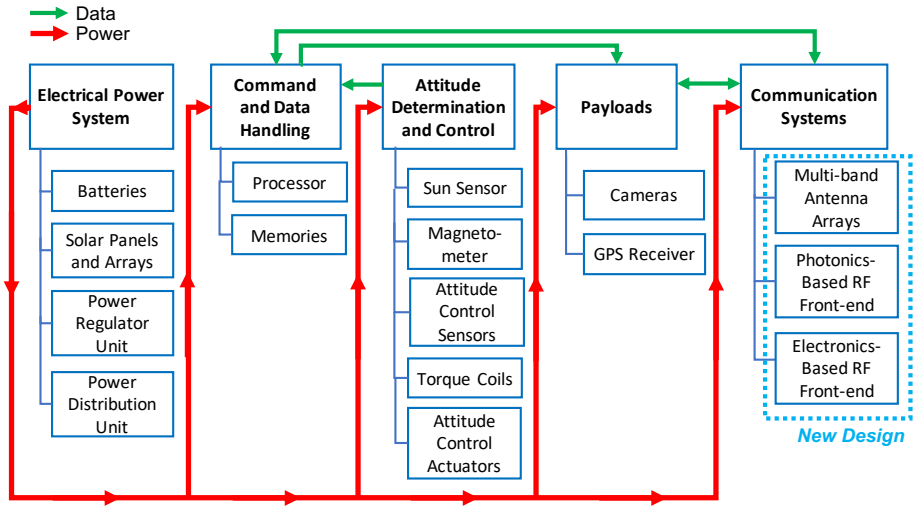

Figure 6.1: Basic functional components of next-generation CubeSats.

be deployed to the target orbit as secondary payloads via an airborne launch system in a rocket (e.g., SpaceX's Falcon rockets) or from the International Space Station (ISS) [123]. In both cases, the deployment stage is carried out through a poly-picosatellite orbital deployer (P-POD) system[4], which currently supports CubeSats of size up to 3U. In the next subsections, we describe the main components in current CubeSat architectures, which are summarized in Figure 6.1.

6.2.1 Electrical Power System

The electrical power system (EPS) serves as the energy source to perform all necessary sensing, processing, and communication tasks. It includes subsystems to perform energy conversion, power regulation and control, energy storage, and distribution [124]. The major energy source is the Sun and, thus, solar panels and high-capacity batteries are utilized to provide highest efficiency even when the CubeSat is not covered by sunlight. The EPS includes the follow components:

- **Batteries**: The batteries in existing CubeSats commonly use lithium polymer cells with a nominal voltage level of 5V with high energy densities and a robust protection

[4]https://www.nasa.gov/pdf/506741main_ppod508.pdf

architecture according to the standard. The batteries also provide extra protection against overcharge, over-discharge, over-current, over-voltage, and over-temperature.

- **Solar Panels and Arrays**: State-of-the-art solar panels generally consists of III-V semiconductor-based solar cells, such as Gallium Arsenide (GaAs) triple junction solar cells, temperature sensors, and Sun sensors. Before the on-orbit deployment, the solar panels are folded inside the launch vehicle. Once in orbit, the solar panels are expanded to conduct energy harvesting, temperature sensing, and other tasks.

6.2.2 Command and Data Handling

The purpose of the command and data handling (C&DH) board is to command the subsystems of CubeSats. The subsystems include performing Earth imaging operations, commanding radio to beacon, transmitting data, receiving commands and data, changing configurations, and commanding EPS to power on or off. The C&DH consists of two processing units. The processing core of the C&DH interprets control commands and schedules actions, whereas small form-factor, low power-consumption micro-controllers are responsible for communicating with the CubeSat's other subsystems.

6.2.3 Attitude Determination and Control System

Another crucial system inside a CubeSat is the attitude determination and control system (ADCS), which guarantees the stability of payloads, manages the position and pointing accuracy of antennas, and assists optical control to provide fine pointing. It contains several sensors, actuators, and magnetometers to measure the magnetic field near orbit [125].

6.2.4 Payloads

There is a plethora of payloads that a CubeSat can incorporate. The most advanced systems include multi-frequency (infra-red, visible, ultra-violet) orthophoto cameras which are capable of capturing imagery at a resolution of 10–15-m ground sample distance, telescopes

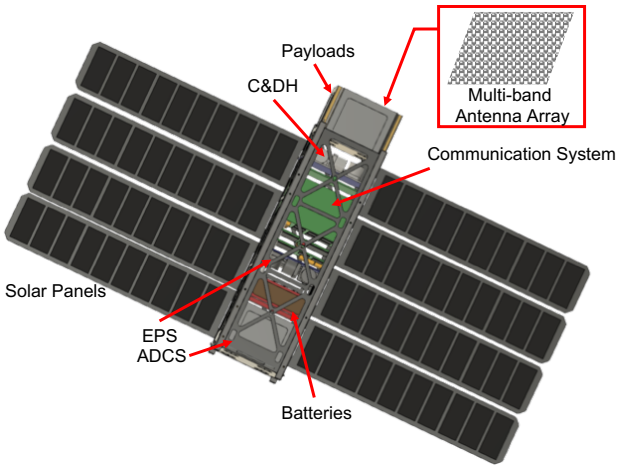

Figure 6.2: Preliminary design of a next-generation 3U CubeSat with solar panels expanded and basic functional components indicated by arrows.

that can observe from surrounding satellites to deep space objects, and a series of sensors for space environment monitoring such as temperature and gas concentration among others. The image sensing capability equipped on CubeSats can reach a radiometric resolution of 16 bits with a spatial granularity or positional accuracy of less than 10 m root mean square error[5].

6.2.5 Communication System

Currently, CubeSats have limited communication capabilities to ground infrastructure. The available frequency bands for communication are the S-band (2–4 GHz), C-band (4–8 GHz), X-band (8–12 GHz), Ku-band (12–18 GHz), and Ka-band (26.5–40 GHz). These frequency bands are also being heavily utilized by other satellite communication and links between space shuttles and the ISS, as well as terrestrial wireless networks including IEEE 802.11 series, which can cause severe interference and thus degrade system performance. In the next section, we present the new communication architecture for our CubeSat design.

[5]https://www.planet.com/products/satellite-imagery/files/Planet_Combined_Imagery_Product_Specs_December2017.pdf

6.3 Proposed Design for Next-Generation CubeSats

Our proposed design of next-generation CubeSats incorporates multi-frequency transceivers and antenna arrays needed to support high-throughput inter-satellite links needed in CubeSat-enabled satellite applications. In order to meet the requirements of future CubeSat use cases and accommodate necessary subsystems and payloads, we propose a CubeSat with the dimension of 3U (10 cm $\times$ 10 cm $\times$ 34 cm) and a maximum weight of 5 kg, as illustrated in Figure 6.2. This design allows the antenna arrays to be stowed during launch and pre-deployment.

6.3.1 Multi-frequency Transceiver Design from RF to THz Bands to Optical Frequencies

To overcome the spectrum scarcity and capacity limitations in current satellite networks, we propose the utilization of multiple frequency bands, from RF to THz, and to optical frequencies, for next-generation CubeSat communication systems. For this, frequency-agile ultra-broadband reconfigurable systems able to communicate over the broad electromagnetic (EM) spectrum ranging from hundreds of MHz up to optical frequencies need to be developed. Between the two ends of the spectrum, the mmWave and, especially, the THz-band frequencies provide new opportunities for high-speed wireless communications. Due to recent major progress in device development at these frequencies [126, 13], it is possible to enable communication at such high frequency bands. While molecular absorption by oxygen and water vapor at mmWave and THz-band cause heavy attenuation to signals on the ground, such effect is negligible in space because of the very low concentration of absorbing molecules above the atmosphere.

Millimeter-wave and THz-band communication exhibit several key advantages over RF communications:

- Owing to the very large available bandwidth at mmWave and THz frequencies, even very simple modulation and coding strategies can support from the start much higher

bit-rates than existing RF systems.

- Because of the small wavelength at mmWave and THz frequencies, the size of antenna arrays can be significantly reduced. More antenna elements can fit per unit area of the array, enabling new massive and ultra-massive MIMO communication schemes.

- Due to the directional propagation of mmWave and THz frequency waves, interference between satellites is potentially much lower than at RF frequencies.

It should be noted that the use of optical communications for satellite networks has also been proposed [127, 128]. Compared to optical frequencies, the mmWave and, specially, the THz-band, support similarly large transmission bandwidths, which are mainly limited not by the physics of the channel, but by the speed of the electronic and opto-electronic components. Moreover, the much narrower transmission beams in optical systems further increases the alignment requirements between the transmitting and receiving satellite. In light of these observations, the THz band (0.3–10 THz) seems to offer a compromise between RF (2–300 GHz) and optical bands (with typical bands of 850 nm/350 THz, 1300 nm/230 THz, and 1550 nm/193 THz).

In light of this proposed multi-frequency communication system, new transceiver architectures are needed. Three metrics weigh in the design of a reliable and efficient transceiver suitable to generate signals at various frequency bands for space communication and networking, namely, (i) dimension constraints, (ii) power source and energy consumption, and (iii) achievable performance. In particular, the dimension of the transceiver has to follow the standard specified in CubeSat architecture. Besides the aforementioned benefits of operating at mmWave and THz-band frequencies, one additional advantage of operating in space is the fact that devices can be naturally operating at a low temperature, without the need of cooling components or cryostats. This can further lead to compact communication systems for CubeSats.

We propose two parallel approaches to realize the proposed multi-band transceivers, namely, multi-stream electronic up-converting chains and optical down-converting chains.

Multi-stream Electronic Frequency Up-converting Chains

While direct-generation mmWave and THz sources have been envisioned [129, 21], currently, the most common option to generate mmWave and THz signals is through frequency multiplication and up-conversion [130, 131]. Conventionally, only the final up-converted signals are used as the output and the intermediate products are discarded. However, by taking advantage of these intermediate frequencies, we can leverage the up-conversion chain to generate multi-streams of signals to be fully utilized as carriers in the multi-band communication system. As illustrated in Figure 6.3, the general idea is to use frequency splitters after frequency multipliers in order to extract the intermediate frequencies for outputs. The signal at frequency f_1 is considered as the intermediate output when producing signals at a higher frequency f_2. Similar structures can be cascaded to provide more output streams.

The main components of the electronic transceiver include *frequency multipliers, mixers, splitters, amplifiers, and filters*. The function of frequency multipliers, which are usually implemented as chains of frequency doublers or triplers, is to increase the frequency of the local oscillator (LO) to the desired radio frequency or to an intermediate frequency (IF). Mixers combine two input signals to generate the output at the sum of their frequencies. Frequency splitters divide the input signal into two identical output signals for further processing. Amplifiers enhance the amplitude of the input signal, while filters, including bandpass and high-pass filters, can eliminate unwanted harmonics to improve the spectrum efficiency. The proposed structure leverages the state of the art in RF, mmWave and THz transceivers, and can only benefit from further developments.

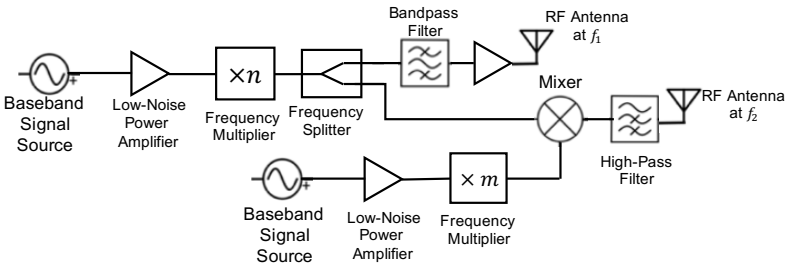

Figure 6.3: Block diagram of all-spectrum signal front-end by the electronics-based approach.

Photonics Frequency Down-conversion Chains

Besides RF up-conversion to mmWave/THz bands, an alternative approach exists where multi-band signals can be generated by down-converting optical signals. Such system can fit in the limited space in IoST CubeSats while providing satisfying multi-band signal generation. These recent research advances are enabled by photonics-based RF signal generation based on a silicon photonics chip [132, 133, 134]. The major components of the photonics-based approach include *a laser signal source* and *a Mach-Zehnder modulator*. With similar ideas of taking advantage of the multi-stream signals as in subsubsection 6.3.1, as shown in Figure 6.4, multi-band signals can be generated by the approach of heterodyning two input signals with a Mach-Zehnder modulator, thus producing an RF signal with a frequency equal to the difference between the two inputs as the final output, while maintaining the two input signals also as two output streams. With a tunable LO, multi-frequency band signals can be generated as the output [135]. Additionally, the stability of the photonics-based RF signals is directly dependent on the stability of the laser sources. Therefore, in the CubeSat design, mode-locked lasers are preferred to generate stable signal source [136]. Then a single-mode optical fiber is used to deliver the down-converted signal to the antenna side.

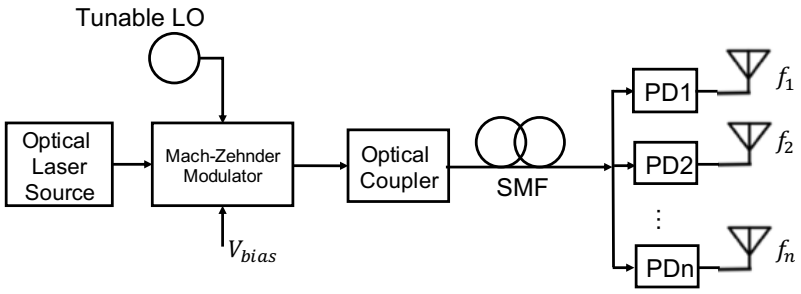

Figure 6.4: Block diagram of multi-frequency band front-end by the photonics-based approach.

6.3.2 Multi-Frequency Antenna Systems

In addition to the transceivers, multi-frequency antenna systems as well as very high gain directional antennas are needed to combat the very long transmission distances. While fixed directional antennas, such as horn antennas, mounted on mechanical steering systems, could be utilized, electronically-controlled phased antenna arrays are preferred due to their much higher flexibility. When moving to higher frequency bands, antennas become smaller and, thus, much denser antenna arrays can be built. Such very large antenna arrays are at basis of massive and ultra-massive MIMO communication schemes.

In order to create a multi-band antenna array, different technologies can be leveraged. On the one hand, *physically reconfigurable antennas* based on nano- or micro-electromechanical (NEMS/MEMS) or origami structures have been proposed as a way to physically change the size of the radiating elements and, thus, their resonant frequency [137, 138]. The main challenges with this approach are the delay associated to the control of the NEMS/MEMS systems, specially when targeting very high data-rates, as well as the size and integration complexity of NEMS for the THz-band antennas. On the other hand, new materials such as graphene can be leveraged to create *software-defined or electronically tunable nano-antennas* and *nano-antenna arrays* [2, 139]. Indeed, the resonant frequency of graphene-based plasmonic nano-antennas can be controlled by modulating the graphene Fermi energy or chemical potential. As a result, without physically changing the antenna

size, one antenna can be tuned to resonate at different bands. While graphene can be utilized for THz frequencies, other nanomaterials and metamaterials are needed to achieve a similar behavior at lower bands.

Besides transmit antenna arrays, reflector antenna arrays can be utilized to fit the multi-frequency CubeSat links. *Reflectarray antennas* have been widely utilized in radars, point-to-point links, and satellite communications because of their flexibility and low cost [53]. Based on principles of phased arrays and geometrical optics, electronically tunable reflector antenna arrays can realize dynamically adjustable radiation patterns. Specifically, the phase shift of each element in the array can be controlled electronically and will jointly form an array pattern to receive from or transmit to the signal desired directions. Compared to traditional phased arrays that require complicated phase shifter circuits and suffer from high transmission line loss at higher frequencies, reflector antenna arrays are simpler in mass production and have higher energy efficiency because there is no need for transmission lines, which make them suitable to be attached to CubeSats with limited dimensions. Moreover, we leverage the conventional design of reflectarrays to a series of foldable multi-band antenna arrays which can be attached to the body of CubeSats and expanded to larger sizes to achieve high gain, enhanced directivity, and high efficacy in multi-band operation. The operation of folding and expansion can be controlled adaptively given the requirements of communication tasks.

6.4 Multi-Band CubeSat Communications

The multi-frequency transceivers and antenna arrays architectures introduced in the previous section will enable innovative, faster, and more spectrum-efficient satellite communication systems. In this section, we conduct a link budget analysis and discuss the communication aspects at the physical and link layers of next generation CubeSat-enabled networks.

6.4.1 Inter-Satellite Links

Communication between CubeSats in orbit are enabled by ISLs, also known as "crosslinks". Analogous to terrestrial Internet backbone links, ISLs require very high capacity in order to be able to handle the aggregate data flows from ground devices as well as satellite data and, ultimately, reduce the total transmission time significantly. For this, we propose to utilize multiple mmWave and THz bands at 0.06, 0.12, 0.18, 0.3, 0.6, and 1 THz for ISLs. As discussed in subsection 6.3.1, the very low concentration of molecules in the exosphere eliminates the molecular absorption problem, which is one of the main bottlenecks for on-the-ground mmWave and THz-band communications.

To assess the feasibility and derive the gain requirements for CubeSats in ISLs, we conduct a link budget analysis. The antenna system used in our simulation is the reconfigurable reflectarray antenna discussed in subsection 6.3.2.We consider that the minimum bandwidth for communication is 500 MHz and the maximum transmitted power is 1 W (30 dBm). In the exosphere, since the temperature is a function of altitude and can vary greatly from a few degrees above absolute zero to thousand degrees in Kelvin, the noise level can also vary gigantically, hence we study a worst-case scenario with ambient temperature at 1500 Kelvin. In Figure 6.5 and Figure 6.6, we illustrate the minimum gain required and the maximum beamwidth allowable at the receiving CubeSat, respectively, to maintain a 10 dB Signal-to-Noise Ratio (SNR), for different frequency bands spanning from 60 GHz to 1 THz. From the simulation results, it is clear that higher gains are needed when increasing the transmission frequency, even in the absence of atmospheric losses. For the 500 MHz bandwidth, since the channel is symmetric, the gain at each transceiver end is always under 55 dB, which can be achievable with the antenna array technologies described in subsection 6.3.2. Increasing the channel bandwidth by an order of magnitude would increase the required gain by 10 dB. In designing the CubeSat constellation, the distance between CubeSats not only influences the coverage of the Earth's surface, but also affects the achievable data rates.

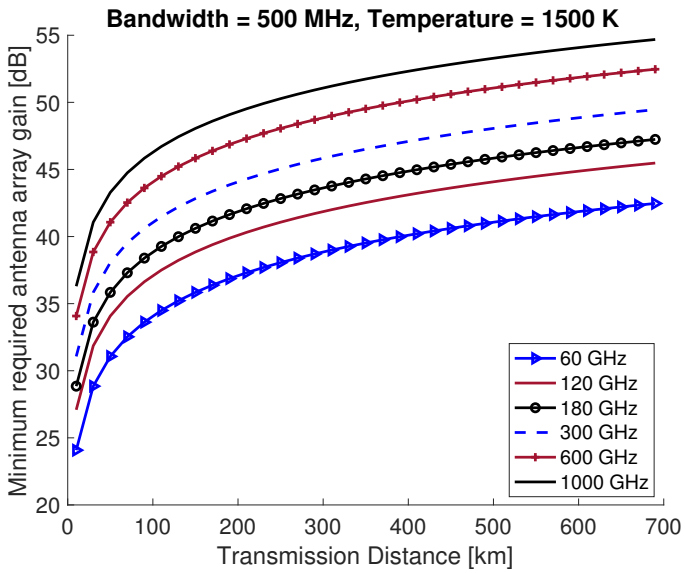

Figure 6.5: Minimum required gain at the receiver in ISLs to maintain a 10 dB SNR at several typical communication frequencies in IoST.

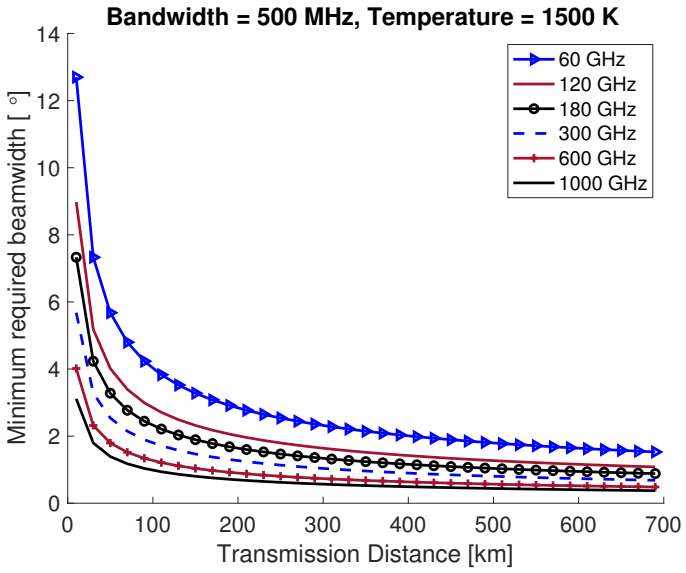

Figure 6.6: Maximum allowable beamwidth at the receiver in ISLs to maintain a 10 dB SNR at several typical communication frequencies in IoST.

The link power budget is critical for estimating the life expectancy of a spacecraft and determining the appropriate choice and assemble of electronic components and circuitry. In the near-Earth case, we use the reference from the Prisma satellite, where the maximum distance of formation flying between its main spacecraft and target is 30 km (a typical

mother-daughter architecture in small satellite formation flying). Our near-Earth case aims for an ISL with a distance of 453.33 km, representing a practical distance for future satellite formation flying strategy. In the deep-space case, we examine a deep-space relay link with a length of 906.022 km. In particular, the link design takes into account the effect of solar conjuction. As a reference, a data relay link for Mars is used based on the flight demonstration in [140]. The numerical results are shown in Table 6.2.

Table 6.2: A Comparison of Design Control Table

Parameter	**Unit**	**LEO Sample** [141]	**Our LEO Design**	**DS Sample** [140]	**Our DS Design**
Transmitter Parameters					
1. Transmitted Power	dBm	20	23.2	40.8	23.2
2. Transmitter Antenna Gain	dBi	0	45	-1.5	45
3. Waveguide and Antenna Pointing Loss	dB	-2	-2	-1.0	-2
4. EIRP (Sum of Items 1–3)	dBm	18	68.2	38.3	68.2
Path Parameters					
5. Free Space Path Loss	dB	-128.87	-185.57	-155.22	-191.59
6. Atmospheric Attenuation	dB	0	0	0	0
7. Cosmic Microwave Background Noise	K	0	2.73	0	2.73
Receiver Parameters					
8. Receiver Antenna Gain	dBi	0	10	-1.0	45
9. Antenna Pointing Loss	dB	0	-1	N/A	-2
10. System Loss	dB	-2	-2	-0.4	-2
Total Link Power Budget					
11. Total Received Power (Sum of Items 4–10)	dBm	-110.87	-113.1	-118.32	-85.12
12. Noise Spectral Density	dB/Hz	-200.96	-203.98	-201.6	-203.98
13. System Noise Temperature	K	580	290*	500	290*
14. Received pt/no	dBm Hz	90.09	90.88	83.28	118.86
15. Required pt/no	dBm Hz	N/A†	80.88	N/A	108.86
16. Performance Margin (Subtraction of Item 15 from 14)	dB	N/A†	10	N/A	10
Carrier Parameters					
17. Carrier Frequency	GHz	2.275	100	0.44	100
18. Modulation Type	–	QPSK	BPSK/QPSK	N/A	BPSK/QPSK
19. Carrier Bandwidth	MHz	8	500	N/A	500

* This is achievable using on-board cryogens.

† "N/A" means data not available in public literature.

6.4.2 Ground-to-Satellite Links

Compared to ISL among CubeSats in the exosphere, where the atmospheric attenuation can be negligible and the received signal strength follows the Friis' law, the ground-to-satellite link is more challenging and complicated. The signals from CubeSats to ground stations will go through at least 500 km long distances traversing the dense atmosphere, which will greatly attenuate the signal strength. Some previous research focuses on the study of the ground-to-satellite link at mmWave and THz band frequencies. The choice of ground station depends on the distribution of precipitable water vapor over the surface. It is shown that with optimal ground station locations, carrier bandwidths, and modulation schemes, the ground-to-satellite links at THz band can achieve 1 Tbps when fog, cloud, or air turbulence are absent [142]. The study also suggests to use airborne platform, such as small aircrafts or balloons, to forward signals from satellites to ground stations. However, deploying ground stations only at dry areas limits the potentials of ground-to-satellite link capacity. To solve this problem, at other locations where humidity is not suitable for THz link establishment, the lower bands can be used (e.g., the X-, Ku- and Ka- bands). These frequency bands can operate in environments where THz link might experience enormous atmospheric attenuation and molecular absorption.

In order to better utilize the available frequency resources and transmit the signals from CubeSats to ground stations, we propose *hybrid GSLs enabled by both microwave and mmWave/THz bands.* The fundamental idea is to use a pilot signal at microwave frequencies to detect the viability of a ground-to-satellite link. If certain criteria are met for data transmission (i.e., CubeSat in line-of-sight (LOS) with ground station, weather permissible, and ground station idle), the data will be transmitted to ground station in Field-of-View (FOV) of the CubeSat with a dedicated channel and an ultra-low latency. We envision the wide spectrum ranging from 3 GHz to 300 GHz can be utilized in GSL, because of the relatively smaller atmospheric and molecular attenuation rate compared to THz frequency bands through the Earth atmosphere. An exception occurs at 180 GHz with a noticeable

drop in maximum achievable data rate is caused by the molecular absorption with a water vapor density of $7.5\ \mathrm{g/m^3}$. For most frequency bands studied, in an environment with dry air and ambient temperature at 300 Kelvin (25°C), a data rate of 150 Gbps can be achieved at 300 GHz. Even with a water vapor density of $7.5\ \mathrm{g/m^3}$, the achievable data rates are on the Gbps-level.

6.4.3 Influence of Weather on CubeSat Multi-Band Links

In satellite communication scenarios, space and atmospheric weather has non-negligible effects on the survivability of GSLs [143]. Among them, rain fading plays a crucial role. According to the ITU's recommendation (Recommendation ITU-R P.838-3), it is demonstrated that the rain attenuation γ_R (in dB/km) is a function of the communication frequency f_c (in GHz), rain rate R (in mm/hr), and two polarization-specific coefficients, k and α, which form a relationship from curve fitting as follows,

$$\begin{aligned}\log \gamma_R &= \log k + \alpha \log R, \\ &= \sum_{j=1}^{4} \left(a_j \exp\left[-\left(\frac{\log f_c - b_j}{c_j} \right)^2 \right] \right) + m_k \log f_c \\ &+ c_k + \log R \left[\sum_{j=1}^{5} \left(a_j \exp\left[-\left(\frac{\log f_c - b_j}{c_j} \right)^2 \right] \right) \right. \\ &\left. + m_\alpha \log f_c + c_\alpha \right],\end{aligned} \tag{6.1}$$

in which a_j, b_j, c_j, m_k, and c_k are coefficients dependent on frequency and polarization conditions and are given in [144]. In particular,

$$k = \left[k_H + k_V + (k_H - k_V) \cos^2\theta \cos(2\tau) \right] / 2, \tag{6.2a}$$

$$\alpha = \left[k_H \alpha_H + k_V \alpha_V + (k_H \alpha_H - k_V \alpha_V) \cos^2\theta \cos(2\tau) \right] / \left(2k \right), \tag{6.2b}$$

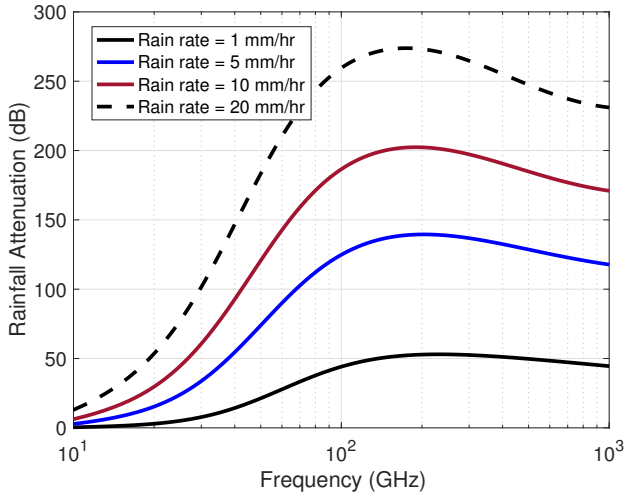

Figure 6.7: Path loss due to rainfall from 10 GHz to 1 THz with 500 km altitude.

where θ and τ are the elevation angle of the path and the polarization title angle with respect to the horizontal plane, respectively.

We can hence capture the attenuation caused by the water molecules at frequencies up to 1 THz in GSLs. When a ground station needs to connect to a CubeSat or vice versa, the power budget takes into account the rain fade at the intended frequency. As shown in Figure 6.7, the rain fading has a peak at around 175 GHz regardless of rain rate, making this spectrum not feasible for GSLs. For a moderate rainfall scenario with rain rate in a range of 0.5–4 mm/hr, the rainfall attenuation is lower than 94.67 dB at 77 GHz and 115.4 dB at 120 GHz.

6.4.4 Massive and Ultra-massive Multiple-Input Multiple-Output Communications

In order to overcome the very high path loss in ISLs, very high gain directional antenna systems are required. As discussed in subsection 6.3.2, the next generation CubeSats will incorporate very large multi-band antenna arrays. Similarly as in the terrestrial case, MIMO [145], massive MIMO [146] and ultra-massive MIMO [2] systems can be utilized. The latter is specially relevant as we move towards mmWave and THz-band frequencies for satellite communications. The key concept of ultra-massive MIMO communications

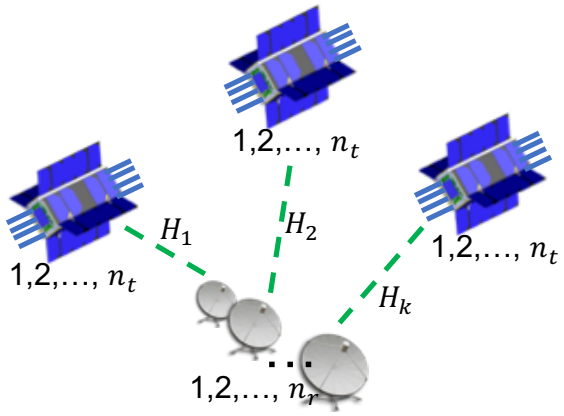

Figure 6.8: An illustration of a distributed MIMO communication link in IoST.

is to increase the coverage range at mmWave and THz-band frequencies by simultaneously focusing the transmitted signals in space and in frequency. Ultra-massive MIMO enables different communication modes, ranging from ultra-massive beamforming for maximum communication range; ultra-massive spatial multiplexing, for increased throughput and multi-user capacity; and, multi-band ultra-massive MIMO, which allows simultaneous transmission over multiple mmWave and THz-band transmission windows. All these modes are enabled by the aforementioned antenna arrays, which can, in addition, be virtually divided in sub-arrays on demand.

6.4.5 Distributed Multiple-Input Multiple-Output Communication in IoST

Besides MIMO communication across CubeSats, distributed MIMO communication schemes between a set of CubeSats and ground devices, other satellites (e.g., LEO, MEO) or deep-space systems can be created [147]. The advantages of distributed MIMO communication include power and route optimization, as well as higher spatial diversity. With the limited form factor of CubeSats, it is difficult to contain large energy source to boost signal strength, which further limit the capacity of each CubeSat. However, with multiple CubeSats sharing the same task of data transmission, the burden of power consumption is reduced. Moreover, with multiple CubeSats covering the same point of interest, the data routing can be optimally planned. As shown in Figure 6.8, three CubeSats, each with n_t

antennas, are covering the same ground station with n_r antennas. The distributed MIMO communication is expected to improve the spectral efficiency as well as the energy efficiency of the IoST network.

6.4.6 Resource Allocation Techniques

To maximize the achievable data-rates in ISLs as well as the aggregated network user capacity in the IoST, new resource allocation strategies are needed. In the context of the IoST, the resources available to the CubeSats include: i) different frequency bands (from RF to THz) with different transmission bandwidths (from 10 MHz to 100 GHz); ii) different number of antenna elements, which can be virtually grouped in sub-arrays and tuned at the different frequency bands; iii) different modulation and coding strategies, ranging form the traditional m-PSK and m-QAM with Forward Error Correction (FEC) schemes, to new modulation and coding strategies tailored to the mmWave and THz-band channels [46]; and, iv) different medium access control strategies, for unicast, multicast and broadcast information, over the different frequency bands. The resource allocation can be formulated as an optimization problem that can be solved by the help of SDN and *machine learning algorithms* given the number of devices to be served on Earth, the area on Earth needs to be covered, and the energy provided to each CubeSat [90]. For example, among multiple frequency bands, mmWave and THz frequencies are desired to serve in the ISL to achieve ultra-fast backbone link. While nowadays on-Earth sensors might not have mmWave transceivers, the CubeSats can reach ground infrastructure with mmWave links, as a supplement to lower frequency links. With the proliferation of applications using artificial intelligence and machine learning algorithms, such resource allocation strategies are best optimized with the help of deep learning and clustering algorithms, where the IoST can adaptively select the best available frequency channel, transmit power, modulation and coding scheme, and so on.

Optimization Problem Formulation

In an ISL, we consider a four-tuple parameter set for resource allocation, which includes the transmit power P_t, the bandwidth W_b, the center frequency f_c, and the directivity of plasmonic reflectarray antennas D_t. We can formulate an optimization problem in the following form,

$$\begin{aligned}
\textit{Given: } & n_s^{(k)}, K, n_0^{(k,l)}, e_0^{(k,l)}, i_0^{(k,l)}, M_0^{(k,l)}, \alpha_0^{(k,l)}, \\
& \Gamma_{\min}^{(x)}, \mathrm{BER}_{\min}^{(x)}, P_{\mathrm{res}}^{(k,l)}, \mathbf{f}_c, \mathbf{W}_b, \gamma_R. && (6.3)\\
\textit{Find: } & P_t^{(k,l,x)}, f_c^{(k,l,x)}. && (6.4)\\
\textit{Objectives: } & \max \sum \Gamma^{(k,l,x)}. && (6.5)\\
\textit{Subject to: } & \sum P_t^{(k,l,x)} \leq P_t^{\mathrm{tot}} \text{ (Transmit power allocation)}, && (6.6)\\
& \sum n_s^{(k,l,x)} \leq N_s^{\mathrm{tot}} \text{ (CubeSat allocation)}, && (6.7)\\
& \sum D^{(k,l,x)} \leq D^{(k,l)} \text{ (Antenna array allocation)}, && (6.8)\\
& \Gamma\left(P_t^{(k,l,x)}, n_s^{(k,l,x)}, D^{(k,l,x)}\right) \geq \Gamma_{\min}^{(x)}, \\
& \forall k \in K \text{ and } \forall l \in L_{orb}. && (6.9)
\end{aligned}$$

We can observe that this problem is a combinatorial optimization problem which cannot be easily solved. Therefore, we seek help from machine learning techniques which have recently burgeoned for communication network use cases.

Resource Allocation Optimization via DNN

In the field of machine learning, deep learning has recently gained significantly promising results in tackling complicated wireless network problems with large data volumes [148]. It is fair to believe that future wireless communication networks will be more intelligent with the utilization of deep learning techniques. In the space network, we also face the challenges of handling, processing, and transmitting sheer amount of data amongst CubeSats

and ground stations in complicated space channels. Lacking real-time knowledge of CubeSat orbital conditions and only having centralized control stations on the Earth will not only hinder prompt data handling, but also often yield undesirable end-to-end throughput. The resource allocation scheme is resulted from a deep neural network (DNN) that aims to optimize the frequency bands, transmitted power levels, as well as adjust the radiation patterns of reconfigurable antenna arrays. Since the optimization targets are independent of each other, we can train an ensemble deep neural network with each finding the global optimum of the specific goal.

In classic DNN architectures, each neuron connected through multiple layers has a certain associated weight which is determined by the algorithm called backpropagation [149]. Backpropagation relies on calculating the gradient of the loss function in order to adjust the initial weights of neurons, which has been proved to be an efficient solution to find the global optima. However, in scenarios where computation complexity and energy consumption become major constraints in employing backpropagtion for finding optimal weights, other efficient yet less energy-draining methods should be considered. In particular, randomized optimization algorithms are preferable candidates in the CubeSat communication network.

Random hill-climbing (RHC) algorithm finds the "peak" value among all values in the "landscape" by comparing the current value with the one in previous step. It has the advantages of low memory requirement as well as low time complexity, compared to neural networks with backpropagation and other optimization methods including the genetic algorithm and simulated annealing. The initial step is randomly chosen. Then a modification is made in the next step and comparison is performed with the previous one: if current step yields a better solution, then we accept it as the temporary solution, and continue moving along the same direction as well as making comparison with next steps; if current step does not outperform the previous one, then we discard it and suggest a new value, or "restart" the research for the local optimal solution. After some iterations, the number of which is

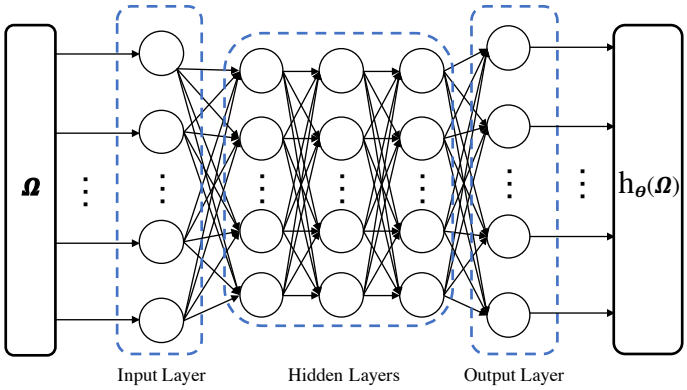

Figure 6.9: Architecture of the deep neural network for CubeSat links. Five layers of neurons are connected to process the input feature space Ω.

predetermined, or the improvement is not significant, the algorithm will stop.

In the CubeSat network, with the intrinsic characteristics of limited power and on-board memory budget, we apply random hill climbing algorithm in the DNN in place of the backpropagation. In our DNN, as shown in Figure 6.9, we first construct the input feature space Ω, which is a matrix with the following quantized column vectors based on the real orbital data from the Iridium,

$$\mathbf{\Omega} = [\iota, \gamma_R, f_D, T, \Gamma_{min}, \text{BER}_{min}, f_c^{(all)}, W_b^{(all)}]^\intercal. \tag{6.10}$$

We then employ the sigmoid function as the activation function in this DNN, which is expressed as $h_\theta(\mathbf{\Omega}) = \frac{1}{1+\exp(-\theta^\intercal \mathbf{\Omega})}$. We then construct a multi-class classification output as $\mathbf{y} = h_\theta(\mathbf{\Omega}) \in \mathbb{R}^S$, in which S is the size of the output units, or the number of classes. The output units are column vectors each with all elements to be 0 except one element has a value of "1" indicating the classified output. In each deep neural network in our ensemble structure, we have four layers, and the number of hidden neurons in the layers are $[75, 50, 30, 12, 6]$. The output is corresponding to the indicator value which points to the selected frequency bands, and transmitted power level. In the training data, we split the training dataset into 80% and 20% as the training and the validation set to perform cross-validation on the weights. The numerical results on link performance based on the selected

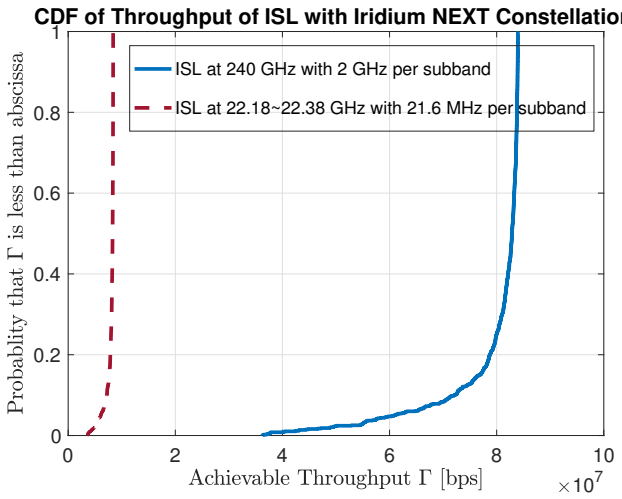

Figure 6.10: Comparison of the CDF of throughput with existing Iridium NEXT frequencies and proposed mmWave/THz dynamic resource allocation scheme.

parameters are drawn in the following section.

In the perspective of actual deployment, recent advancements have been made available in industry to ensure ultra-low power consumption and miniaturized size for neural computation hardware. For example, the Movidius technology developed by Intel is the miniaturized neural compute engine which can ignite the future deployment of deep neural network at very low power consumption, implying a good fit for low power budget in CubeSats.

Based on the DNN we constructed and trained with inputs based on the real orbital data from Iridium NEXT constellation, we can perform testing using the connected neurons with weights found by random hill-climbing technique. In our simulated satellite communication scenarios, a pair of fixed end-users are on the ground with two locations on the east and west hemisphere and hence rely on the satellite network for communications. Therefore in the end-to-end link path which consists of a GSL uplink, multiple ISLs, and a GSL downlink, we compare the performance in terms of the achievable throughput values with various link distance (e.g., the arc-length distance in ISLs), and the maximum throughput CubeSat network can achieve by using the dynamic resource allocation scheme in ISLs.

In ISL data links, we apply the forward error correction with the $BCH(63, 39, 4)$ cod-

ing scheme and QPSK is used as the modulation scheme. We send a packet with a total length of 1500 bytes. According to the Iridium NEXT constellation, the frequency bands for ISL spans eight channels in 22.18–22.38 GHz, each with a 21.6 MHz bandwidth, the feeder uplink has 13 channels in 29.1–29.3 GHz and downlink has 13 channels in 19.4–19.6 GHz, each with approximately 15.3 MHz bandwidth. In our proposed CubeSat links, the candidate frequency bands for ISL include 60, 140, 240, 300, and 420 GHz.

6.4.7 Challenges in Physical Layer Techniques

As mentioned before, UM MIMO communications will enhance the link performance. However, the realization of UM MIMO schemes in the IoST, however, introduces several challenges. First of all, the performance of UM MIMO drastically depends on the available channel information. For this, on the one hand, accurate end-to-end channel models accounting for both the impact of the antenna arrays in transmission and reception as well as the propagation medium are needed. While multi-path propagation in the exosphere is highly unlikely, reflections from the CubeSat components (e.g., solar panels) in the vicinity of the receiving antenna need to be taken into account. In addition, as the number of elements in orbit increases and space trash accumulates, reflections and scattering can increase. On the other hand, with the channel models in hand, low-complexity real-time channel estimation and prediction algorithms are needed, which should take into account the relative motion of CubeSats.

In light of the channel information, the second major challenge to address relates to the control and operation of the array. New dynamic beamforming algorithms are needed to implement the different operation modes described above. The control algorithms need to be tailored to the specific array architecture, and in particular, the phase/delay and amplitude control available per element or per group of elements (sub-array). In the simplest case, a predefined codebook with multiple common beam patterns can be designed preloaded in the CubeSats, specially taking into account that, once deployed, the CubeSat

network topology is not expected to change much. However, in case of CubeSat failure or new additions, the possibility to redefine new codebooks on demand is also desirable.

Additionally, the realization of distributed MIMO systems among CubeSats introduces several open issues. The major roadblock to overcome is the need for accurate time, frequency and phase synchronization between CubeSats. On the one hand, part of this information is already available at the ADCS (see Figure 6.1, section 6.3). On the other hand, however, this information needs to be accessible and shared among the distributed MIMO CubeSat set, in an efficient manner. Additional challenges include the development of mechanisms to compensate for oscillators deviations in time which can lead to clock skew, phase noise in mmWave and THz-band transceivers, and changing EM wave propagation speed as it traverses different layers of the atmosphere with different molecules species and concentrations.

6.5 Summary

This chapter presents the design of a multi-band CubeSat, which integrates front-ends and antennas able to communicate simultaneously in multiple bands ranging from the microwave to the mmWave and the THz band. Moreover, through link budget analyses in inter-satellite links, we show the great link potential of such CubeSat inter-satellite communication system. This design is envisioned to serve as a potential solution to enable multi-frequency space network architecture for future ubiquitous communications.

CHAPTER 7
CONCLUSION AND FUTURE WORK

7.1 Summary of Contributions

Recent years have witnessed a dramatic rise in wireless data traffic brought forth by numerous exciting technologies in wireless communications. This exponential growth has been accompanied by the demand for higher data rates and better coverage. Among emerging research and development trends in wireless communications, THz communications has been envisioned as one of the key enabling technologies for the next decade. Buoyed by the availability of ultra-wide spectrum resources, the THz band can provide terabits per second (Tbps) links for a plethora of applications, ranging from ultra-fast massive data transfer among nearby devices in Terabit Wireless Personal and Local Area Networks to high-definition videoconferencing among mobile devices in small cells, as well as inter-satellite communications in space networks.

In this thesis, we strive to address the important problem inherent in these frequency bands for their applications in both terrestrial and space communication systems. The contributions in each chapter are summarized as follows:

- In Chapter 2, we propose the UM MIMO platforms consisting of reconfigurable antenna arrays, enabled by either graphene or metasurfaces and utilized in transmission, reception, and controlled reflection. An end-to-end analytical physical model has been developed and analyzed to highlight the significant enhancement in both transmission distance and achievable spectral efficiency. Further, we analyze the distance limitation problem and NLoS issue faced by both mmWave and THz bands caused by atmospheric attenuation and molecular absorption in wireless communication systems. Based on the analyses, simulation results demonstrate at least five

times distance improvement in utilizing the proposed intelligent communication environments in real-world communication scenarios.

- In Chapter 3, we present beamforming and beam-steering designs to achieve high spectral efficiency at mmWave and THz-band frequencies in order to enhance the communication distance. Two beamforming schemes based on optimal continuous phase shifts with reconfigurable reflectarray and a phase-gradient metasurfaces are discussed. In addition, a dual-polarization channel model based on reconfigurable reflectarray is proposed and analyzed under an array-of-subarray architecture. Owing to the feature of reconfigurable electromagnetic characteristic of advanced artificial 2D materials such as metasurfaces, dynamic polarization states can be achieved and utilized to realize polarization diversity in wireless channels. A precoding design based on optimizing the dominant paths' strengths is proposed and analyzed. Simulation results are obtained to verify such polarization diversity gain.

- In Chapter 4, we present a time-varying channel modeling and tracking approach in 3-D indoor environments for THz band communication systems. The channel model can be especially useful in facilitating realistic channel estimation that requires a high level of accuracy without sacrificing the time-efficiency. Our model introduces the extended Kalman filtering and continuous-time Markov chain to model and track the dynamic path behavior for LoS path and multipaths, respectively. Moreover, the simulation results at various frequency bands show a good general applicability of the time-varying channel model in THz channel, with analysis of major time-varying channel characteristics. Finally, the simulation results based on the proposed model are validated by 3D ray-tracing.

- In Chapter 5, we first describe the effects of Earth's upper atmosphere and solar activities with respect to communications in the THz spectrum. In particular, we show that even though ionized particles are active in the ionosphere, no significant impact

will be cast on THz links, making THz band a feasible carrier for near-Earth links. Furthermore, for deep-space links, only severe solar activities can cause angular instability at THz band. We further analyze the orbit perturbation caused by various factors in space and propose a model characterizing such effects. Finally, based on the characterization of space channels, we present a link-level analysis for diversity-based TeraSpace channel. In particular, we demonstrate the spectral efficiency over various THz frequency bands and link distances. Simulation results show that with the TeraSpace link can achieve a maximum throughput of 172 Gbps at 120 GHz, proving a promising space communication application using the THz band.

- In Chapter 6, we present the design of a multi-band CubeSat, which integrates front-ends and antennas able to communicate simultaneously in multiple bands ranging from the microwave to the mm-wave and the THz band. Moreover, through link budget analyses in inter-satellite links, we show the great link potential of such CubeSat inter-satellite communication system. We also provide analysis on weather effect on the ground-to-satellite links and discuss challenges for future design and deployment. This design is envisioned to serve as a potential solution to enable multi-frequency space network architecture for future ubiquitous communications.

7.2 Future Directions

On the basis of current research progress, we recognize a number of open problems need to be addressed in order to facilitate the THz band communication to achieve the goal of Tbps-level throughput.

- *Trade-off Between Dimensions and Energy Consumption:* In terms of real-world applications, the Intelligent Environments are expected to be coated onto surfaces of interior walls and/or ceilings, and building facades, which require dimensions that can both fit specific installation areas and satisfy link requirements. Meanwhile, with

more reflectarray elements and RF chains built into the system, the energy consumption will also increase, due to the advanced signal processing circuitry. Therefore, how to achieve an economic solution to balance the overall dimension and energy consumption while serving users to its desired performance is a nontrivial issue.

- *Compatibility With Existing Solutions:* Current Wi-Fi access points have a mature protocol stack to sense the channel and establish links with users. In order for the Intelligent Environments to assist with improving indoor signal coverage, it needs to be compatible with the IEEE 802.11 series standard. For now this is still under research and serves as a worthy problem for novel solutions.

- *Standardization:* With many candidate approaches being investigated in reflectarrays, metasurfaces, frequency selective surfaces, among others, there has not been a consensus on how to standardize the device architecture, maximum emitted power, and communication protocols. As more ideas evolve, a standardization effort within a work group is necessary towards a solid framework.

- *Coordinated Intelligent Communication Environments with Multiple Reconfigurable Reflectarrays:* With multiple reconfigurable reflectarrays deployed in the environment, the sum data-rate will significantly improve. However, a relevant question is the coordination among them. Algorithms for fair user scheduling as well as resource allocation for each user are needed to address the problem. In addition, machine learning solutions are favorable to optimize the unconventional configuration of the intelligent wireless environments.

- *Design and Prototyping of Intelligent Communication Environments:* On the basis of theoretical analysis and design, the prototyping of intelligent communication environments is a crucial step to validate the results. Current large area electronics techniques, as well as advanced control circuitry based on FPGAs, can greatly facilitate the development of the actual layout and configuration of the reconfigurable

reflectarrays.

7.3 Publications

As part of the research conducted in this dissertation, we have the following documents that are either published, submitted, or in progress, as follows:

Journals

1. S. Nie, C. Han, and I. F. Akyildiz, "Channel Modeling and Analysis of Inter-Small-Satellite Links in Terahertz Band Space Networks," submitted to IEEE Transactions on Communications, under revision, Mar. 2021.

2. C. Liaskos, S. Nie, A. Tsioliaridou, A. Pitsillides, S. Ioannidis, and I. F. Akyildiz, "End-to-end Wireless Path Deployment with Intelligent Surfaces Using Interpretable Neural Networks," *IEEE Transactions on Communications*, vol. 68, no. 11, pp. 6792–6806, 2020.

3. I. F. Akyildiz, A. Kak, and S. Nie, "6G and Beyond: The Future of Wireless Communications Systems," *IEEE Access*, vol. 8, pp. 133 995–134 030, 2020.

4. C. Liaskos, A. Tsioliaridou, S. Nie, A. Pitsillides, S. Ioannidis, and I. F. Akyildiz, "On the network-layer modeling and configuration of programmable wireless environments," *IEEE/ACM Transactions on Networking*, vol. 27, no. 4, pp. 1696–1713, 2019.

5. C. Liaskos, S. Nie, A. Tsioliaridou, A. Pitsillides, S. Ioannidis, and I. F. Akyildiz, "A novel communication paradigm for high capacity and security via programmable indoor wireless environments in next generation wireless systems," *Ad Hoc Networks*, vol. 87, pp. 1–16, 2019.

6. C. Liaskos, S. Nie, A. Tsioliaridou, A. Pitsillides, S. Ioannidis, and I. F. Akyildiz,

"A New Wireless Communication Paradigm through Software-controlled Metasurfaces," *IEEE Communications Magazine*, vol. 56, no. 9, pp. 162–169, 2018.

7. I. F. Akyildiz, C. Han, and S. Nie, "Combating the Distance Problem in the Millimeter Wave and Terahertz Frequency Bands," *IEEE Communications Magazine*, vol. 56, no. 6, pp. 102–108, 2018.

8. I. F. Akyildiz, J. M. Jornet, and S. Nie, "A New CubeSat Design with Reconfigurable Multi-band Radios for Dynamic Spectrum Satellite Communication Networks," *Ad Hoc Networks*, vol. 86, pp. 166–178, 2019.

Conferences

1. S. Nie and I. F. Akyildiz, "Codebook Design for Dual-Polarized Ultra-Massive MIMO Communications in MillimeterWave and Terahertz Bands," to appear in 2021 IEEE International Conference on Acoustics, Speech and Signal Processing (ICASSP), June 2021.

2. S. Nie and I. F. Akyildiz, "Beamforming in Intelligent Environments based on Ultra-Massive MIMO Platforms in MillimeterWave and Terahertz Bands," in 2020 IEEE International Conference on Acoustics, Speech and Signal Processing (ICASSP), May 2020, pp. 8683–8687.

3. C. Liaskos, S. Nie, A. Tsioliaridou, A. Pitsillides, S. Ioannidis, and I. F. Akyildiz, "Mobility-aware beam steering in metasurface-based programmable wireless environments," in 2020 IEEE International Conference on Acoustics, Speech and Signal Processing (ICASSP), May 2020, pp. 9150–9154.

4. S. Nie, J. M. Jornet, and I. F. Akyildiz, "Intelligent environments based on ultra-massive MIMO platforms for wireless communication in millimeter wave and terahertz bands," in 2019 IEEE International Conference on Acoustics, Speech and Signal Processing (ICASSP), 2019, pp. 7849–7853.

5. S. Nie, J. M. Jornet, and I. F. Akyildiz, “Deep-Learning-Based Resource Allocation for Multi-Band Communications in CubeSat Networks,” in 2019 IEEE International Conference on Communications Workshops (ICC Workshops), May 2019, pp. 1–6.

6. S. Nie and I. F. Akyildiz, “Three-Dimensional Dynamic Channel Modeling and Tracking for Terahertz Band Indoor Communications,” in IEEE 28th International Symposium on Personal, Indoor and Mobile Radio Communications (PIMRC), October 2017, pp. 1–5.

7. S. Nie, C. Han, and I. F. Akyildiz, “A three-dimensional time-varying model for 5G indoor dual-mobility channels,” in IEEE 86th Vehicular Technology Conference (VTC), September 2017, pp. 1–5.

Appendices

APPENDIX A

PROOF OF LEMMA IN CHAPTER 5

Proof. From Equation 5.5, we have the relative motion expressed as

$$\ddot{\mathbf{p}} = \ddot{\mathbf{r}_{\mathrm{F}}} - \ddot{\mathbf{r}_{\mathrm{L}}} = -\mu\frac{\mathbf{r}_{\mathrm{F}}}{||\mathbf{r}_{\mathrm{F}}||^3} + \mu\frac{\mathbf{r}_{\mathrm{L}}}{||\mathbf{r}_{\mathrm{L}}||^3} + \mathbf{f}_{\mathrm{F}} - \mathbf{f}_{\mathrm{L}} \quad = -\mu\frac{\mathbf{r}_{\mathrm{L}}+\mathbf{p}}{||\mathbf{r}_{\mathrm{L}}+\mathbf{p}||^3} + \mu\frac{\mathbf{r}_{\mathrm{L}}}{||\mathbf{r}_{\mathrm{L}}||^3} + \mathbf{f}_{\mathrm{F}} - \mathbf{f}_{\mathrm{L}}, \tag{A.1}$$

where $\mathbf{p} = \mathbf{r}_{\mathrm{F}} - \mathbf{r}_{\mathrm{L}}$. Based on Equation 5.10 and the values of solar pressure per unit surface and the small SMR values of small satellites, the solar radiation pressure-induced force on small satellites is has a negligible impact compared to the J_2 effect. Hence, the external force on each satellite $\mathbf{f}_{\mathrm{F/L}}$ is approximated as $\mathbf{f}_{\mathrm{J_2}}$. Similarly, if we express $\mathbf{r}_{\mathrm{F}} = \mathbf{r}_{\mathrm{L}} + \mathbf{p}$ and use U to represent $\frac{3\mu J_2 R_e^2}{2}$ for convenience, from Equation 5.8 we have

$$\mathbf{f}_{\mathrm{J_2,F}} = \frac{U}{||\mathbf{r}_{\mathrm{L}}+\mathbf{p}||^5}\left[\left(5\frac{\left(\mathbf{r}_{\mathrm{F}}\cdot\mathbf{z}_{\mathrm{G}}\right)^2}{||\mathbf{r}_{\mathrm{L}}+\mathbf{p}||^2} - 1\right)\left(\mathbf{r}_{\mathrm{L}}+\mathbf{p}\right) - 2\left(\mathbf{r}_{\mathrm{F}}\cdot\mathbf{z}_{\mathrm{G}}\right)\mathbf{z}_{\mathrm{G}}\right], \tag{A.2}$$

where $\mathbf{z}_{\mathrm{G}}$ is unit vector along the z-axis in the ECI frame and equals $[0\ 0\ 1]^{\intercal}$. Therefore, $\mathbf{r}_{\mathrm{F}}\cdot\mathbf{z}_{\mathrm{G}} = z_{\mathrm{F}}$, which is the z component of the satellite state vector (also in the ECI frame). For the leading satellite, we also have

$$\mathbf{f}_{\mathrm{J_2,L}} = \frac{U}{||\mathbf{r}_{\mathrm{L}}||^5}\left[\left(5\frac{z_{\mathrm{L}}^2}{||\mathbf{r}_{\mathrm{L}}||^2} - 1\right)\mathbf{r}_{\mathrm{L}} - 2z_{\mathrm{L}}\mathbf{z}_{\mathrm{G}}\right], \tag{A.3}$$

where $\mathbf{r}_{\mathrm{L}}\cdot\mathbf{z}_{\mathrm{G}} = z_{\mathrm{L}}$. We then expand $\frac{1}{||\mathbf{r}_{\mathrm{L}}+\mathbf{p}||^3}$ as

$$\begin{aligned}\frac{1}{||\mathbf{r}_{\mathrm{L}}+\mathbf{p}||^3} &= \frac{1}{\left(\left(\mathbf{r}_{\mathrm{L}}+\mathbf{p}\right)\cdot\left(\mathbf{r}_{\mathrm{L}}+\mathbf{p}\right)\right)^{3/2}} = \frac{1}{\left(\mathbf{r}_{\mathrm{L}}\cdot\mathbf{r}_{\mathrm{L}} + 2\mathbf{r}_{\mathrm{L}}\cdot\mathbf{p} + \mathbf{p}\cdot\mathbf{p}\right)^{3/2}} \\ &= \frac{1}{\mathbf{r}_{\mathrm{L}}^3\left(1 + 2\left(\frac{\mathrm{p}}{\mathbf{r}_{\mathrm{L}}}\right)\cos\varrho\left(\frac{\mathrm{p}}{\mathbf{r}_{\mathrm{L}}}\right)^2\right)},\end{aligned} \tag{A.4}$$

where ϱ is the angle between vectors $\mathbf{p}$ and $\mathbf{r}_{\mathrm{L}}$, $\cos\varrho = \frac{\mathbf{r}_{\mathrm{L}}\cdot\mathbf{p}}{||\mathbf{r}_{\mathrm{L}}||||\mathbf{p}||}$. Using a first-order Taylor expansion and in satellite formation flying that $\frac{\mathbf{p}}{\mathbf{r}_{\mathrm{L}}} \ll 1$,

$$\begin{aligned}
\frac{1}{||\mathbf{r}_{\mathrm{L}}+\mathbf{p}||^3} &\approx \frac{1}{||\mathbf{r}_{\mathrm{L}}||^3} - \frac{3\left(p/r_{\mathrm{L}}\right)\cos\varrho}{||\mathbf{r}_{\mathrm{L}}||^3} = \frac{1}{||\mathbf{r}_{\mathrm{L}}||^3} - \frac{3\mathbf{p}\cdot\mathbf{r}_{\mathrm{L}}}{||\mathbf{r}_{\mathrm{L}}||^5}, \\
\frac{1}{||\mathbf{r}_{\mathrm{L}}+\mathbf{p}||^5} &\approx \frac{1}{||\mathbf{r}_{\mathrm{L}}||^5} - \frac{5\left(p/r_{\mathrm{L}}\right)\cos\varrho}{||\mathbf{r}_{\mathrm{L}}||^5} = \frac{1}{||\mathbf{r}_{\mathrm{L}}||^5} - \frac{5\mathbf{p}\cdot\mathbf{r}_{\mathrm{L}}}{||\mathbf{r}_{\mathrm{L}}||^7}.
\end{aligned} \tag{A.5}$$

Therefore, when neglecting expanded terms with r_{L}^7 and r_{L}^9 in the denominator which have negligible impact on the relative motion, we can have

$$\ddot{\mathbf{p}} \approx -\mu\frac{\mathbf{p}}{r_{\mathrm{L}}^3} + \frac{3\mu\mathbf{r}_{\mathrm{L}}\left(\mathbf{p}\cdot\mathbf{r}_{\mathrm{L}}\right)}{r_{\mathrm{L}}^5} + \frac{2U}{r_{\mathrm{L}}^5}\left(z_{\mathrm{L}} - z_{\mathrm{F}}\right)\mathbf{z}_{\mathrm{G}}. \tag{A.6}$$

It is noticed that the J_2 effect only affects the components along the z-axis, which can be expressed as the difference between the satellite pairs in their z-coordinate in the ECI frame, or the difference of true anomalies of the satellite pairs, shown as the angle γ in Figure 5.5. When transforming Equation A.6 into the state vector form, we have three equation similar to Equation 5.6c, except for the last one, which is

$$\ddot{z} = 3\omega^2 z + 2\omega\dot{x} + \frac{2Uh}{r_l^5}, \tag{A.7}$$

where $h = z_{\mathrm{L}} - z_{\mathrm{F}}$ as the initial condition. Taking the Laplace transform for both sizes, we have

$$s^2 z - s z_0 - \dot{z_0} + w_0^2 z = \frac{2\omega_0 \dot{x_0}}{s} + \frac{4\omega^2 z_0}{s} + \frac{8\omega U h}{r_l^5 s}, \tag{A.8}$$

and solving for z through inverse Laplace transform and the relation of $\frac{1}{s\left(s^2+\omega_0^2\right)} = \frac{1}{s\omega_0^2} - \frac{s}{\omega_0^2\left(s^2+\omega_0^2\right)}$, we have

$$z = 4z_0 + \frac{2}{\omega_0}\dot{x}_0 + \frac{z_0}{\omega_0}\sin\omega_0 t - \left(3z_0 + \frac{2\dot{x}_0}{\omega_0}\right)\cos\omega t + \frac{8Uh}{r_l^5\omega_0}\left(1-\cos\omega_0 t\right). \tag{A.9}$$

Therefore, the relative motion without secular drift can be expressed as

$$
\begin{aligned}
x(t) &= 6\sin\omega t z_0 + x_0 - \frac{2}{\omega}\left(1-\cos\omega t\right)\dot{z_0} + \frac{4\sin\omega t}{\omega}\dot{x_0}, \\
y(t) &= y_0\cos\omega_0 t + \frac{\dot{y_0}}{\omega}\sin\omega_0 t, \\
z(t) &= \frac{\dot{z_0}}{\omega_0}\sin\omega_0 t - \left(3z_0 + \frac{2\dot{x_0}}{\omega_0}\right)\cos\omega_0 t - \frac{8Uh}{r_l^5\omega_0} - \cos\omega_0 t.
\end{aligned}
\tag{A.10}
$$

In order to analyze the angular misalignment, we need to convert the Cartesian coordinates to Euler angles, which follows

$$
\begin{aligned}
\tan\phi &= \frac{y(t)}{z(t)} = \frac{y_0\cos\omega_0 t + \frac{\dot{y_0}}{\omega}\sin\omega_0 t}{\frac{\dot{z_0}}{\omega_0}\sin\omega_0 t - \left(3z_0 + \frac{2\dot{x_0}}{\omega_0}\right)\cos\omega_0 t - \frac{8Uh}{r_l^5\omega_0} - \cos\omega_0 t}, \\
\tan\theta &= \frac{-x(t)}{\sqrt{y(t)^2 + z(t)^2}} \\
&= -\frac{6\sin\omega t z_0 + x_0 - \frac{2}{\omega}\left(1-\cos\omega t\right)\dot{z_0} + \frac{4\sin\omega t}{\omega}\dot{x_0}}{\sqrt{\left(y_0\cos\omega_0 t + \frac{\dot{y_0}}{\omega}\sin\omega_0 t\right)^2 + \left(\frac{\dot{z_0}}{\omega_0}\sin\omega_0 t - \left(3z_0 + \frac{2\dot{x_0}}{\omega_0}\right)\cos\omega_0 t - \frac{8Uh}{r_l^5\omega_0} - \cos\omega_0 t\right)^2}}
\end{aligned}
\tag{A.11}
$$

The cumulative distribution function of the angle variation obtained from Equation A.11 is plotted in Figure 5.6, which follows a wrapped Gaussian distribution with different mean and variance values. □

REFERENCES

[1] I. F. Akyildiz, A. Kak, and S. Nie, "6G and Beyond: The Future of Wireless Communications Systems," *IEEE Access*, vol. 8, pp. 133 995–134 030, 2020.

[2] I. F. Akyildiz and J. M. Jornet, "Realizing ultra-massive MIMO (1024× 1024) communication in the (0.06–10) terahertz band," *Nano Communication Networks*, vol. 8, pp. 46–54, 2016.

[3] S. Abadal, C. Han, and J. M. Jornet, "Wave propagation and channel modeling in chip-scale wireless communications: A survey from millimeter-wave to terahertz and optics," *IEEE Access*, vol. 8, pp. 278–293, 2019.

[4] T. Nagatsuma, G. Ducournau, and C. C. Renaud, "Advances in terahertz communications accelerated by photonics," *Nature Photonics*, vol. 10, no. 6, p. 371, 2016.

[5] T. Ishibashi, Y. Muramoto, T. Yoshimatsu, and H. Ito, "Unitraveling-carrier photodiodes for terahertz applications," *IEEE Journal of Selected Topics in Quantum Electronics*, vol. 20, no. 6, pp. 79–88, Nov. 2014.

[6] H. Ito and T. Ishibashi, "Photonic Terahertz-Wave Generation Using Slot-Antenna-Integrated Uni-Traveling-Carrier Photodiodes," *IEEE Journal of Selected Topics in Quantum Electronics*, vol. 23, no. 4, pp. 1–7, Jul. 2017.

[7] J. L. Kloosterman *et al.*, "Hot electron bolometer heterodyne receiver with a 4.7-THz quantum cascade laser as a local oscillator," *Applied Physics Letters*, vol. 102, no. 1, p. 011 123, 2013.

[8] N. M. Burford and M. O. El-Shenawee, "Review of terahertz photoconductive antenna technology," *Optical Engineering*, vol. 56, no. 1, p. 010 901, 2017.

[9] A. E. Yachmenev *et al.*, "Metallic and dielectric metasurfaces in photoconductive terahertz devices: A review," *Optical Engineering*, vol. 59, no. 6, p. 061 608, 2019.

[10] O. Momeni and E. Afshari, "A broadband mm-wave and terahertz traveling-wave frequency multiplier on CMOS," *IEEE Journal of Solid-State Circuits*, vol. 46, no. 12, pp. 2966–2976, 2011.

[11] D. Gamzina *et al.*, "Backward wave oscillator for high power generation at THz frequencies," in *Terahertz Emitters, Receivers, and Applications VIII*, International Society for Optics and Photonics, vol. 10383, 2017, p. 1 038 303.

[12] P. Vazquez *et al.*, "Towards THz high data-rate communication: a 50 Gbps all-electronic wireless link at 240 GHz," in *Proc. of the 4th ACM International Conference on Nanoscale Computing and Communication*, ACM, 2017, p. 25.

[13] I. F. Akyildiz, J. M. Jornet, and C. Han, "Terahertz band: Next frontier for wireless communications," *Physical Communication*, vol. 12, pp. 16–32, 2014.

[14] A. Zak *et al.*, "Antenna-integrated 0.6 THz FET direct detectors based on CVD graphene," *Nano Letters*, vol. 14, no. 10, pp. 5834–5838, 2014.

[15] I. F. Akyildiz and J. M. Jornet, *Graphene-based Plasmonic Nano-antenna for Terahertz Band Communication*, US Patent App. 14/253,539, Jul. 2016.

[16] ——, *Graphene-based Plasmonic Nano-Transceiver employing HEMT for Terahertz Band Communication*, US Patent App. 14/560,213, Jun. 2015.

[17] J. M. Jornet and I. F. Akyildiz, "Channel Modeling and Capacity Analysis of Electromagnetic Wireless Nanonetworks in the Terahertz Band," *IEEE Transactions on Wireless Communications*, vol. 10, no. 10, pp. 3211–3221, Oct. 2011.

[18] S. Priebe and T. Kurner, "Stochastic modeling of THz indoor radio channels," *IEEE Transactions on Wireless Communications*, vol. 12, no. 9, pp. 4445–4455, 2013.

[19] D. He *et al.*, "Stochastic channel modeling for kiosk applications in the terahertz band," *IEEE Transactions on Terahertz Science and Technology*, vol. 7, no. 5, pp. 502–513, 2017.

[20] I. F. Akyildiz, C. Han, and S. Nie, "Combating the Distance Problem in the Millimeter Wave and Terahertz Frequency Bands," *IEEE Communications Magazine*, vol. 56, no. 6, pp. 102–108, Jun. 2018.

[21] J. M. Jornet and I. F. Akyildiz, "Graphene-based Plasmonic Nano-transceiver for Terahertz Band Communication," in *Proc. of European Conference on Antennas and Propagation (EuCAP)*, 2014.

[22] C. Han, X. Zhang, and X. Wang, "On medium access control schemes for wireless networks in the millimeter-wave and terahertz bands," *Nano communication networks*, vol. 19, pp. 67–80, 2019.

[23] R. R. Choudhury and N. H. Vaidya, "Deafness: A mac problem in ad hoc networks when using directional antennas," in *Proceedings of the 12th IEEE International Conference on Network Protocols*, IEEE, 2004, pp. 283–292.

[24] C. Han, W. Tong, and X.-W. Yao, "Ma-adm: A memory-assisted angular-division-multiplexing mac protocol in terahertz communication networks," *Nano communication networks*, vol. 13, pp. 51–59, 2017.

[25] X. Gao, L. Dai, Y. Zhang, T. Xie, X. Dai, and Z. Wang, "Fast channel tracking for terahertz beamspace massive mimo systems," *Ieee transactions on vehicular technology*, vol. 66, no. 7, pp. 5689–5696, 2016.

[26] S. Collonge, G. Zaharia, and G. E. Zein, "Influence of the human activity on wide-band characteristics of the 60 ghz indoor radio channel," *IEEE Transactions on Wireless Communications*, vol. 3, no. 6, pp. 2396–2406, Nov. 2004.

[27] B. A. Bilgin, H. Ramezani, and O. B. Akan, "Human Blockage Model for Indoor Terahertz Band Communication," in *Proc. of IEEE International Conference on Communications Workshops (ICC Workshops)*, May 2019, pp. 1–6.

[28] J. Qiao, L. X. Cai, X. S. Shen, and J. W. Mark, "Enabling Multi-Hop Concurrent Transmissions in 60 GHz Wireless Personal Area Networks," *IEEE Transactions on Wireless Communications*, vol. 10, no. 11, pp. 3824–3833, Nov. 2011.

[29] C. Liaskos *et al.*, "Design and Development of Software Defined Metamaterials for Nanonetworks," *IEEE Circuits and Systems Magazine*, vol. 15, no. 4, pp. 12–25, Fourthquarter 2015.

[30] S. Abadal *et al.*, "Computing and Communications for the Software-Defined Metamaterial Paradigm: A Context Analysis," *IEEE Access*, 2017.

[31] Q. Wu and R. Zhang, "Intelligent Reflecting Surface Enhanced Wireless Network: Joint Active and Passive Beamforming Design," in *Proc. of IEEE Global Communications Conference (GLOBECOM)*, Dec. 2018, pp. 1–6.

[32] C. Huang *et al.*, "Reconfigurable intelligent surfaces for energy efficiency in wireless communication," *IEEE Transactions on Wireless Communications*, vol. 18, no. 8, pp. 4157–4170, 2019.

[33] L. Zhang *et al.*, "Space-time-coding digital metasurfaces," *Nature Communications*, vol. 9, no. 1, p. 4334, 2018.

[34] X. Tan, Z. Sun, J. M. Jornet, and D. Pados, "Increasing indoor spectrum sharing capacity using smart reflect-array," in *Proc. of IEEE International Conference on Communications (ICC)*, IEEE, 2016, pp. 1–6.

[35] H. Yang *et al.*, "A programmable metasurface with dynamic polarization, scattering and focusing control," *Scientific Reports*, vol. 6, p. 35 692, 2016.

[36] A. Li, S. Singh, and D. Sievenpiper, "Metasurfaces and their applications," *Nanophotonics*, vol. 7, no. 6, pp. 989–1011, 2018.

[37] Y.-H. Pao and V. Varatharajulu, "Huygens' principle, radiation conditions, and integral formulas for the scattering of elastic waves," *The Journal of the Acoustical Society of America*, vol. 59, no. 6, pp. 1361–1371, 1976.

[38] H.-T. Chen, A. J. Taylor, and N. Yu, "A review of metasurfaces: Physics and applications," *Reports on Progress in Physics*, vol. 79, no. 7, p. 076 401, 2016.

[39] C. Liaskos, S. Nie, A. Tsioliaridou, A. Pitsillides, S. Ioannidis, and I. F. Akyildiz, "A New Wireless Communication Paradigm through Software-Controlled Metasurfaces," *IEEE Communications Magazine*, vol. 56, no. 9, pp. 162–169, Sep. 2018.

[40] A. Tsioliaridou, C. Liaskos, A. Pitsillides, and S. Ioannidis, "A novel protocol for network-controlled metasurfaces," in *Proc. of the 4th ACM International Conference on Nanoscale Computing and Communication*, ACM, 2017, p. 3.

[41] A. Pitilakis *et al.*, "Software-Defined Metasurface Paradigm: Concept, Challenges, Prospects," in *Proc. of the 12th International Congress on Artificial Materials for Novel Wave Phenomena (Metamaterials)*, IEEE, 2018, pp. 483–485.

[42] A. C. Tasolamprou *et al.*, "Intercell wireless communication in software-defined metasurfaces," in *Proc. of IEEE International Symposium on Circuits and Systems (ISCAS)*, IEEE, 2018, pp. 1–5.

[43] J. Ma *et al.*, "Security and eavesdropping in terahertz wireless links," *Nature*, vol. 563, no. 7729, pp. 89–93, 2018.

[44] D. Chen *et al.*, "An LDPC code based physical layer message authentication scheme with prefect security," *IEEE Journal on Selected Areas in Communications*, vol. 36, no. 4, pp. 748–761, 2018.

[45] C. Liaskos, S. Nie, A. Tsioliaridou, A. Pitsillides, S. Ioannidis, and I. Akyildiz, "A novel communication paradigm for high capacity and security via programmable indoor wireless environments in next generation wireless systems," *Ad Hoc Networks*, vol. 87, pp. 1–16, 2019.

[46] C. Han and I. F. Akyildiz, "Distance-aware bandwidth-adaptive resource allocation for wireless systems in the terahertz band," *IEEE Transactions on Terahertz Science and Technology*, vol. 6, no. 4, pp. 541–553, 2016.

[47] J. M. Jornet and I. F. Akyildiz, "Graphene-based Plasmonic Nano-antenna for Terahertz Band Communication in Nanonetworks," *IEEE Journal on Selected Areas in Communications*, vol. 12, no. 12, pp. 685–694, Dec. 2013.

[48] I. F. Akyildiz and J. M. Jornet, *Ultra Massive MIMO Communication in the Terahertz Band*, US Patent App. 15/211,503, Nov. 2016.

[49] M. Tamagnone, J. Gomez-Diaz, J. Mosig, and J. Perruisseau-Carrier, "Analysis and design of terahertz antennas based on plasmonic resonant graphene sheets," *Journal of Applied Physics*, vol. 112, no. 11, p. 114 915, 2012.

[50] K. Yao and Y. Liu, "Plasmonic metamaterials," *Nanotechnology Reviews*, vol. 3, no. 2, pp. 177–210, 2014.

[51] G. Oliveri, D. H. Werner, and A. Massa, "Reconfigurable electromagnetics through metamaterials – a review," *Proceedings of the IEEE*, vol. 103, no. 7, pp. 1034–1056, 2015.

[52] C. Liaskos, A. Tsioliaridou, A. Pitsillides, S. Ioannidis, and I. F. Akyildiz, "Using Any Surface to Realize a New Paradigm for Wireless Communications," *Communications of the ACM*, vol. 61, no. 11, pp. 30–33, Oct. 2018.

[53] S. V. Hum and J. Perruisseau-Carrier, "Reconfigurable reflectarrays and array lenses for dynamic antenna beam control: A review," *IEEE Transactions on Antennas and Propagation*, vol. 62, no. 1, pp. 183–198, 2014.

[54] A. Y. Zhu, A. I. Kuznetsov, B. Lukyanchuk, N. Engheta, and P. Genevet, "Traditional and emerging materials for optical metasurfaces," *Nanophotonics*, vol. 6, no. 2, pp. 452–471, 2017.

[55] K. Iwaszczuk *et al.*, "Flexible metamaterial absorbers for stealth applications at terahertz frequencies," *Optics Express*, vol. 20, no. 1, p. 635, 2012.

[56] M. J. Lockyear, A. P. Hibbins, and J. R. Sambles, "Microwave surface-plasmon-like modes on thin metamaterials," *Physical review letters*, vol. 102, no. 7, p. 073 901, 2009.

[57] A. Singh, M. Andrello, N. Thawdar, and J. M. Jornet, "Design and operation of a graphene-based plasmonic nano-antenna array for communication in the terahertz band," *IEEE Journal on Selected Areas in Communications*, vol. 38, no. 9, pp. 2104–2117, 2020.

[58] H. Zhu, S. Cheung, K. L. Chung, and T. I. Yuk, "Linear-to-circular polarization conversion using metasurface," *IEEE Transactions on Antennas and Propagation*, vol. 61, no. 9, pp. 4615–4623, 2013.

[59] J. Hao, Y. Yuan, L. Ran, T. Jiang, J. A. Kong, C. Chan, and L. Zhou, "Manipulating electromagnetic wave polarizations by anisotropic metamaterials," *Physical review letters*, vol. 99, no. 6, p. 063 908, 2007.

[60] A. A. Saleh and R. Valenzuela, "A statistical model for indoor multipath propagation," *IEEE Journal on Selected Areas in Communications*, vol. 5, no. 2, pp. 128–137, 1987.

[61] C. Han, A. O. Bicen, and I. F. Akyildiz, "Multi-Ray Channel Modeling and Wideband Characterization for Wireless Communications in the Terahertz Band," *IEEE Transactions on Wireless Communications*, vol. 14, no. 5, pp. 2402–2412, May 2015.

[62] S. Nie, J. M. Jornet, and I. F. Akyildiz, "Intelligent Environments Based on Ultra-massive Mimo Platforms for Wireless Communication in Millimeter Wave and Terahertz Bands," in *Proc. of IEEE International Conference on Acoustics, Speech and Signal Processing (ICASSP)*, May 2019, pp. 7849–7853.

[63] O. El Ayach, S. Rajagopal, S. Abu-Surra, Z. Pi, and R. W. Heath, "Spatially sparse precoding in millimeter wave MIMO systems," *IEEE Transactions on Wireless Communications*, vol. 13, no. 3, pp. 1499–1513, 2014.

[64] S. V. Hum and J. Perruisseau-Carrier, "Reconfigurable reflectarrays and array lenses for dynamic antenna beam control: A review," *IEEE Transactions on Antennas and Propagation*, vol. 62, no. 1, pp. 183–198, 2013.

[65] C. Huang *et al.*, "Holographic MIMO surfaces for 6G wireless networks: Opportunities, challenges, and trends," *IEEE Wireless Communications*, vol. 27, no. 5, pp. 118–125, 2020.

[66] T. Otsuji *et al.*, "Emission and detection of terahertz radiation using two-dimensional electrons in III–V semiconductors and graphene," *IEEE Transactions on Terahertz Science and Technology*, vol. 3, no. 1, pp. 63–71, 2013.

[67] P. K. Singh, G. Aizin, N. Thawdar, M. Medley, and J. M. Jornet, "Graphene-based plasmonic phase modulator for terahertz-band communication," in *Proc. of the 10th European Conference on Antennas and Propagation (EuCAP)*, 2016, pp. 1–5.

[68] O. E. Ayach, R. W. Heath, S. Abu-Surra, S. Rajagopal, and Z. Pi, "The capacity optimality of beam steering in large millimeter wave MIMO systems," in *Proc. of the 13th IEEE International Workshop on Signal Processing Advances in Wireless Communications (SPAWC)*, 2012, pp. 100–104.

[69] C. A. Balanis, *Antenna Theory: Analysis and Design*. Wiley-Interscience, 2005, ISBN: 0471714623.

[70] N. Yu *et al.*, "Light propagation with phase discontinuities: Generalized laws of reflection and refraction," *Science*, vol. 334, no. 6054, pp. 333–337, 2011.

[71] F. Aieta *et al.*, "Out-of-plane reflection and refraction of light by anisotropic optical antenna metasurfaces with phase discontinuities," *Nano Letters*, vol. 12, no. 3, pp. 1702–1706, 2012.

[72] B. Di *et al.*, "Hybrid beamforming for reconfigurable intelligent surface based multi-user communications: Achievable rates with limited discrete phase shifts," *IEEE Journal on Selected Areas in Communications*, vol. 38, no. 8, pp. 1809–1822, 2020.

[73] Q. Wu and R. Zhang, "Intelligent reflecting surface enhanced wireless network via joint active and passive beamforming," *IEEE Transactions on Wireless Communications*, vol. 18, no. 11, pp. 5394–5409, 2019.

[74] M. Di Renzo *et al.*, "Smart Radio Environments Empowered by Reconfigurable Intelligent Surfaces: How It Works, State of Research, and The Road Ahead," *IEEE Journal on Selected Areas in Communications*, vol. 38, no. 11, pp. 2450–2525, 2020.

[75] A. Arbabi, Y. Horie, M. Bagheri, and A. Faraon, "Dielectric metasurfaces for complete control of phase and polarization with subwavelength spatial resolution and high transmission," *Nature Nanotechnology*, vol. 10, no. 11, pp. 937–943, 2015.

[76] Y. Zhang, Y. Feng, B. Zhu, J. Zhao, and T. Jiang, "Graphene based tunable metamaterial absorber and polarization modulation in terahertz frequency," *Optics Express*, vol. 22, no. 19, pp. 22 743–22 752, 2014.

[77] F. W. Vook, E. Visotsky, T. A. Thomas, and B. Mondal, "Product codebook feedback for massive MIMO with cross-polarized 2D antenna arrays," in *Proc. of the 25th Annual International Symposium on Personal, Indoor, and Mobile Radio Communication (PIMRC)*, 2014, pp. 502–506.

[78] E. Zöchmann *et al.*, "Directional evaluation of receive power, Rician K-factor and RMS delay spread obtained from power measurements of 60 GHz indoor channels," in *Proc. of IEEE-APS Topical Conference on Antennas and Propagation in Wireless Communications (APWC)*, 2016, pp. 246–249.

[79] L. Yan, C. Han, and J. Yuan, "A Dynamic Array-of-Subarrays Architecture and Hybrid Precoding Algorithms for Terahertz Wireless Communications," *IEEE Journal on Selected Areas in Communications*, vol. 38, no. 9, pp. 2041–2056, 2020.

[80] A. Karttunen, C. Gustafson, A. F. Molisch, J. Järveläinen, and K. Haneda, "Censored multipath component cross-polarization ratio modeling," *IEEE Wireless Communications Letters*, vol. 6, no. 1, pp. 82–85, 2016.

[81] I. F. Akyildiz, S. Nie, S.-C. Lin, and M. Chandrasekaran, "5G roadmap: 10 key enabling technologies," *Computer Networks*, vol. 106, pp. 17–48, 2016.

[82] S. Nie, C. Han, and I. F. Akyildiz, "A three-dimensional time-varying model for 5G indoor dual-mobility channels," in *Proc. of the 86th IEEE Vehicular Technology Conference (VTC Fall)*, Sep. 2017.

[83] C. Han and I. F. Akyildiz, "Three-Dimensional End-to-End Modeling and Analysis for Graphene-Enabled Terahertz Band Communications," *IEEE Transactions on Vehicular Technology*, vol. 66, no. 7, pp. 5626–5634, 2016.

[84] R. Piesiewicz *et al.*, "Scattering Analysis for the Modeling of THz Communication Systems," *IEEE Transactions on Antennas and Propagation*, vol. 55, no. 11, pp. 3002–3009, Nov. 2007.

[85] J. Kokkoniemi *et al.*, "Frequency and time domain channel models for nanonetworks in terahertz band," *IEEE Transactions on Antennas and Propagation*, vol. 63, no. 2, pp. 678–691, 2015.

[86] S. Priebe *et al.*, "Channel and propagation measurements at 300 GHz," *IEEE Transactions on Antennas and Propagation*, vol. 59, no. 5, pp. 1688–1698, 2011.

[87] S. M. Kay, *Fundamentals of Statistical Signal Processing, Volume I: Estimation Theory*. Prentice Hall, 1993.

[88] J. Salmi, A. Richter, and V. Koivunen, "Detection and tracking of MIMO propagation path parameters using state-space approach," *IEEE Transactions on Signal Processing*, vol. 57, no. 4, pp. 1538–1550, 2009.

[89] 3GPP TR 38.901, "Study on channel model for frequencies from 0.5 to 100 GHz," Mar. 2017.

[90] I. F. Akyildiz and A. Kak, "The Internet of Space Things/Cubesats," *IEEE Network*, vol. 33, no. 5, pp. 212–218, 2019.

[91] S. Weston *et al.*, "State of the Art: Small Spacecraft Technology," *NASA Technical Report*, Oct. 2020.

[92] M. Sweeting, "Modern Small Satellites-Changing the Economics of Space," *Proceedings of the IEEE*, vol. 106, no. 3, pp. 343–361, 2018.

[93] I. F. Akyildiz, J. M. Jornet, and S. Nie, "A new CubeSat design with reconfigurable multi-band radios for dynamic spectrum satellite communication networks," *Ad Hoc Networks*, vol. 86, pp. 166–178, 2019.

[94] S. Bandyopadhyay *et al.*, "A review of impending small satellite formation flying missions," in *Proc. of the 53rd AIAA Aerospace Sciences Meeting*, 2015, p. 1623.

[95] R. Radhakrishnan *et al.*, "Survey of inter-satellite communication for small satellite systems: Physical layer to network layer view," *IEEE Communications Surveys and Tutorials*, vol. 18, no. 4, pp. 2442–2473, 2016.

[96] O. Kodheli *et al.*, "Satellite Communications in the New Space Era: A Survey and Future Challenges," *IEEE Communications Surveys and Tutorials*, pp. 1–1, 2020.

[97] P. Grenfell, A. Aguilar, K. Cahoy, and M. Long, "Pointing, Acquisition, and Tracking for Small Satellite Laser Communications," in *Proc. of the 32nd Annual AIAA/USU Conference on Small Satellites*, 2018.

[98] S. Krucker *et al.*, "Solar flares at submillimeter wavelengths," *The Astronomy and Astrophysics Review*, vol. 21, no. 1, p. 58, 2013.

[99] J. Kokkoniemi *et al.*, "Impact of beam misalignment on THz wireless systems," *Nano Communication Networks*, vol. 24, p. 100 302, 2020.

[100] Z. Sodnik, B. Furch, and H. Lutz, "Free-space laser communication activities in Europe: SILEX and beyond," in *Proc. of the 19th Annual Meeting of the IEEE Lasers and Electro-Optics Society*, 2006, pp. 78–79.

[101] L. Wang, C. Jiang, L. Kuang, S. Wu, and S. Guo, "TDRSS scheduling algorithm for non-uniform time-space distributed missions," in *Proc. of the IEEE Global Communications Conference*, 2017, pp. 1–6.

[102] Y. Xie and Y. Fang, "A general statistical channel model for mobile satellite systems," *IEEE Transactions on Vehicular Technology*, vol. 49, no. 3, pp. 744–752, 2000.

[103] W. Li, C. L. Law, V. K. Dubey, and J. Ong, "Ka-band land mobile satellite channel model incorporating weather effects," *IEEE Communications Letters*, vol. 5, no. 5, pp. 194–196, 2001.

[104] K. P. Liolis, A. D. Panagopoulos, and S. Scalise, "On the combination of tropospheric and local environment propagation effects for mobile satellite systems above 10 GHz," *IEEE Transactions on Vehicular Technology*, vol. 59, no. 3, pp. 1109–1120, 2009.

[105] P. Petropoulou, E. T. Michailidis, A. D. Panagopoulos, and A. G. Kanatas, "Radio propagation channel measurements for multi-antenna satellite communication systems: A survey," *IEEE Antennas and Propagation Magazine*, vol. 56, no. 6, pp. 102–122, 2014.

[106] J. Y. Suen, M. T. Fang, S. P. Denny, and P. M. Lubin, "Modeling of terabit geostationary terahertz satellite links from globally dry locations," *IEEE Transactions on Terahertz Science and Technology*, vol. 5, no. 2, pp. 299–313, 2015.

[107] J. Y. Suen, "Terabit-per-second satellite links: a path toward ubiquitous terahertz communication," *Journal of Infrared, Millimeter, and Terahertz Waves*, vol. 37, no. 7, pp. 615–639, 2016.

[108] J. Taylor, K.-M. Cheung, D. Seo, *et al.*, "Galileo Telecommunications," *DESCANSO Design and Performance Summary Series*, 2002.

[109] J. Chang *et al.*, "Body pointing, acquisition and tracking for small satellite laser communication," in *Proc. of the SPIE Free-Space Laser Communications XXXI*, vol. 10910, 2019, pp. 144–152.

[110] A. Richardson, "2019 NRL Plasma Formulary," *The Office of Naval Research*, 2019.

[111] D. Fixsen, "The temperature of the cosmic microwave background," *The Astrophysical Journal*, vol. 707, no. 2, p. 916, 2009.

[112] D. Muhleman, P. Esposito, and J. Anderson, "The electron density profile of the outer corona and the interplanetary medium from Mariner-6 and Mariner-7 time-delay measurements," *The Astrophysical Journal*, vol. 211, pp. 943–957, 1977.

[113] A. Berman, "A unified observational theory for solar wind columnar turbulence," *The Deep Space Network Progress Report 42*, vol. 50, pp. 124–131, 1979.

[114] W. Clohessy and R. Wiltshire, "Terminal guidance system for satellite rendezvous," *Journal of the Aerospace Sciences*, vol. 27, no. 9, pp. 653–658, 1960.

[115] Y. Kozai, "New determination of zonal harmonics coefficients of the earth's gravitational potential," *SAO Special Report*, vol. 165, 1964.

[116] T. Svantesson, "A physical MIMO radio channel model for multi-element multi-polarized antenna systems," in *Proc. of the 54th IEEE Vehicular Technology Conference*, vol. 2, 2001, pp. 1083–1087.

[117] A. D. Panagopoulos, P.-D. M. Arapoglou, and P. G. Cottis, "Satellite communications at Ku, Ka, and V bands: Propagation impairments and mitigation techniques," *IEEE Communications Surveys and Tutorials*, vol. 6, no. 3, pp. 2–14, 2004.

[118] R. P. Welle, "The Cubesat Paradigm: An Evolutionary Approach To Satellite Design," The Aerospace Corporation, Tech. Rep., 2016.

[119] J. Puig-Suari, C. Turner, and W. Ahlgren, "Development of the standard CubeSat deployer and a CubeSat class PicoSatellite," in *Proc. of the IEEE Aerospace Conference*, vol. 1, Mar. 2001, 1/347–1/353 vol.1.

[120] K. Woellert, P. Ehrenfreund, A. J. Ricco, and H. Hertzfeld, "Cubesats: Cost-effective science and technology platforms for emerging and developing nations," *Advances in Space Research*, vol. 47, no. 4, pp. 663–684, 2011.

[121] S. Madry, *Space Systems for Disaster Warning, Response, and Recovery*. Springer, 2014, ISBN: 9781493915125.

[122] R. Hevner, W. Holemans, J. Puig-Suari, and R. Twiggs, "An advanced standard for CubeSats," *Proc. of the Small Satellite Conference*, Aug. 2011.

[123] N. Crisp, K. Smith, and P. Hollingsworth, "Launch and deployment of distributed small satellite systems," *Acta Astronautica*, vol. 114, pp. 65–78, 2015.

[124] L. J. Ippolito and L. J. Ippolito Jr, *Satellite communications systems engineering: Atmospheric effects, satellite link design and system performance*. John Wiley & Sons, 2017.

[125] J. Straub, M. Wegerson, and R. Marsh, "An intelligent attitude determination and control system for a CubeSat class spacecraft," in *Proc. of the AIAA SPACE Conference and Exposition*, 2015, p. 4422.

[126] Z. Pi and F. Khan, "An introduction to millimeter-wave mobile broadband systems," *IEEE Communications Magazine*, vol. 49, no. 6, pp. 101–107, Jun. 2011.

[127] V. W. Chan, "Optical satellite networks," *Journal of Lightwave Technology*, vol. 21, no. 11, p. 2811, 2003.

[128] Z. Sodnik, B. Furch, and H. Lutz, "Optical intersatellite communication," *IEEE Journal of Selected Topics in Quantum Electronics*, vol. 16, no. 5, pp. 1051–1057, 2010.

[129] A. H. M. Shirazi *et al.*, "On the design of mm-wave self-mixing-VCO architecture for high tuning-range and low phase noise," *IEEE Journal of Solid-State Circuits*, vol. 51, no. 5, pp. 1210–1222, 2016.

[130] I. Mehdi, J. V. Siles, C. Lee, and E. Schlecht, "THz diode technology: status, prospects, and applications," *Proceedings of the IEEE*, vol. 105, no. 6, pp. 990–1007, 2017.

[131] T. W. Crowe, W. R. Deal, M. Schröter, C.-K. C. Tzuang, and K. Wu, "Terahertz RF Electronics and System Integration," *Proceedings of the IEEE*, vol. 105, no. 6, pp. 985–989, 2017.

[132] A. Rashidinejad, Y. Li, and A. M. Weiner, "Recent Advances in Programmable Photonic-Assisted Ultrabroadband Radio-Frequency Arbitrary Waveform Generation," *IEEE Journal of Quantum Electronics*, vol. 52, no. 1, pp. 1–17, Jan. 2016.

[133] J. Wang *et al.*, "Reconfigurable radio-frequency arbitrary waveforms synthesized in a silicon photonic chip," *Nature Communications*, vol. 6, p. 5957, 2015.

[134] P. Ghelfi, G. Serafino, F. Scotti, F. Laghezza, and A. Bogoni, "Flexible receiver for multiband orthogonal frequency division multiplexing signals at the millimeter waveband based on optical downconversion," *Optics Letters*, vol. 37, no. 18, pp. 3924–3926, 2012.

[135] F. Laghezza, F. Scotti, P. Ghelfi, and A. Bogoni, "Photonics-assisted multiband RF transceiver for wireless communications," *Journal of Lightwave Technology*, vol. 32, no. 16, pp. 2896–2904, 2014.

[136] X. Yang *et al.*, "Optical frequency comb based multi-band microwave frequency conversion for satellite applications," *Optics Express*, vol. 22, no. 1, pp. 869–877, 2014.

[137] C. G. Christodoulou, Y. Tawk, S. A. Lane, and S. R. Erwin, "Reconfigurable antennas for wireless and space applications," *Proceedings of the IEEE*, vol. 100, no. 7, pp. 2250–2261, 2012.

[138] X. Liu, S. Yao, B. S. Cook, M. M. Tentzeris, and S. V. Georgakopoulos, "An origami reconfigurable axial-mode bifilar helical antenna," *IEEE Transactions on Antennas and Propagation*, vol. 63, no. 12, pp. 5897–5903, 2015.

[139] L. Zakrajsek, E. Einarsson, N. Thawdar, M. Medley, and J. M. Jornet, "Design of Graphene-based Plasmonic Nano-antenna Arrays in the Presence of Mutual Coupling," in *Proc. of the 11th European Conference on Antennas and Propagation (EuCAP)*, 2017.

[140] C. Ao *et al.*, "A first demonstration of Mars crosslink occultation measurements," *Radio Science*, vol. 50, no. 10, pp. 997–1007, 2015.

[141] T. Grelier *et al.*, "Formation flying radio frequency instrument: First flight results from the PRISMA mission," in *Proc. of the 5th ESA Workshop on Satellite Navigation Technologies and European Workshop on GNSS Signals and Signal Processing (NAVITEC)*, 2010, pp. 1–8.

[142] J. Y. Suen, M. T. Fang, and P. M. Lubin, "Global Distribution of Water Vapor and Cloud Cover – Sites for High-Performance THz Applications," *IEEE Transactions on Terahertz Science and Technology*, vol. 4, no. 1, pp. 86–100, Jan. 2014.

[143] T. Tjelta *et al.*, "Results of a Ka band campaign for the characterisation of propagation conditions for SatCom systems at high latitudes," in *Proc. of the 11th European Conference on Antennas and Propagation (EUCAP)*, Mar. 2017, pp. 1481–1485.

[144] ITU-T, "Specific attenuation model for rain for use in prediction methods," International Telecommunication Union, Recommendation P.838-3, Mar. 2005.

[145] P.-D. Arapoglou *et al.*, "MIMO over satellite: A review," *IEEE communications surveys & tutorials*, vol. 13, no. 1, pp. 27–51, 2011.

[146] R. C. de Lamare, "Massive MIMO systems: signal processing challenges and future trends," *URSI Radio Science Bulletin*, vol. 86, no. 4, pp. 8–20, 2013.

[147] R. J. Barton, "Distributed MIMO communication using small satellite constellations," in *Proc. of IEEE International Conference on Wireless for Space and Extreme Environments (WiSEE)*, Oct. 2014, pp. 1–7.

[148] S. Dörner *et al.*, "Deep learning based communication over the air," *IEEE Journal of Selected Topics in Signal Processing*, vol. 12, no. 1, pp. 132–143, 2018.

[149] I. Goodfellow, Y. Bengio, A. Courville, and Y. Bengio, *Deep Learning*. MIT Press, 2016, vol. 1.

VITA

Shuai Nie received the Bachelor of Engineering degree in Telecommunications Engineering from Xidian University, Xi'an, China, in 2012, and received the Master of Science degree in Electrical Engineering from New York University, Brooklyn, in 2014. She received the Ph.D. degree in Electrical and Computer Engineering from Georgia Institute of Technology, Atlanta, in May 2021, under the supervision of Prof. Ian F. Akyildiz. She is a graduate student member of the IEEE. Her current research interests include terahertz band communication systems, millimeter wave communications, and satellite communications, with a focus on channel modeling, physical layer design, and signal processing.